

# **Aalborg Universitet**

# A Micro Raman Investigation of Viscoelasticity in Short Fibre Reinforced Polymer **Matrix Composites**

Schjødt-Thomsen, Jan

Publication date: 2000

Document Version Publisher's PDF, also known as Version of record

Link to publication from Aalborg University

Citation for published version (APA):

Schjødt-Thomsen, J. (2000). À Micro Raman Investigation of Viscoelasticity in Short Fibre Reinforced Polymer Matrix Composites. Department of Mechanical Engineering, Aalborg University.

Copyright and moral rights for the publications made accessible in the public portal are retained by the authors and/or other copyright owners and it is a condition of accessing publications that users recognise and abide by the legal requirements associated with these rights.

- Users may download and print one copy of any publication from the public portal for the purpose of private study or research.
- You may not further distribute the material or use it for any profit-making activity or commercial gain
   You may freely distribute the URL identifying the publication in the public portal -

Take down policy
If you believe that this document breaches copyright please contact us at vbn@aub.aau.dk providing details, and we will remove access to the work immediately and investigate your claim.

Institute of Mechanical Engineering Aalborg University Special Report No. 42

# A Micro Raman Investigation of Viscoelasticity in Short Fibre Reinforced Polymer Matrix Composites

Ph.D. Dissertation

by

Jan Schjødt-Thomsen

### Copyright © 2000 Jan Schjødt-Thomsen

Reproduction of material contained in this report is permitted provided that the source is given. Additional copies are available at the cost of printing and mailing from Line Nesgaard Jensen, Institute of Mechanical Engineering, Aalborg University, Pontoppidanstraede 101, DK-9220 Aalborg East, Denmark. Telephone: +45 96 35 93 00, Fax: +45 98 15 14 11. Questions and comments are most welcome and can be directed to the author at the same address or by electronic mail: jst@ime.auc.dk.

Printed at Aalborg University, January 2000.

ISSN 0905-2305

# **Preface**

This dissertation has been submitted to the Faculty of Science and Technology of Aalborg University, Aalborg, Denmark, in partial fulfilment of the requirements for the technical Ph.D. degree.

The project underlying this thesis has been carried out from September 1996 to September 1999 at the Institute of Mechanical Engineering at Aalborg University. The project has been supervised by Professor, dr.techn. Ryszard Pyrz, to whom I am deeply grateful for his inspiring ideas, his encouraging spirit and his guidance through the project.

I would like to thank my friends and colleagues, M.Sc. Anders Steen Nielsen, M.Sc. Jens Nygaard and Ph.D. Nikolaj Vejen for many exhausting and inspiring discussions and also the other colleagues at the Institute of Mechanical Engineering.

I am greatly indebted to Kristian Glejbøl, Berit Pedersen and Bjørn Winther Jensen at NKT Research Center, Brøndby, Denmark, for plasma treating the carbon fibres and grafting the polypropylene used in this work.

Finally, I wish to thank Ph.D. Charles Lawrence for reading the manuscript and suggesting minor corrections.

Jan Schjødt-Thomsen

Aalborg, January 2000

# **Abstract**

The purpose of the present Ph.D. project is to investigate the load transfer mechanisms between the fibre and matrix and the stress/strain fields in and around single fibres in short fibre reinforced viscoelastic polymer matrix composites subjected to various loading histories. The materials considered are high modulus carbon fibres embedded in a polypropylene matrix. The polypropylene matrix displays nonlinear viscoelasticity and its constitutive behaviour is modelled using the Schapery model.

The investigation of the load transfer mechanisms and the local stress/strain field is based on experimental work conducted on model composites consisting of one or a few fibres embedded in the polymer matrix. The fibre strains are measured *in situ* during loading, using micro Raman spectroscopy.

Different loading histories are applied to the test specimens; Creep loading, mechanical conditioning and subsequent creep, creep loading and subsequent recovery, creep loading at an elevated temperature, creep loading of specimens with misaligned fibres and creep loading of specimens with interacting fibres.

Experiments have shown two different load transfer mechanisms. The first which is of a friction-like nature where the load of the fibre is governed by the coefficient of friction and the initial radial pressure on the fibre, stemming from manufacture. The second load transfer mechanism is due to improved adhesion between the fibre and matrix obtained by grafting the polypropylene with maleic-anhydride.

The experimental results for the two load transfer cases are subsequently used to determine the interfacial shear strength. When the load transfer is friction-like the interfacial shear strength is rather low, whereas the interfacial shear strength is governed by the matrix shear yield strength when the load transfer is due to adhesion between the fibre and matrix.

In order to investigate the nonlinear stress/strain field due to the two load transfer mechanisms, two qualitative approaches for analysing the single fibre composite - subjected to creep loading conditions - have been proposed and is used along with nonlinear finite element models. The two models are based on the integration of point forces along the fibre boundary and the major difference of the two approaches is that the first uses experimental inputs, whereas the second is purely theoretical. The two models are plane models and are capable of taking misalignment of the fibres, with respect to the loading axis, into account. In the two models as well as in the finite element models thermal stress/strain from manufacture is taken into account. It is shown that the initial residual stress in the specimen from manufacture may have a beneficial influence on the loading transferred to the fibres, i.e. the residual stresses may prohibit tensile fibre fractures. Selected experimental results are compared to calculated results.

Overall creep behaviour of short fibre reinforced composites is predicted using the Mori - Tanaka mean field approach where the fibres are modelled as volumes containing equavalent eigenstrains. These eigenstrains are related to strain through the Eshelby tensor. In the present work the Mori - Tanaka mean field approach has been extended to incorporate both the effect of a weakened interface through a modified Eshelby tensor and the effect of different fibre orientations through a statistical fibre orientation function. The degree of weakening of the interface is governed by an interfacial parameter based upon the interfacial shear strength obtained from experiments. Different fibre orientations are considered in terms of stiffness and creep properties.

# **Abstrakt**

Formålet med det foreliggende Ph.D. projekt er at undersøge belastningsoverførslen mellem fibre og matrix, samt spændings/tøjnings-feltet i og omkring enkelte fibre i kort fiber forstærkede viskoelastiske polymer matrix kompositter i forskellige belastningssituationer. De benyttede materialer er høj modul kulfibre i en polypropylen matrix.

Polypropylen udviser ulineær viskoelasticitet og den konstitutive opførsel beskrives ved hjælp af Schapery's model.

Undersøgelsen af belastningsoverførslen mellem fibre og matrix samt det lokale spændings- og tøjnings-felt er baseret på eksperimentelle undersøgelser af modelkompositter med mikro Raman spektroskopi, hvor fiber tøjningen måles direkte under belastning af prøveemnet.

Prøveemnerne påvirkes med forskellige belastningsforløb; Krybning, mekanisk konditionering og efterfølgende krybning, krybning og efterfølgende aflastning (recovery), krybning ved forhøjet temperatur, krybning af emner med fibre der ikke er parallelle med belastningsretningen, samt krybning af emner med fibre der påvirker hinanden.

Eksperimenterne har vist to forskellige belastningsoverførselsmekanismer. Den ene er friktionslignende, hvor belastningen der overføres til fiberen er bestemt af friktionskoefficienten mellem fiber og matrix samt af det termisk inducerede initielle radielle tryk på fiberen. Den anden belastningsoverførselsmekanisme skyldes behandlingen af polypropylen med malein-syre-anhydrid, hvilket forøger bindingen mellem fiber og matrix.

De eksperimentelle resultater for de to situationer er efterfølgende benyttet til at bestemme interface forskydningsstyrken. I friktionssituationen er interface forskydningsstyrken ret lav mens den i den anden situation er bestemt af matrix materialets forskydningsflydespænding.

For at undersøge spændings- og tøjnings-feltet som følge af de to belastningsoverførselsmekanismer er to forskellige metoder foreslået. Disse er baseret på integration af punktkræfter langs fiberranden. Den afgørende forskel på de to metoder er at den ene benytter eksperimentelle data som input, mens den anden er ren teoretisk. De to metoder er 2-dimensionelle og er således istand til at medtage indflydelsen af fibre, der ikke er parallelle med belastningsretningen. Sammen med de to modeller er der benyttet ulineære finite element modeller. I både de to modeller samt i FEM beregningerne er der taget højde for termiske spændinger og tøjninger. Det er vist at de termisk inducerede spændinger kan forhindre trækbrud i fiberen. Beregnede resultater er efterfølgende sammenlignet med udvalgte eksperimentelle resultater.

Den makroskopiske krybning af kort fiber forstærkede kompositter er modelleret med Mori-Tanaka's middelfelt teori, hvori fibrene betragtes som områder med ækvivalente eigentøjninger. Disse eigentøjninger er relateret til tøjninger via Eshelby tensoren. I det foreliggende arbejde er Mori-Tanaka's teori udvidet til at medtage effekten af et forringet fiber/matrix interface via en modificeret Eshelby tensor samt effekten af forskellige fiber orienteringer via en statistisk fiber orienteringsfunktion. Forringelsen af interfacet er styret af en interfaceparameter der er beregnet udfra den eksperimentelt bestemte interfaceforskydningsstyrke. Endvidere er forskellige fiberorienteringers indflydelse på komposittens krybeegenskaber og stivhed undersøgt.

# **Contents**

Preface								
A	Abstract (English)							
A	Abstrakt (Danish)							
1	Introduction							
	1.1	Creep Modelling Approaches	12					
	1.2	Outline	13					
2	Rar	man Spectroscopy	15					
	2.1	Theoretical Raman Scattering	16					
	2.2	Experimental Setup	21					
	2.3	Applications of MRS	24					
	2.4	Summary	28					
3 Viscoelasticity								
	3.1	Viscoelastic Constitutive Models	30					
	3.2	The Schapery Model	32					
		3.2.1 Creep	35					
		3.2.2 Recovery	37					
		3.2.3 Relaxation	37					
	3.3	3 - D Constitutive Model	39					
	3.4	Summary	40					
4	Exp	perimental Results	41					
	4.1	Specimen Preparation and Materials Data	41					

CONTENTS

$\mathbf{R}$	References 12							
7	Con	clusio	ns	117				
	6.6	Summ	ary	116				
	6.5		Ss					
	6.4	Fibre	Orientation	107				
	6.3	Imper	fect Interface	105				
	6.2	Incren	nental Creep Modelling	101				
	6.1	Overa	ll modelling	99				
6	Ove	rall C	reep Modelling	99				
	5.5	Summ	ary	95				
	5.4		s from Approaches I, II and FEM					
	5.3		Element Analysis					
	5.2	-	Modelling, Approach II					
	5.1	Creep	Modelling, Approach I	73				
5	Sing		re Creep Modelling	71				
	4.0	Summ	ary	00				
	4.5	4.4.1	Results					
	4.4		Acial Strength					
	4.4	4.3.5	Fibre Surface Morphology					
		4.3.4	Creep Strain in Misaligned Fibres and Fibre Interaction					
		4.3.3	24/48 hour Creep and Creep at an Elevated Temperature					
		4.3.2	Mechanical Conditioning/Creep and Creep/Recovery	53				
		4.3.1	Creep	51				
	4.3	Exper	imental Results for PP-MA Specimens	49				
		4.2.3	24 hour Creep	48				
		4.2.2	Creep and Subsequent Recovery	46				
		4.2.1	Mechanical Conditioning and Subsequent Creep	45				
	4.2	Exper	imental Results for PP-U Specimens	43				

**121** 

C	CONTENTS			
${f A}$	APPENDICES	129		
$\mathbf{A}$	Stresses Due to a Point Force	131		
В	Average Strain and Stress Theorems	135		
	B.1 Average strain theorem	135		
	B.2 Average stress theorem	136		

8 CONTENTS

1

# Introduction

Development of fibre reinforced composites with thermoplastic polymer matrices has acquired considerable attention in the recent years. Owing to the continuous need for structural weight reduction and recycleability it is believed this trend will persist well into the future. Several advantages of thermoplastic over the thermosetting polymers have been recognised. These include short moulding cycles, excellent chemical and corrosion resistance and recycleability. The recent developments in thermoplastic matrices for high performance composites involve primarily the use of poly-ether-ether-ketone (PEEK), poly-ether-sulfone (PES) and poly-phenylene-sulphide (PPS). Unfortunately, these polymers are usually very expensive and require relatively advanced processing tools. As a consequence, efforts have been made to replace these expensive thermoplastic polymers with the commodity polymers such as polyamide (PA) and polypropylene (PP). In engineering applications these materials are usually reinforced with short fibres rather than continuous fibres and for "common" purposes these material combinations have proved to be very cost effective.

However, an important aspect of composite structural performance is the properties' time dependent nature. This behaviour affects the fit and finish of components and the dimensional and structural stability of load bearing components. Before prediction of the structural behaviour of larger composite structures can be achieved their viscoelastic behaviour must be understood.

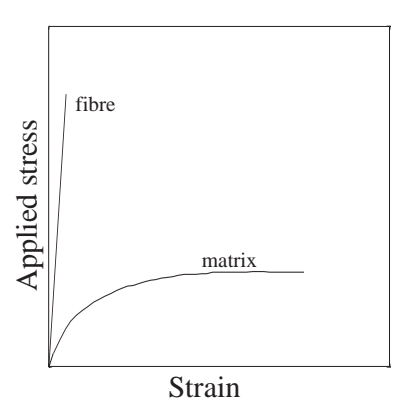


Figure 1.1: Schematic response to simple tension of a fibre and a polymer matrix.

The complexities of composite viscoelasticity arise due to the fact that two materials, with very

different constitutive behaviour, are combined. Subjected to simple tension the polymeric matrix and the fibre will behave as shown schematically in figure 1.1. It is seen that the fibre behaves linear elasticly until fracture occurs, whereas the matrix behaves elastic-plastic. Application of creep loading conditions to the fibre and the matrix yields two different responses also, as shown schematically in figures 1.2A and B. The fibre strain is constant with respect to time, whereas the graph of the matrix strain displays three distinct regions. In the first region, known as the primary creep region or the transient creep region, the creep strain is continuously increasing with a decreasing rate. In region II the material displays steady state creep or secondary creep, where the creep strain is increasing at a nearly constant rate. In region III, the tertiary creep region, the creep strain increases at a continuously increasing rate until failure. This region is rarely considered in creep modelling or in a components service life because the time from the onset of tertiary creep until the component breaks may be very short.

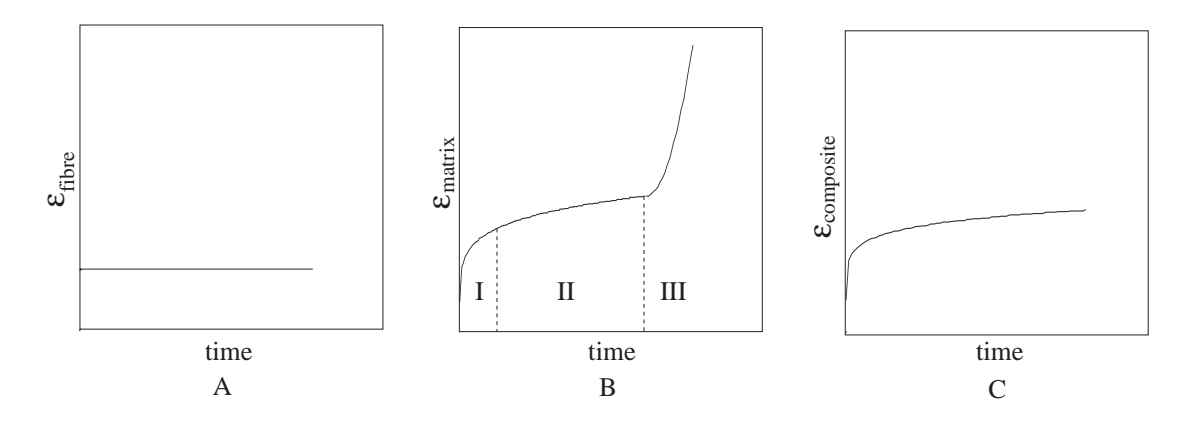


Figure 1.2: Schematic response to creep loading of A) a fibre, B) a matrix and C) a composite.

In figure 1.2C the creep strain of a composite is shown schematically. In figures 1.2A, B and C, the magnitude of strains are  $\varepsilon_m > \varepsilon_{comp.} > \varepsilon_f$ . This suggests that a thorough understanding of composite viscoelasticity is essential since the matrix material and the reinforcing fibres interact and in fact combine to form a third and completely different material.

An understanding of the importance of composite viscoelasticity is essential in, for example the off-shore industry for construction of cables to mount on oil rigs to keep them in the desired position or for construction of pipes for transport of natural gas and oil. These cables or pipes may be so large that they can not carry their own weight if they are made of traditional engineering materials. Then the only alternative is to substitute the original material with composites due to their high strength to weight ratio. The prediction of the structural behaviour of such components is an extremely difficult task. The nature of the load is dynamic, the environment is highly aggressive both on the outside of the component and on the inside of the pipes where a high temperature mixture of gas and oil flows, and if the composite mechanics is not fully understood the prediction of the structural behaviour may be very wrong. Furthermore, in these situations it is essential to have a thorough knowledge of the micromechanics of composites because diffusion of gas and oil into the region between the fibre and matrix will lead to a degeneration of the composite material and finally to a break down of its structure.

The viscoelastic behaviour of fibre reinforced composites is dependent upon loading situation, fibre distribution, environment and last, but definitely not least, of the load transfer efficiency in the region between the matrix and the reinforcing fibre. Since this region is very important for allmost all overall composite properties a definition of the terms used seems appropriate:

**Interphase:** This is defined as a three dimensional region between the fibre and matrix with physical and chemical properties differing from those of the fibre and matrix respectively.

**Interface:** This is defined as a two dimensional border between the fibre and interphase or between the fibre and matrix if an interphase is not present.

According to these definitions an interphase becomes an interface if its thickness decreases to zero.

In this thesis the region between the fibre and matrix is considered as an interface. Thus, no "different" material between the fibre and matrix will be considered in the theoretical modelling.

The importance of loading, fibre distribution, environment and load transfer efficiency on composite viscoelasticity have been appreciated for a long time, but the lack of an effective method to quantify the latter has lead to proposals of various experimental methods, the fragmentation test being one of the most common. Unfortunately, the results from fragmentation tests are not fully understood. However, it seems, at present, that micro Raman spectroscopy, (MRS), is one of the most powerful techniques for analysing the micromechanics of composite materials, and especially the load transfer efficiency/mechanism due to the techniques' high spatial resolution.

Thus, the purpose of the present work is to investigate the load transfer mechanisms between the fibre and matrix and the stress/strain fields in and around single fibres in short fibre model composites subjected to various loading histories. The experimental basis is micro Raman spectroscopy which is used for *in-situ* measurements of the fibre strains.

Two material combinations have been used in this study. One consisting of polypropylene, with plasma treated carbon fibres subsequently denoted as "PP-U" and polypropylene modified with maleic anhydride with standard surface treated fibres, subsequently denoted as "PP-MA". The fibres used are high modulus PAN based carbon fibres with an "as received" surface treatment and with a plasma surface treatment conducted by NKT Research Center, Denmark.

Experimental creep and relaxation data for the matrix material have been provided by BASF. The reason for this choice of materials is that the primary purpose of the project is to investigate phenomena occurring in a viscoelastic composite subjected to creep loading. Polypropylene is widely used as a model material because it is easy crystallisable, easy to process and a wide spectrum of crystallinities and crystal dimensions can be obtained [47]. Additionally, polypropylene displays creep behaviour within a relatively short amount of time and this is desirable in the present study. Finally, polypropylene has proven to be very suitable for MRS in conjunction with carbon fibres due to its low flourescence in the frequency range considered in this work.

Carbon fibres are rarely used in conjunction with injection moulded polypropylene composites. However, carbon fibres have been chosen because they are very suitable for MRS as internal strain-gauges. Furthermore, the phenomena occurring around the fibre is believed to be invariant with respect to the type of fibre used, whereas the magnitude of the measured quantities may differ.

The high modulus, (HM), PAN based carbon fibres have been chosen because they are commonly used in a variety of applications, whereas pitch based fibres are very rarely used because they are very brittle. Another advantage of the HM carbon fibre is that they possess a second order Raman peak which twice as strain sensitive as the first order peaks.

# 1.1 Creep Modelling Approaches

The modelling of creep in composite materials demands different approaches depending on the application of the model and the complexity of the service history applied to the composite. Creep models may be developed on different levels. A "model" may be empirical if the overall response of the material, as observed from experiments, is the only interest. Secondly, a model may be purely phenomenological if an overall response of the material is of primary interest, whereas a continuum model may be able to describe some of the microstructural influences in an average sense and neglecting details which are of less importance. Finally, a model may be strictly micromechanical, considering phenomena and details on length scales corresponding to fibre diameters or even less.

# **Empirical Approaches**

An empirical approach may be the only approach if the material being considered is "brand new" and no theory has been developed. However, use of an empirical approach requires a lot of experimental evidence and one should only use this approach when the load is known to be exactly as in the experiments used to obtain the data. The most common empirical creep models are the various power laws.

# Phenomenological Approaches

In the situation where substantial experimental evidence is present but it is not possible to explain all the observed phenomena in a physical sense, then the phenomenological approach seems to be the proper approach. This approach may be more simple than a micromechanical approach i.e. the complexity is not increased due to complex microstructural aspects. Examples of simple phenomenological models are the spring-dashpot models such as the Maxwell model or the Kelvin model. Two different approaches have given rise to some of the classic phenomenological models in nonlinear constitutive modelling. The first of these is the functional approach which was used by Green and Rivlin [34] and Pipkin and Rogers [86]. The other is the concept of internal state variables as used by Biot [7]. However, in his comprehensive study of these two approaches Pyrz [87] found that it seems there exists some links which put these two approaches into certain, although not complete, correspondence.

# Continuum Mechanics Approaches

The continuum mechanics approach involves by definition continuous quantities. This implies that sources of microstructural heterogeneity such as microdamage and positions of inclusions need to be averaged over some regions of the material in order to provide continuous quantities reflecting the actual microstructure.

The most widely used approaches are volume averaging of the field quantities or the use of unit cells with imposed continuity conditions on the tractions and displacements acting between the cells. The unit cell approach is capable of taking highly local phenomena into account, however, due to the cell structure a periodicity of the composite microstructure is often assumed. On the other hand the volume averaging approach does not yield as detailed information of the local quantities around the fibres, but is capable of taking real fibre distributions into account and is probably the approach which has been used the most, due to Eshelby [24] and his transformation

strains.

# Micromechanical Approaches

Depending on what the objective of the investigation is, the micromechanical model must incorporate a statistical descriptor of the quantity investigated. This is a necessity if the ultimate goal is an overall prediction of a composites' response to a loading situation. However, if a highly local phenomena, such as the influence of fibre debonding or interphase quality on the stress field, is the objective of investigation, a statistical description is not necessary. However, a larger degree of detail is gained on account of the models capability to predict overall behaviour. The approaches taken in the use of micromechanical modelling has a large span of variability ranging from shear lag models to finite elements.

Considering the advantages and disadvantages of all the aforementioned approaches this author believes that the greatest benefit is gained if they are combined. This is the fundamental approach in the present thesis.

# 1.2 Outline

In chapter 2 some basic principles of Raman spectroscopy is presented in terms of traditional electromagnetic theory. This is followed by some practical aspects of applying micro Raman spectroscopy, (MRS), to fibre strain measurements.

Chapter 3 is devoted to viscoelasticity. First, an introduction to some of the most general viscoelastic constitutive models is given, followed by a thorough description of the Schapery constitutive model which is used throughout this work. In the one dimensional situation a power law expression with one nonlinearising parameter is used to predict the creep and recovery strains, whereas relaxation is modelled using a power law expression and two nonlinearising parameters. Finally, this one dimensional constitutive model is extended to three dimensions.

In chapter 4 the experimental work is presented. In all the experiments the fibre strain is measured using MRS. The types of experiments include: Creep loading, creep loading and subsequent recovery, repeated loading and subsequent creep loading, creep loading at an elevated temperature, creep loading on specimens with misaligned fibres and finally the influence of interaction between fibres on the strain in a reference fibre.

Chapter 5 presents the basic ideas of two micromechanical stress/strain analysis methods for modelling the stress/strain field around an embedded fibre.

Two approaches have been proposed because experiments have shown different load transfer mechanisms for the two material combinations considered in this work.

The two methods are based upon integration of point forces along the fibre boundary thus giving the stress/strain field in an infinitely extended plane solid.

Finally, experimental results from the previous chapter is compared to both the theoretical approaches and to nonlinear finite element models, which include thermal residual strains generated during the manufacture process.

Chapter 6 deals with overall creep modelling. The method is based upon the Mori - Tanaka mean field approach and incorporates the effect of a slightly weakened interface through a modi-

1.2. Outline

fied Eshelby tensor. The interfacial parameter is calculated from experimental data obtained with MRS. Furthermore, fibre orientation is taken into account through a fibre orientation function, capable of simulating real fibre orientations.

Finally, chapter 7 presents the conclusions of the present work and outlines some suggestions for future work.

2

# Raman Spectroscopy

This chapter serves the purpose of giving a general introduction to Raman spectroscopy. Firstly, the theory of Raman scattering is outlined. Secondly, a description of the spectrometer and attached equipment is given. Then a literature study covering a broad range of applications of Raman spectroscopy has been undertaken in order to pinpoint the possibilities and limitations of Raman spectroscopy applied to viscoelastic composite investigations. Finally, the practical aspects of using Raman spectroscopy - in conjunction with composite measurements - are outlined.

In 1928 Raman and Krishan discovered that liquids scattered an incident beam of sunlight when exposed to it, [90], [91].

When transparent gases, liquids or solids are exposed to a monochromatic source of light most of the light is transmitted without any change, but a small fraction of it will be scattered. If an analysis is performed on the frequencies contained in the scattered radiation, it is found that besides the wavenumber of the incident light,  $\nu_0$ , there are wavenumbers of the type  $\nu' = \nu_0 \pm \nu_M$  present, meaning that Raman scatter is an inelastic scatter of light by matter. In the scattered spectrum the "new" wavenumbers, the Raman bands, constitutes the Raman spectrum. It is important to emphasize that the Raman effect does *not* depend on the light being monochromatic. However, the detection is much easier when the light is monochromatic.

Even though the Raman effect has been known for a long time it is only within the last three decades that the use of the technique has become commercially available. This is due to the fact that the Raman effect is very weak, typically the scattered intensity is only  $10^{-8}$  of the incident radiation and thus very sensitive measuring equipment and highly intense light sources are necessary. When commercially available lasers were developed, the basis for applied Raman spectroscopy was founded.

Raman spectroscopy has a wide range of applications, though its application in mechanical engineering and material science is quite new. In chemistry Raman spectroscopy has been used extensively for investigation of reaction processes between gases and curing reactions in polymers. In the field of biology it is possible to use the Raman technique to detect if cells contain enough beta-carotene to be viable. Finally, the technique has great potential in criminal investigations, where it can be used to detect various kinds of drugs and explosives.

# 2.1 Theoretical Raman Scattering

When a solid is exposed to an incident radiation, the molecules in the solid may change their amount of energy either by loosing or gaining energy. If the molecules are gaining energy, meaning that the incident radiation looses energy, the type of scatter is called Stokes scattering, while the opposite situation is called anti-Stokes scattering and if no change in energy takes place the scatter is called Rayleigh scattering [59].

The change in energy is proportional to the change of wavenumber, implying that the Raman bands are characterised by the magnitude of its wavenumber *shift*,  $|\Delta \nu|$ , from the incident wavenumber, where  $|\Delta \nu| = |\nu_0 - \nu'|$ .

At room temperature most molecular vibrations are in the ground state and anti-Stokes scattering is less likely to occur than the Stokes scattering, resulting in Stokes scattering being more intense. For this reason Stokes scattering is usually studied in Raman spectroscopy.

In order to describe the Raman effect, it is necessary to give a brief introduction to the theory of electromagnetic radiation. Generally, there are three ways to describe the Raman effect:

1) by quantum mechanics which states that radiation is emitted or absorbed due to a system changing its state of energy between two discrete energy levels, meaning that the radiation is quantised with the energy in discrete photons. To describe spectroscopy by quantum mechanics, the radiation and the molecule are treated as a complete system and the energy transferred between the radiation and the molecule is analysed as a consequence of the interaction between them.

2) The second approach used to describe spectroscopy is the perturbation theory, which treats the radiation classically, but the radiation is now considered as a source of perturbation of the energy levels of the scattering system. Quantum mechanics is subsequently used to investigate the transitions of energy in the perturbed system and the resulting scatter.

3) The third approach to describing spectroscopy is by the classical eletromagnetic theory, which will be outlined in the following section.

### Introduction to Electromagnetic Radiation

Consider a plane harmonic wave of electromagnetic radiation travelling in free space. Choosing the axis of propagation as the z-axis and assuming that the electric vector lies in the xz-plane, the wave can be illustrated as in figure 2.1.

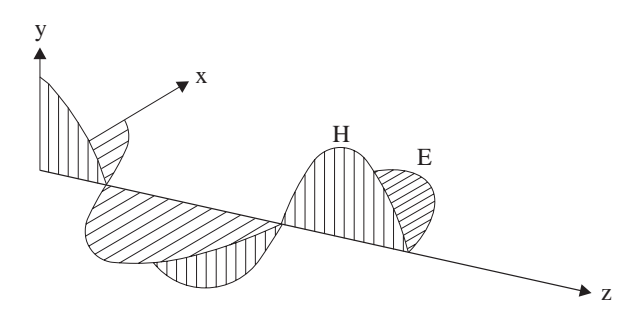


Figure 2.1: A plane harmonic wave of electromagnetic radiation.

According to the laws of Maxwell the electric field vector, **E**, will have only one component, which can be represented as

$$E_x = E_{x0} \cos \left\{ \omega \left( t - \frac{z}{c} \right) + \theta_x \right\} \tag{2.1}$$

where  $E_{x0}$  is the amplitude of  $E_x$ ,  $\omega$  is the angular frequency, t is time, z is the position along the z-axis, c is the velocity of propagation and  $\theta_x$  is the phase angle.

The other component of electromagnetic radiation is the magnetic field vector,  $\mathbf{H}$ , which is perpendicular to the electric field vector. In the plane situation the magnetic field vector has only one component which can be expressed as

$$H_y = H_{y0}\cos\left\{\omega\left(t - \frac{z}{c}\right) + \theta_y\right\} \tag{2.2}$$

where  $H_{y0}$  is the amplitude of  $H_y$  and  $\theta_y = \theta_x$  in the situation shown in figure 2.1.

# The Dipole

The dipole is the source of Rayleigh and Raman scattering and as such it is a very important quantity in the theoretical description of Raman scatter. The major contributor to Raman scatter is the electric dipole and for this reason the magnetic dipole will be omitted here. The electric dipole arises when two charges, equal in magnitude and of opposite sign, are displaced relatively to each other. Thus the dipole moment,  $P_i$  which is a vector, is defined by

$$P_i = qs_i (2.3)$$

where  $s_i$  is the vector pointing from the charge -q towards the charge q.

Imagine a molecule with a given distribution of electrons. If the molecule is in its equilibrium configuration it vibrates with a certain frequency. When the molecule is exposed to an external electric field, the distribution of electrons is changed and dipoles are created. These dipoles can oscillate and cause radiation. The frequency with which the dipoles oscillate, are determined by the frequency of the electric field and the frequency of the molecular vibration. It readily follows that the harmonic vibration of a dipole vibrating with the angular frequency  $\omega$ , can be expressed as

$$P_i = P_{i0} \cos \omega t \tag{2.4}$$

where  $P_{i0}$  is the amplitude vector of the vibrating dipole.

### The Polarisability tensor

Light scattering phenomena can be described in a classical manner in terms of the electromagnetic radiation caused by the dipoles induced in the scattering system by electric and magnetic fields of the incident radiation.

The induced electric dipole,  $P_i$ , can be described in terms of a power series of the electric field,  $E_k$  as

$$P_i = P_i^{(1)} + P_i^{(2)} + P_i^{(3)} + \dots {2.5}$$

where  $P_i^{(j)}$  are given by

$$P_{i}^{(1)} = \alpha_{ik} E_{k}$$

$$P_{i}^{(2)} = \frac{1}{2} \beta_{ikl} E_{k} E_{l}$$

$$P_{i}^{(3)} = \frac{1}{6} \gamma_{iklm} E_{k} E_{l} E_{m}$$
(2.6)

where  $\alpha_{ik}$ ,  $\beta_{ikl}$  and  $\gamma_{iklm}$  are tensors. This stems from the fact that, in general, the direction of the dipole is not coincident with that of the electric field causing it.

More precisely the tensor  $\alpha_{ik}$  is a second order tensor and is termed the *polarisability tensor*. Its components has units of  $C \cdot m^2/V$ . The tensor  $\beta_{ikl}$  is a third order tensor and is called the *hyperpolarisability tensor* and its components has the units of  $C \cdot m^3/V^2$ . Finally the tensor  $\gamma_{iklm}$  is a fourth order tensor and is called the *second hyperpolarisability tensor*, and its components has units of  $C \cdot m^4/V^3$ .

These tensors can be interpreted as a measure of the ease with which the electrons can be displaced and thereby create a dipole under the action of an electric field.

Typically the magnitudes of the components of  $\alpha_{ij}$ ,  $\beta_{ikl}$  and  $\gamma_{iklm}$  are  $10^{-40}$  C· m<sup>2</sup>/V,  $10^{-50}$  C· m<sup>3</sup>/V<sup>2</sup> and  $10^{-61}$  C· m<sup>4</sup>/V<sup>3</sup>, respectively [59]. For this reason the tensors  $\beta_{ikl}$  and  $\gamma_{iklm}$  are usually neglected when considering Raman scatter.

This leads to the following expression relating the electric field and the dipole

$$P_i = \alpha_{ij} E_j \tag{2.7}$$

where i, j = 1, 2, 3, corresponding to the three directions in a cartesian coordinate system.  $\alpha_{ij}$  is a symmetric tensor,  $\alpha_{ij} = \alpha_{ji}$ , meaning that there are only six different components and obviously  $\alpha_{ij}$  transforms in a manner analogous to the stress and strain tensors

$$\alpha_{l'k'} = b_{l'i}b_{k'j}\alpha_{ij} \tag{2.8}$$

where  $b_{l'i}$  and  $b_{k'j}$  are direction cosines between the axis l'i and k'j respectively. The polarisability tensor also has invariants, the first is the mean polarisability defined as

$$a = \frac{1}{3}\alpha_{kk} \tag{2.9}$$

and the second invariant is defined as

$$\gamma^2 = \frac{1}{2} \left\{ (\alpha_{11} - \alpha_{22})^2 + (\alpha_{22} - \alpha_{33})^2 + (\alpha_{33} - \alpha_{11})^2 + 6(\alpha_{12}^2 + \alpha_{23}^2 + \alpha_{31}^2) \right\}$$
(2.10)

As in three dimensional plasticity, the Mises yield surface is a cylinder, the second invariant of the polarisability tensor can also be given a graphical representation, which is an ellipsoid. When the cartesian coordinate axes are coincident with the ellipsoidal axes, these axes correspond to the *principal* axes, which is analogous to the principal stress and strain axes in the theory of elasticity.

# Classical Raman and Rayleigh Scattering

As a molecule vibrates, the atoms and thus the electron cloud vibrates which causes the oscillating dipole. As a simple example, consider figure 2.2.

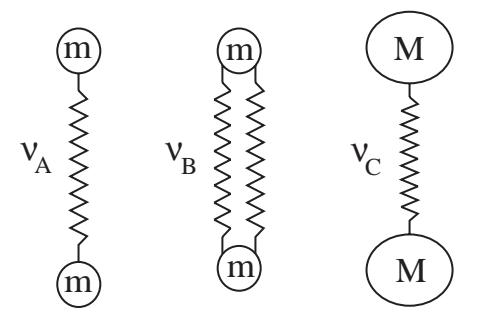


Figure 2.2: Three different molecules. A) Single bond between atoms, B) Double bond, C) Larger masses.

The figure shows the different vibrational frequencies of different molecules. The stiffness of the bonds will influence the frequency of the Raman scatter. This is indeed the case because the stiffer the bond, the smaller the deformation of the material and thus the magnitude of the dipole is smaller, because of the smaller separation between the charges. Larger masses influence the vibrational frequency due to the fact that a larger atom contains more electrons and thus a larger amount of charge causing the dipole.

This leads to the theoretical description of Raman and Rayleigh scatter based on the polar-isability tensor.

Consider the scattering system consisting of one molecule, in which the nuclei may vibrate around the equilibrium positions but no rotations take place.

When both vibration and rotation is considered the polarisability tensor is expected to be a function of the nuclear coordinates. Since only vibrations are considered the nuclear coordinates are termed *normal* coordinates and are given by

$$Q_k = Q_{k0}\cos(\omega_k t + \delta_k) \tag{2.11}$$

where  $Q_k$  is the normal coordinate amplitude,  $\omega_k$  is the vibrational frequency associated with the k'th vibration mode, and  $\delta_k$  is the phase angle.

It is now possible to describe the variation of the polarisability tensor with vibration as a Taylor series with respect to the normal coordinates, [59]

$$\alpha_{ij} = (\alpha_{ij})_0 + \sum_k \left(\frac{\partial \alpha_{ij}}{\partial Q_k}\right)_0 Q_k + \frac{1}{2} \sum_{k,l} \left(\frac{\partial^2 \alpha_{ij}}{\partial Q_k \partial Q_l}\right)_0 Q_k Q_l + \dots$$
 (2.12)

where  $(\alpha_{ij})_0$  is the value of  $\alpha_{ij}$  in the equilibrium configuration,  $Q_k, Q_l$  ... are the normal coordinates associated with vibrational frequencies  $\omega_k, \omega_l$  ..., where summations are to be taken over all the normal coordinates. Omitting higher order terms in the Taylor series, equation (2.12) can be written as

$$(\alpha_{ij})_k = (\alpha_{ij})_0 + (\alpha'_{ij})_k Q_k \tag{2.13}$$

where  $(\alpha'_{ij})_k = \left(\frac{\partial \alpha_{ij}}{\partial Q_k}\right)_0$ .

When the molecule is exposed to an electromagnetic radiation of the form

$$E_i = E_{i0}\cos\omega_0 t \tag{2.14}$$

the induced dipole can be expressed as

$$P_i^{(1)} = (\alpha_{ij})_k E_j \tag{2.15}$$

Inserting equations (2.14), (2.13) and (2.11) into equation (2.15), leads to

$$P_i^{(1)} = (\alpha_{ij})_0 E_{i0} \cos \omega_0 t + (\alpha'_{ij})_k E_{i0} Q_{k0} \cos \omega_0 t \cos(\omega_k + \delta_k)$$
(2.16)

 $(\alpha'_{ij})_k$  is also known as the "Raman tensor" and is essential when considering polarised Raman spectroscopy.

After using some mathematical manipulations equation (2.16) can be expressed as, [59]

$$P_i^{(1)} = P_i^{(1)}(\omega_0) + P_i^{(1)}(\omega_0 - \omega_k) + P_i^{(1)}(\omega_0 + \omega_k)$$
(2.17)

The first term in equation (2.17) give rise to scattering with frequency  $\omega_0$ , and so accounts for Rayleigh scattering. The second term give rise to scattering with frequency  $\omega_0 - \omega_k$  and thus accounts for Stokes-Raman scattering. The last term give rise to scattering with vibrational frequency  $\omega_0 + \omega_k$  and thus accounts for anti-Stokes Raman scattering. The three kinds of scattering occurs when:

Rayleigh scattering: arises from the dipole oscillating at vibrational frequency  $\omega_0$ , when the molecule is exposed to the electric field which itself oscillates with frequency  $\omega_0$ .

Raman scattering: arises from the dipoles oscillating with frequency  $\omega_0 \pm \omega_k$ . This occurs when the dipoles are oscillating with frequency  $\omega_0$  and these are affected by the molecule oscillating with frequency  $\omega_k$ .

Thus one of the main conditions for a material to be Raman active is that the partial derivative of the polarisability tensor, with respect to the normal coordinates, must have non-zero components. This implies that there must be a change in the polarisability with the vibration of the molecule. As a consequence of this fact polarised Raman spectroscopy can be used to conduct measurements in a polymer in a way similar to classical photoelasticity.

As mentioned before different molecules possesses different Raman frequencies. Some of these frequencies will shift under an application of load. This is quite easy to show. Consider figure 2.2. The following system of equations can be established to determine the eigen frequency of the system

$$\det \begin{bmatrix} (-m'\omega^2 + k') & -k' \\ -k' & (m'\omega^2 + k') \end{bmatrix} = 0$$
 (2.18)

where m' and k' are the equivalent mass and stiffness of the system, respectively. In general this equation can be written in a compact form as

$$det(\mathbf{B} - \omega^2 \mathbf{I}) = 0 \tag{2.19}$$

which constitutes a matrix equation in which I is the identity matrix and B incorporates both the equivalent mass and stiffness.  $\omega$  is the eigen frequency of the system and det denotes the determinant of the matrix. If a force is applied to the system in figure 2.2 the resulting displacement causes a larger force between the atoms. This additional force is analoguous to a change,  $\Delta \mathbf{B}$ , in the matrix B. Now the equation to determine the frequency reads [96]

$$det\left((\mathbf{B} + \Delta\mathbf{B}) - \Omega^2\mathbf{I}\right) = 0 \tag{2.20}$$

where the frequency shift is obtained as  $\Delta \nu = \Omega - \omega$ . The derivations above show that application of a load causes a change of frequency. This phenomenon provides the basis for strain measurements in e.g. the reinforcing fibres in fibre composites. All that is required for the strain measurements is a calibration curve relating frequency shift and applied strain as will be shown later.

# 2.2 Experimental Setup

In this section parts of the experimental setup are described. First a description of the Raman spectrometer is given, followed by a description of the straining rig which has been constructed in order to apply the various load histories.

### The spectrometer

Attached to the spectrometer is a modified Olympus microscope which serves to locate the desired area in the sample and to enhance resolution. The laser beam is directed on to the sample through the optics of the spectrometer and then through the microscope. Using this experimental setup it is possible to focus the laser spot to a diameter of about 1-2  $\mu$ m and record Raman spectra from this area. The scattered radiation from the sample goes back through the microscope and into the spectrometer as shown in figure 2.3. An additional description of some of the parts follows and a photograph of the spectrometer is shown in figure 2.4.

- a) The laser alignment mirror is used to make sure that the laser is perfectly aligned.
- b) The objective lens and the pinhole serves to provide a well defined laser spot.
- f) The beam splitter allows only Raman scattered light to pass through. This means that the CCD camera will only be exposed to Raman scattered light and not to Rayleigh scattered light.
- g) The polariser is fundamental for determining vibration modes and symmetry of vibrations. This is due to the fact that the intensity of the actual vibration changes when changing the polarisation of the excitation radiation.

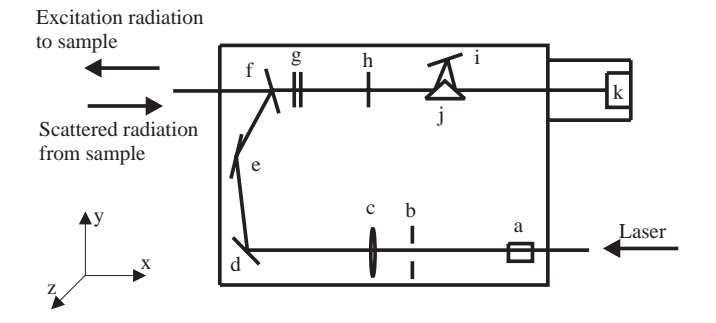


Figure 2.3: The major parts of the spectrometer. a) Laser alignment mirror. b) Objective lens and 10 μm pinhole. c) Spot focus adjustment lens. d) Adjustable mirror. e) Fixed mirror. f) Beam splitter. g) Polariser. h) Spatial filter. i) Grating. j) Isosceles triangular mirror. k) CCD chip.

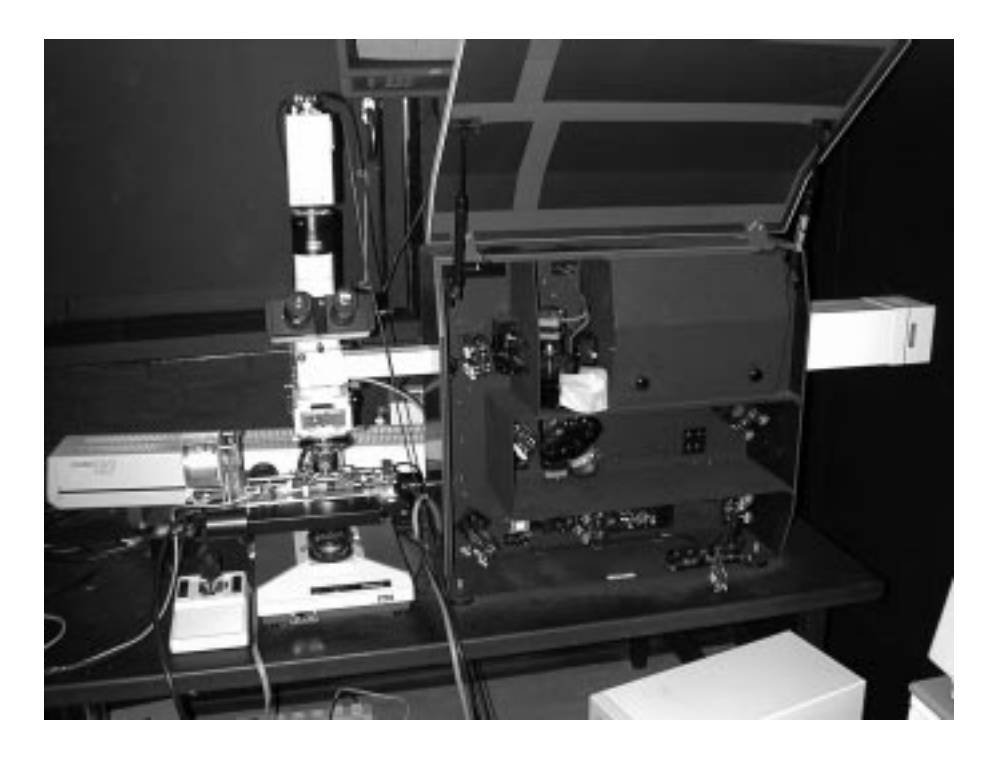


Figure 2.4: The spectrometer.

- **h**) The spatial filter allows the examination of samples where the region or particle of interest cannot be physically isolated from the remainder of the sample. Spectral interferences from the surrounding area can be minimised or eliminated by isolating the region of interest with a spatial filter.
- i) The grating consists of a series of grooves ruled on a hard glassy or metallic material. These grooves are extremely closely spaced, spacings of 1  $\mu$ m are not unusual, [41]. The grating disperses the scattered light and then passes it through a narrow slit so that the light passing through to the detector at any time has a very narrow band width and may be considered as essentially monochromatic. The spectrum is produced by rotating the grating so that a continuously changing wavelength is presented to the detector.

- j) The different wavelenghts from the grating are exposed to different areas of the CCD chip by the triangular mirror.
- k) The CCD chip is the device which detects the scattered radiation and produces the spectrum. It is a two-dimensional array of silicon photosensors, each photosensor usually being referred to as a pixel. When radiation falls on a pixel, photoelectrons are produced in numbers proportional to the intensity of the radiation. A typical CCD contains about 2000 columns and 800 rows of pixels, where the area of each pixel is  $15 \ \mu m \times 15 \ \mu m$ .

The spectrometer is operated by appropriate software installed on a PC. The PC serves both as a data collector and as controller of filters and motors in the spectrometer. Furthermore, the PC controls the fully automatic motorised xyz-stage, the heating device and the straining rig. Additional software provides the tools for data analysis.

# The Straining Rig

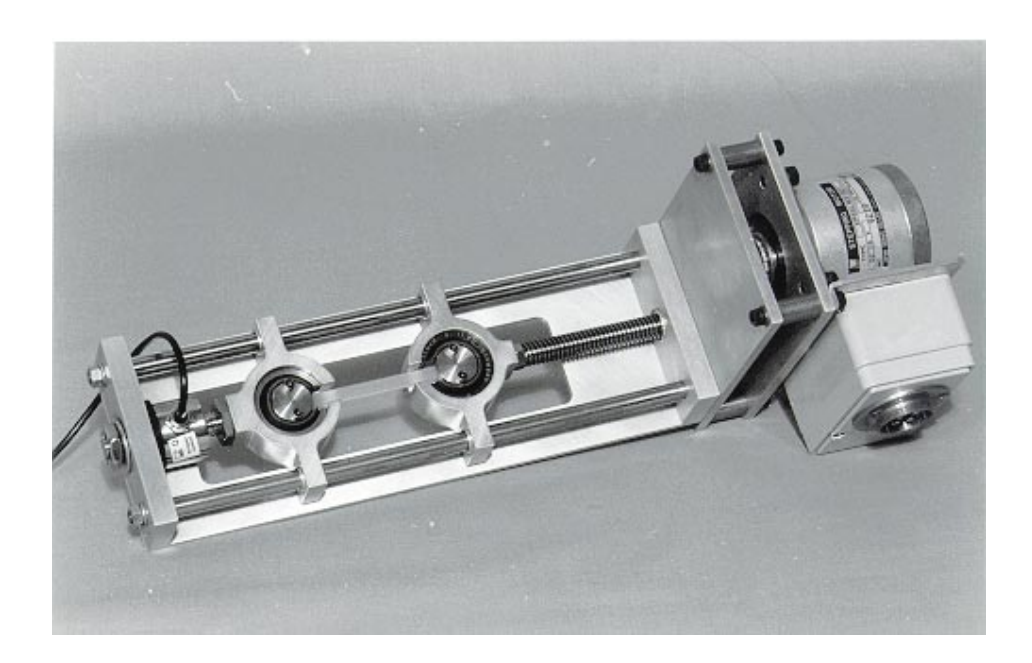


Figure 2.5: The straining rig.

The straining rig was purpose build to fit under the Raman microscope and is shown in figure 2.5. The straining rig is constructed as a conventional tensile testing machine with two columns carrying the load. Two plates at each end of the rig serve as base for the load transducer and the gearbox, respectively. The gear box is belt driven in order to minimise noise and vibrations transmitted to the microscope. The specimen is held by two guides in which spherical bearings are mounted to ensure that no bending effects are applied to the specimen. Clamps with a shape exactly like the specimens ends are mounted in these bearings. This ensures that no stress concentrations are introduced into the specimens. One of the guides is connected to the gear box via a spindle and can slide along the columns in slide bearings and thereby provides the linear displacement that creates the tension in the specimen. A stepper motor with a resolution of  $1.8^{\circ}$  per step is connected to the gear box. This resolution gives a linear displacement of 4  $\mu$ m per

step. The load transducer is connected to a strain gauge amplifier and a data acquisition module. The signal from from the strain gauge amplifier is used to control the stepper motor, thus the straining rig is force controlled, allowing application of different loading histories, such as step loading, creep loading or conventional tensile testing.

# 2.3 Applications of MRS

This section includes a literature survey of papers covering a broad range of MRS applications in order to pinpoint the possibilities and limitations of the technique and serves as a basis for specifying the experimental programme. Additionally, the section describes some of the practical details concerning strain measurements with MRS.

Even though the Raman effect has been known for quite some time it was not used for strain measurements until the late 1970's. The idea of using Raman spectroscopy for strain measurements in crystalline materials initiated when Robert Young and David Batchelder was discussing twinning of polydiacetylene crystals, during a coffee break at Queen Mary and Westfield College in London, [135]. After the initiation of the concept of strain measurement with MRS, Batchelder and Bloor [4], showed that polydiacetylene crystals posseses four strain dependent Raman frequencies, situated at 2080 cm<sup>-1</sup>, 1480 cm<sup>-1</sup>, 1200 cm<sup>-1</sup> and 950 cm<sup>-1</sup>. They also showed that the strain sensitivity of these four peaks are: -20 cm<sup>-1</sup>/%, -9.9 cm<sup>-1</sup>/%, -0.4 cm<sup>-1</sup>/% and -7.6 cm<sup>-1</sup>/%, respectively.

Later on Galiotis et~al.~[31] found that aramid fibres possess a strain sensitive Raman band as well, situated at 1610 cm<sup>-1</sup>. Later on these findings were refuted by other workers, but the disagreement was finally resolved by Young et~al.~[132] who found that high powered lasers (> 1W) caused premature failure of aramid fibres. Young et~al. also found the strain sensitivity to be -4.1 cm<sup>-1</sup>/%.

The first researchers to report strain induced frequency shifts in carbon fibres were Robinson et al., [92]. They showed that carbon fibres usually possess two major first order Raman bands at 1360 cm<sup>-1</sup> and 1580 cm<sup>-1</sup> which shift to a lower wavenumber under the application of a tensile load. The strain sensivity of these bands are approximately -7 cm<sup>-1</sup>/% and -9 cm<sup>-1</sup>/%.

After these pioneering investigations it was obvious that the Raman technique is a powerful tool for in-situ non destructive investigations of various micromechanical phenomena in composite materials.

Huang and Young [43] investigated the interfacial behaviour of high temperature cured carbon fibre/epoxy resin model composites. They evaluated the interfacial shear strength by Raman spectroscopic analysis of the traditional fragmentation test. They found that the interfacial shear strength was higher in the hot-cured specimens than in the equivalent cold-cured specimens. It was found that the stress transfer from the fibre to the matrix was well modelled by the Cox shear-lag theory at low levels of applied stress. At higher levels of applied stress the stress transfer mechanism is a combination of elastic shear stress in the bonded region and frictional shear stress in the debonded region. Also in the debonded region a higher shear stress was found in the hot-cured specimens, due to the effect of thermal expansion mismatch.

Paipetis and Galiotis [79] investigated the effect of fibre sizing on the stress transfer efficiency in carbon/epoxy model composites. They found that the interfacial shear strength was higher

in the sized system than in the unsized. The interfacial shear strength determined from the Kelly-Tyson model was found to be 42 MPa which compares well to the shear yield strength of the resin.

The residual stress in the fibre was measured in 20 identical specimens and found to be independent of the sizing and was of the order of 2000 MPa. However, upon loading mode II debonding was observed in the unsized system whereas the sized system sustained a higher shear stress leading to a mixed mode cracking.

Another application of Raman spectroscopy is monitoring interaction effects between fibres in 2-dimensional model composites. Such investigations have been undertaken by Schadler et~al. [95] and Chohan and Galiotis [15] on carbon/epoxy specimens. Wagner et~al. [117] investigated interaction effects in model composites with Kevlar fibres. Grubb et~al. [35] investigated the fiber interactions in hybrid model composites by embeddeding one carbon fibre along with two Kevlar fibres on each side in an epoxy resin. Generally, the interaction distance is found to be  $\approx 5$  times the carbon fibre diameter. The strain concentration factor is approximately 1.5 which is less than predicted by the applied shear lag analysis. In the Kevlar specimen the strain concentration factor is around 1.1 which is due to the fact that Kevlar fibres are not as brittle as carbon fibres but instead display a region of damage which carries no load. Furthermore, these investigations showed that axial stresses in the matrix is not negligible as assumed by the shear-lag theories.

Strain measurements in polymeric fibres have been undertaken by Young and Yeh [133], who investigated the mechanical straining of PET fibres and found that the Raman frequency shift was stress related.

Grubb and Li [36] investigated the molecular stress distribution and creep of high-modulus PE fibres and found that the molecular structure undergoes complex changes during creep.

Hu et al. [45] used the strain sensitivity of diacetylene to measure the strain in a diacetylene/urethane copolymer at various angles of polarization and found that the results were in agreement with the theory of elasticity.

Rodriguez-Cabello *et al.* [93] investigated the chain deformation of uniaxially stretched bulk PE and found that the transfer of the load on the polymer backbone was not effective until the sample showed a high degree of orientation in the stretching direction.

Mermet et al. [67] investigated the plastic deformation of PC and found that the cohesive regions in the polymer was affected differently and that the shape of the spectra were different when the temperature was lower and higher than the glass transition temperature, respectively. This is due to the larger mobility of the molecular chains at temperatures above the glass transition temperature.

In all the afore mentioned studies the Raman frequency shifts were used to determine the strains and molecular stress distribution. This is possible because of the highly orientated polymer chains. The stretching of the polymer chains causes the polymer backbone to be stretched, which again causes the frequency shifts.

However, such opto-mechanical behaviour is much more difficult in isotropic polymers because they show no stress or strain induced frequency shifts until a very large strain is applied. The reason is, that initially the polymer chains are more or less randomly oriented in the bulk polymer, but when the load level is increased a larger degree of orientation is observed for the polymer chains and the same tendencies as for the fibre can be observed. As seen in [67] both a frequency shift and a broadening of the Raman band occurs for deformed PC specimens. Unfortunately the deformed specimens are strained to above 90 %, which is not appropriate for the present study.

The former investigations are based on the strain dependent frequency shifts of the fibres. However, Raman spectroscopy can also be used for other investigations than strain measurements.

By comparing the shape and intensities of the various bands in the Raman spectra it is possible to determine the fractions of crystalline and amorphous phases in a semi crystalline polymer. This technique has been used by Keresztury and Földes [50] in an analysis of polyethylene, and by Nielsen and Pyrz [74] in an investigation of the crystalline phase influence on thermal strains in carbon fibre/polypropylene matrix composites during cool down.

To measure the strains in isotropic polymers another feature of the Raman spectra needs to be taken in to consideration. Namely the dependence of polarization on the incident and scattered light on the frequency shift. The reason is that for polymers of low orientation, observations with different polarization combinations are selectively sensitive to chains oriented in different directions and these chains are in different states of stress/strain. This leads to the possibility of obtaining information about the distribution of stress/strain in chains at different orientation to the loading direction, [75]. Applying a known stress state to the polymer and recording the spectra yields the "reference" spectra. These spectra are compared to the spectra obtained from the vicinity of an embedded fibre and the strains around an embedded fibre can be determined. However, at present, this technique seems only to be applicable to polymers which are also suited for classical photo elasticity, i.e. amorphous birefringent polymers.

In spite of the large number of papers concerning strain measurements on composites the Raman technique has not been used on composites during creep. To the authors knowledge only a few investigations concerning viscoelasticity in composites have been conducted.

Sengonul and Wilding [108] used the Raman technique to monitor viscoelasticity in ultra high modulus polyethylene, (UHMPE), fibres. They used the Raman spectroscopy to interpret the time dependent behaviour of UHMPE and subsequently model these effects by simple spring/dash-pot models. These models are used to predict the Raman frequency shifts on strain. The parameters in the models are determined by best fit to experimental data. The creep behaviour is quite well modelled, but the relaxation modelling fails to reproduce the observed phenomena.

A theoretical investigation of the stress induced shifts for isotropic and uniaxially orientated PET have been carried out by Bower *et al.* [9] and an experimental investigation by Lewis *et al.* [54]. They found that neither a strain or stress governed model fits the experimental data well. Most important is the conclusion that the observed shifts depend only on the applied stress and do not change as the sample creeps.

Based on the previous literature study it was decided that the experimental approach should be based on fibre strain measurements using MRS. Additionally, traditional optical microscopy and SEM will be used when appropriate.

In all the Raman measurements the incident laser light was polarised in the yz-plane, see figure 2.3 and 2.4, and the loading direction of the straining rig was parallel to the x-direction. Equipment for changing the polarisation direction of the incident laser light was only purchased recently and has not been used in the present work.

# Determination of Strain Sensitivity of Carbon Fibres

To measure the strains in a carbon fibre composite it is necessary to know which of the Raman bands are strain sensitive. For HM PAN based carbon fibre there are generally three main Raman bands. These are  $\nu_1 \approx 1360 \text{ cm}^{-1}$ ,  $\nu_2 \approx 1580 \text{ cm}^{-1}$  and  $\nu_3 \approx 2700 \text{ cm}^{-1}$ . The 1360 cm<sup>-1</sup> frequency is an  $A_{1g}$  vibration mode due to crystal boundary regions in the graphite and

has been attributed to a crystalline size effect. The second frequency is attributed to the in-plane stretching of the C-C bonds in the fibre and is due to an  $E_{2g}$  vibrational mode in the graphite crystals. The last frequency at 2700 cm<sup>-1</sup> is a second order band [92]. The three frequencies in the spectrum of the used carbon fibres are shown in figure 2.6.

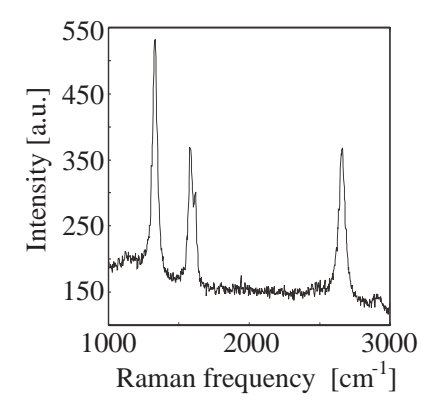


Figure 2.6: The three strain sensitive Raman peaks in a HM carbon fibre.

In this analysis high modulus carbon fibres of the type Tenax-J from Toho Rayon are used. The frequency used for the strain measurements is the 2660 cm<sup>-1</sup> peak, due to its high strain sensivity.



Figure 2.7: The bending rig.

To determine the peak position dependence upon strain a simple bending test is performed. A small straining rig have been constructed, consisting of a clamp and a micrometer dial gauge. A carbon fibre is glued on top of a polymeric beam and inserted into the clamp in the bending rig. The dial gauge is used to apply a known deformation to the cantilever beam, and from the beam theory the strain in the fibre can be determined from the expression

$$\varepsilon = \frac{3h\delta}{2L^2} \left( 1 - \frac{x}{L} \right) \tag{2.21}$$

where h is the height of the beam,  $\delta$  is the deflection, x is the distance from the clamped end to the point of measurement and L is the length of the beam. The bending rig is shown in figure 2.7.

The tensile strain sensitivity of the fibres was found to be -23 cm<sup>-1</sup>/%, which is consistent

28 2.4. Summary

with values reported by Young [134] and the compressive strain sensitivity has been found by Nielsen and Pyrz [74] to be -20 cm<sup>-1</sup>/%. The experimental values along with the fitted straight line are shown in figure 2.8. From measurements on unloaded carbon fibres in free air, the frequency at which the fibres are unstrained has been found to be 2661 cm<sup>-1</sup>.

Galiotis and Batchelder [30] found that the 2660 cm<sup>-1</sup> Raman band is nonlinear for strains larger than 0.6 %. However, strains of this magnitude will not appear in the present work and therefore this nonlinearity is disregarded. In the present study only one fibre type have been used but in the discussion of strain sensitivity it is important to mention that the strain sensitivity also depends on fibre moduli. Huang and Young [44] found that the strain sensitivity of both PAN and pitch based carbon fibres increased linearly with increasing fibre moduli. Furthermore, they found that the stress dependence of Raman shift was independent of fibre modulus.

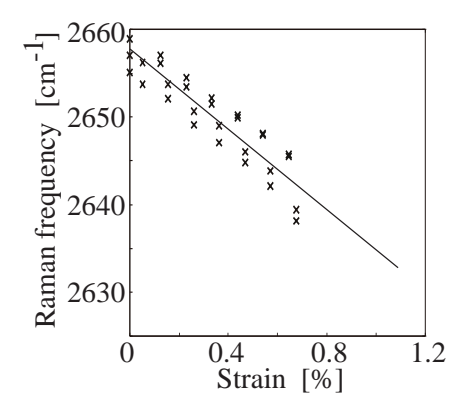


Figure 2.8: The strain sensitivity of the carbon fibres, measured on different fibres.

# 2.4 Summary

The basic theory of Raman scattering has been outlined and it has been shown - by simple mechanical considerations - that application of a load will shift some of the Raman bands in crystalline materials. The relationship between applied strain and wavenumber shift for the used fibres have been found to be -23 cm $^{-1}$ /% which is consistent with values found in the litterature. Based on a literature study the experimental programme includes fibre strain measurements using MRS together with SEM and optical microscopy when appropriate.

3

# Viscoelasticity

This chapter outlines the viscoelastic constitutive model applied to the polypropylene matrix considered in this thesis.

The chapter is divided into three major parts. One discusses some of the theoretical approaches used to describe viscoelastic constitutive behaviour. The major effort is placed on the Schapery model, because this model will be used in the theoretical modelling. Next, the parameters in the Schapery model are determined from creep and relaxation data and finally the one dimensional Schapery model is extended to three dimensions.

Polymeric materials are characterised by the long chain like nature of their molecules. Most polymers in this area of interest have molecules based on a carbon backbone with each carbon atom being linked to the two adjacent carbon atoms by covalent bonds.

The chains in the molecular structure of a polymer may be linear in the sense that they form long threads, they may be branched or they may be crosslinked in which case the chains are linked together at various points along their length. In the latter case the molecular chains may form a giant molecular network and constitutes a thermosetting polymer.

Thermoplastic polymers can appear as amorphous and semi crystalline. The semi crystalline polymers also form crosslinks, although these are usually based on secondary bonds such as hydrogen bonds and Van der Waal bonds, whereas the crosslinks in thermosetting polymers are covalent.

The deformation mechanisms in a thermoplastic polymer are mainly due to extension in the molecular chains and relative motion between adjacent chains. This relative motion is prohibited in the thermosetting polymers due to the strong crosslinks between the chains.

Upon heating, the secondary bonds in thermoplastic polymers will be broken, causing a large relative motion between the chains and a decrease in stiffness of the polymer, which can be of several orders of magnitude. These physical and molecular changes in the polymer are the major contributors to the viscoelastic behaviour of thermoplastic polymers.

A study of the viscoelastic properties of composite materials is of primarily interest because of the considerable number of composites that have a polymeric matrix. This is the case for most fibre composites where the most common polymer matrices are epoxy for unidirectional fibre composites, polyester for chopped fibre composites and a wide range of thermoplastic polymers for injection moulded composites. Because of the time dependent properties of the polymer the composite will also exhibit time dependence and these effects are magnified at elevated temperatures.

In the following some viscoelastic models will be presented and finally the basis of the Schapery model will be outlined.

# 3.1 Viscoelastic Constitutive Models

The most general description of a viscoelastic material is to state the relation between stress and strain as

$$\varepsilon(t) = \mathcal{J}_{ijkl} \left[ \sigma(\tau) \right]_0^t$$
  

$$\sigma(t) = \mathcal{G}_{ijkl} \left[ \varepsilon(\tau) \right]_0^t$$
(3.1)

where  $\mathcal{J}_{ijkl}$  is the fourth order anisotropic creep tensor, (the creep compliance) and  $\mathcal{G}_{ijkl}$  is the fourth order anisotropic relaxation tensor, (the relaxation modulus).

In order to reproduce the observed material deformation behaviour, the viscoelastic constitutive model must be able to reproduce history dependence in the sense of fading memory, since this feature is possessed by most polymeric and composite materials. Indeed, some composite materials even possess permanent memory, manifesting itself as hysteresis under repeated loading or as plasticity under static loading.

The fading memory characteristic is that the material responds less to events in the distant past in its history than to recent ones. In the linear situation this means that the rate of change of the relaxation and creep tensors are affected less as time increases, thus the magnitude of these tensors are continuously decreasing with increasing time. In the nonlinear situation it is somewhat more complicated and demands the existence of the Fréchet differential, [17].

The following discussion of constitutive models will be concerned with some of the integral based constitutive models.

The most general formulation of the relations above is that due to Green and Rivlin [34]. This approach is basically a polynomial expansion of the stress history, expressing the strain as linear functionals. In the one dimensional case this constitutive relation can be stated as

$$\varepsilon(t) = \int_0^t \phi_1(t - \tau_1) \dot{\sigma}(\tau_1) d\tau_1 + \int_0^t \int_0^t \phi_2(t - \tau_1, t - \tau_2) \dot{\sigma}(\tau_1) \dot{\sigma}(\tau_2) d\tau_1 d\tau_2 + \int_0^t \int_0^t \int_0^t \phi_3(t - \tau_1, t - \tau_2, t - \tau_3) \dot{\sigma}(\tau_1) \dot{\sigma}(\tau_2) \dot{\sigma}(\tau_3) d\tau_1 d\tau_2 d\tau_3 + \dots$$
(3.2)

where  $\phi_i$  are creep compliances and  $\tau_i$  are the times at which the stresses are applied.

It is seen that the first term is the linear Boltzmann superposition integral. Furthermore, it is important to notice that this model is not capable of modelling the response of an ageing material because the kernels are functions of  $(t - \tau_i)$  only and not of  $(t, \tau_i)$ , i.e. the kernels are invariant with respect to time translation. The second and higher order terms account for magnitude and interaction nonlinearity between different loading components. The kernels can be determined by application of stepwise loading and the number of kernels corresponds to the number of steps.

Even though this model is very general, it is not suited for application. If the material of interest exhibits strong nonlinearities several terms are needed. To determine  $\phi_i$  in equation (3.2) 78 experiments are needed, whereas a third order approximation of the three dimensional

case involves 12 kernels and according to Lockett, [58] this demands 463 experiments. This fact makes it very tedious to utilise the model.

As an alternative approach the kernels can be nonlinearised by introducing stresses or stress rates into the kernels.

This approach was proposed by Pipkin and Rogers [86] and their one dimensional constitutive model may be stated as

$$\varepsilon(t) = \int_0^t \phi_1[t - \tau, \sigma(\tau)] \dot{\sigma}(\tau) d\tau + \int_0^t \int_0^t \phi_2[t - \tau_1, \sigma(\tau_1), t - \tau_2, \sigma(\tau_2)] \dot{\sigma}(\tau_1) \dot{\sigma}(\tau_2) d\tau_1 d\tau_2 
+ \int_0^t \int_0^t \int_0^t \phi_3[t - \tau_1, \sigma(\tau_1), t - \tau_2, \sigma(\tau_2), t - \tau_3, \sigma(\tau_3)] \dot{\sigma}(\tau_1) \dot{\sigma}(\tau_2) \dot{\sigma}(\tau_3) d\tau_1 d\tau_2 d\tau_3$$
(3.3)

The motivation for proposing this model was that the first integral should model single step tests exactly, the second term should extend the exact representation to two step tests etc. An important aspect pointed out by Lockett [58], is that this equation cannot be used as a basis for systematic determination of material properties unless the material happens to be completely definable in one step tests. This stems from the fact that the second term involves a function of four variables and a systematic experimental programme would be prohibitive.

The third model considered is a single integral representation, known as the Rabotnov model. The Rabotnov model is based upon the assumption that the kernels in the expression

$$\varepsilon(t) = \int_0^t J_1(t - \tau_1) d\sigma(\tau_1) + \int_0^t \int_0^t J_2(t - \tau_1, t - \tau_2) d\sigma(\tau_1) d\sigma(\tau_2) + \dots$$
 (3.4)

are separable and expressable as

$$J_i(t - \tau_1, t - \tau_2, \dots, t - \tau_i) = a_i \prod_{n=1}^i J_0(t - \tau_n)$$
(3.5)

where  $a_i$  is a constant and  $J_0$  is the same for all time arguments  $(t-\tau_n)$ . Choosing an appropriate integral operator  $K^*$ , equation (3.4) can be written as

$$\phi(\varepsilon) = \sigma + K^* \sigma \tag{3.6}$$

where  $K^*\sigma$  is given by

$$K^*\sigma = \int_0^t K(t-\tau)\sigma(\tau)d\tau \tag{3.7}$$

which gives the creep strain for an applied stress  $\sigma_0$  as

$$\phi(\varepsilon) = \sigma_0 \left[ 1 + \int_0^t K(t - \tau) d\tau \right]$$
 (3.8)

where  $\phi(\varepsilon)$  incorporates both the instantaneous stress-strain curve and the deviation from the instantaneous curve due to time effects. However, equation (3.8) is of no use if the kernel is

unknown. Rabotnov proposed the following expression for the kernel K(t), [87]

$$K(t) = \frac{e^{-\beta t}}{t} \sum_{n=1}^{\infty} \frac{[A, (\alpha)]^n t^{\alpha n}}{, (\alpha n)}$$
(3.9)

where A,  $\beta$  and  $\alpha$  are constants and , is the Euler function. Having determined these constants the response to an applied load of a material is readily obtainable from equation (3.6).

According to Pyrz [87], a remarkable feature of equation (3.6) is that it describes the creep deformation, the recovery deformation, the relaxation and the stress rate dependence correctly for a variety of isotropic materials and composite materials.

Another single integral model is the endochronic model suggested by Valanis, but since this is a special case of the Schapery model it will not be considered further.

As stated earlier, the constitutive description of the matrix material will be based upon the thermodynamic model, proposed by Schapery. The reason for using the Schapery model is that this model has shown to give very accurate results compared to experiments.

This theory has a number of desirable features, [58]. The ability to describe strong nonlinearity of some materials and the nonlinearity with respect to strain is contained in the form of functions rather than polynomials which are not the most convenient form. The polynomial formulation can lead to wrong conclusions such as predictions of compressive behaviour from tensile data. Furthermore, because of the dependence of material functions of only one variable, the experimental programme is not prohibitive.

The Schapery model appears to describe the deformation behaviour very well, for both stress and strain inputs, [87]. The ability of the model to describe viscoelastic behaviour have been shown by Schapery [101], [102] and Lou and Schapery [60], by applying the model to a variety of materials.

Another advantage, compared to the multiple integral representations, is that it is quite straight forward to use the Schapery model to describe experimental data, whereas the multiple integral representations are virtually impossible to verify in practice.

The Shapery model is based upon the thermodynamics of irreversible processes, and uses the concept of internal state variables. The theory is developed in a series of publications, [99] - [101] and is basically an extension of the work of Biot [7].

# 3.2 The Schapery Model

The state of a material is defined by the generalized state variables  $\xi$ , which are divided into two groups, of observed variables  $\xi_m$   $(m=1,2,\ldots k)$  and hidden variables  $\xi_r$   $(r=k+1,k+2,\ldots n)$ . To each state variable the conjugate forces are denoted by  $\mu_m$  and  $\mu_r$ .

The hidden variables are not important in this particular case, since they vanish in the final equations, but they can be thought of as representing molecular configurations in a polymer or location of interstitial atoms in a metal. In the thermodynamic formulation the generalized state variables need not be restricted, but as will be seen later, six of the observed variables are associated with the six independent components of the strain tensor and the corresponding conjugate forces are associated with the six independent components of the stress tensor.

equations

Constitutive equations must be consistent with the basic principles of continuum mechanics. This implies that the constitutive equation obeys the laws of motion, conservation principles and the Clausius - Duhem inequality, which is a consequence of the second law of thermodynamic. The derivation of the Schapery constitutive equation, for strains expressed in terms of stresses, is based upon a thermodynamic potential, G, known as the Gibbs free energy. For the opposite situation, stresses in terms of strains, the Helmholtz free energy potential is used.

By assuming that the concept of entropy is extendable into situations when the system is in the "neighbourhood" of equilibrium, it is possible, through the Gibbs equation, to equate the internal energy changes for reversible and irreversible processes and obtain an explicit expression for the entropy production. The entropy production is explicitly related to the various irreversible processes in the system through a linear phenomenological relation, (Onsager's principle), between the forces  $(\mu_i - \mu_i^R)$  and the fluxes  $\dot{\xi}_i$  and is expressed as

$$(\mu_i - \mu_i^R) = \sum_{j=1}^n b_{ij}(\mu_m, T) \dot{\xi}_j$$
 (3.10)

This principle states that when the flow  $\dot{\xi}_j$  corresponding to the irreversible process j, is influenced by the force  $(\mu_i - \mu_i^R)$ , corresponding to the irreversible process i, then the flow  $\dot{\xi}_i$  is also influenced by the force  $(\mu_j - \mu_j^R)$  through the same influence coefficients,  $b_{ij}(\mu_m, T)$ . In this description the term  $\mu_i^R$  is the reversible part of the conjugate forces.  $\mu_i^R$  is related to  $\xi_i$  through the Gibb's free energy and thus reduces the problem to the solution of two systems of

$$\xi_m = -\varrho \frac{\partial G(\mu_m, \xi_r)}{\partial \mu_m} \qquad m = 1, 2 \dots k$$

$$\varrho \frac{\partial G(\mu_m, \xi_r)}{\partial \xi_r} + b_{rs}(\mu_m)\dot{\xi_s} = 0 \qquad r, s = k + 1, k + 2 \dots n$$
(3.11)

where  $\varrho$  is mass density. Approximating the Gibbs free energy in a Taylor expansion with respect to the internal variables

$$\varrho G = \varrho G_0(\mu_m) + c_r(\mu_m)\xi_r + \frac{1}{2}d_{rs}(\mu_m)\xi_r\xi_s$$
(3.12)

where  $G_0$  acts as a potential for the time independent response, the second term corresponds to the energy associated with a simultaneous action on the internal variables  $\xi_r$  and the last term is defined by the interaction energy associated with the simultaneous action on the internal variables  $\xi_r$  and  $\xi_s$ , [87]. Substituting the Taylor expansion into equation (3.11) gives the following (n-k) differential equations

$$c_r(\mu_m) + d_{rs}(\mu_m)\xi_s + b_{rs}(\mu_m)\dot{\xi}_s = 0$$
(3.13)

Further simplifications are introduced by the assumption that all coefficients  $b_{rs}(\mu_m)$  and  $d_{rs}(\mu_m)$  are affected equally by the conjugate forces

$$b_{rs}(\mu_m) = a_D(\mu_m)b_{rs}$$
$$d_{rs}(\mu_m) = a_G(\mu_m)d_{rs}$$

where  $b_{rs}$  and  $d_{rs}$  are constant, positive definite matrices.  $a_D$  nonlinearises the entropy production and  $a_G$  nonlinearises the interaction energy in the Gibbs free energy expansion, (3.12). The coefficients  $c_r(\mu_m)$  describes the diffusion of the conjugate forces,  $\mu_m$ , into the material structure where they affect the internal varibles. This nonlinear force transfer process introduces a third nonlinearising function  $\bar{\mu}_m$ , and can be described by

$$c_r(\mu_m) = f_{rm}\bar{\mu}_m(\mu_m)$$

where  $f_{rm}$  is a constant matrix.

By the simplifications and assumptions above it is now possible to reduce the n-k differential equations in (3.13) and obtain a set of differential equations with constant coefficients

$$a_G(\mu_m)d_{rs}\xi_s + a_D(\mu_m)b_{rs}\frac{d\xi_s}{dt} = -f_{rm}\bar{\mu}_m(\mu_m)$$
  $r, s = k+1, k+2, \dots n$  (3.14)

This set of equations can be rewritten by introducing the reduced time,  $\psi$ , as

$$d_{rs}\xi_s + b_{rs}\frac{d\xi_s}{d\psi} = -\frac{1}{a_G}f_{rm}\bar{\mu}_m(\mu_m)$$
(3.15)

where  $d\psi = (a_G/a_D)dt$ . Upon substitution of the free energy expansion, equation (3.12), into the first of equations (3.11) the k algebraic equations are obtained as

$$\xi_m = -\varrho \frac{\partial G_0(\mu_m)}{\partial \mu_m} - f_{rm} \frac{\bar{\mu}_m(\mu_m)}{\partial \mu_m} \xi_r \tag{3.16}$$

where the third term in the free energy expansion is neglected. The set of decoupled differential equations, (3.14), can be integrated for the internal variables  $\xi_s$  and substituted into the equation above, thus giving the set of observable variables  $\xi_m$  in integral form.

For uniaxial loading only one observed variable  $\xi_1$  exists and is equal to  $\varepsilon$ . The virtual work condition  $\delta W = \mu_i \delta \xi_i = \sigma \delta \varepsilon$  gives the generalised force  $\mu_1 = \sigma$ , leading to the one dimensional Schapery equation

$$\varepsilon(t) = -\varrho \frac{\partial G_0}{\partial \sigma} + \frac{\partial \bar{\mu}_1(\mu_1)}{\partial \mu_1} \int_0^t D(\psi - \psi') \frac{\partial (\bar{\mu}_1/a_G)}{\partial \tau} d\tau$$
 (3.17)

or in the well known form

$$\varepsilon(t) = g_0 D_0 \sigma + g_1 \int_0^t \Delta D(\psi - \psi') \frac{\partial g_2(\sigma(\tau))}{\partial \tau} d\tau$$
(3.18)

where

$$g_0 = -\varrho \frac{\partial G_0}{\partial \sigma} \frac{1}{D_0 \sigma}$$
$$g_1 = \frac{\partial \bar{\mu}_1}{\partial \mu_1}$$

$$g_2 = \frac{\bar{\mu}_1}{a_G} \frac{1}{\sigma}$$

$$D_0 = D(0)$$

$$\psi \equiv \int_0^t \frac{dt}{a_\sigma}$$

$$\psi' \equiv \psi(\tau) \equiv \int_0^\tau \frac{dt}{a_\sigma}$$

$$a_\sigma = \frac{a_D}{a_G}$$

## 3.2.1 Creep

In this section the parameters in the Schapery model are determined from creep data provided by BASF. The creep data corresponds to several load levels at temperatures  $T = 23^{\circ}C$ ,  $60^{\circ}C$ ,  $80^{\circ}C$ ,  $100^{\circ}C$  and  $120^{\circ}C$ . Only the data for  $23^{\circ}C$  and  $60^{\circ}C$  are considered since these are the temperatures at which experiments were carried out. The loads provided by BASF are  $\sigma_0 = 1, 2, ..., 8$  MPa for  $T = 23^{\circ}C$  and  $\sigma_0 = 1, 2, ..., 4$  MPa for  $T = 60^{\circ}C$ .

Application of a nominal stress  $\sigma = \sigma_0 H(\tau)$  at time  $\tau = 0$ , reduces equation (3.18) to:

$$\varepsilon(t) = \sigma_0 \left( D_0 g_0 + g_1 g_2 \Delta D \left( \frac{t}{a_\sigma} \right) \right) \tag{3.19}$$

where  $H(\tau)$  is the Heaviside step function.

Assuming that the nonlinear transient creep compliance can be expressed as

$$\Delta D(\psi) = D_1 \psi^n$$

a power law creep equation is obtained

$$\varepsilon(t) = \sigma_0 \left( D_0 g_0 + g_1 g_2 D_1 \left( \frac{t}{a_\sigma} \right)^n \right) \tag{3.20}$$

To determine  $D_0$  and  $D_1$  the creep data in the linear viscoelastic range is used. This corresponds to applied loads of 1,2 and 3 MPa. In the linear viscoelastic region  $g_0 = g_1 = g_2 = a_{\sigma} = 1$  and thus the following equation holds

$$\varepsilon(t) = \sigma_0 \left( D_0 + D_1 t^n \right) \tag{3.21}$$

The parameters  $D_0$  and  $D_1$  are determined by a least squares data regression and the exponent is obtained as the slope of the data plotted in a double logarithmic co-ordinate system. The three parameters  $g_1$ ,  $g_2$  and  $a_{\sigma}$  are determined by rewriting equation (3.20) and assuming that  $g_0 = 1$ 

$$\log\left\{\frac{\varepsilon(t)}{\sigma_0} - g_0 D_0\right\} \frac{1}{D_1} = \log\left\{g_1 g_2 \left(\frac{t}{a_\sigma}\right)^n\right\}$$
(3.22)

and using a least squares data regression gives  $\frac{g_1g_2}{a_z^n}$ .

The assumption that  $g_0 = 1$  is supported by Brueller [11], who has investigated the nonlinear long term behavior of the polymeric materials; poly-methylmethacrylate (PMMA), poly-styrene (PS), poly-oxymethylene (POM) and styrene-acrylonitriles (SAN).

The most important consequence of the fact that  $g_0 = 1$  is that the instantaneous response to an applied load - of the polymeric material is always linear, even in the nonlinear range, i.e. yielding is not accounted for.

Due to the lack of recovery data it is not possible to distinguish between the three nonlinearizing parameters  $g_1$ ,  $g_2$  and  $a_{\sigma}$ . Due to this fact, it is assumed that the product  $g_1g_2$  is equal to unity and thereby placing all the nonlinearity on  $a_{\sigma}$ . This assumption is indirectly validated by the physical nature of the parameters. The parameters  $g_0$ ,  $g_1$  and  $g_2$  reflect third and higher order stress dependence of the Gibb's free energy, whereas  $a_{\sigma}$  reflects stress dependence on both the entropy production and free energy. Since the entropy production (Second law of thermodynamics) restricts the nature of constitutive models it would be inconsistent to assume that  $a_{\sigma}$  equals unity and instead place the nonlinearity on some of the other parameters.

The assumption that  $g_1g_2$  equals unity is also indirectly supported by experiments by Hiel [39], Xinran [131] and Lou and Schapery [60]. They found that  $g_1$  is a slightly decreasing function of stress, whereas  $g_2$  is a slightly increasing function of stress, and thus the product equals unity to a good approximation.

It should be noted here that the case of  $g_0 = g_1 = g_2 = 1$  and letting all nonlinearity be due to  $a_{\sigma}$  is analogous to what Valanis proposed in his rate independent "plasticity" theory. However, that theory was based upon ideas provided by Schapery in 1969.

The expressions for  $a_{\sigma}$  as a function of stress at temperatures 23°C and 60°C are found to be

$$a_{\sigma}(\sigma, 23) = 10^{(-0.14\sigma + 0.41)}$$
  
 $a_{\sigma}(\sigma, 60) = 10^{(-0.36\log(\sigma) - 0.83)}$  (3.23)

where  $\sigma$  is normalised with respect to the stress at which the material is in its linear range, i.e.  $\sigma = \sigma_{app}/1$  MPa.

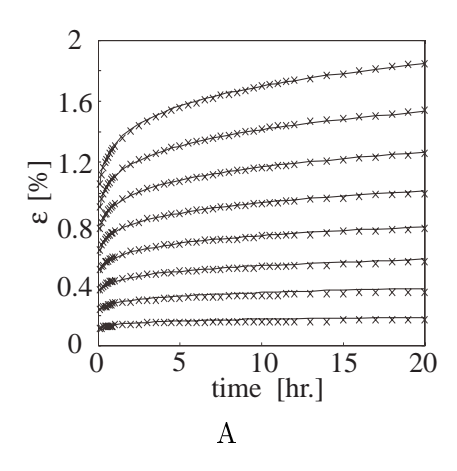
The creep data and the strains calculated by equation (3.20) are shown in figure 3.1. For T=23 °C the loads are 1,...,8 MPa and for T=60 °C the loads are 1,...,4 MPa.

In summary the creep constitutive equation is found to be

$$\varepsilon(t) = \sigma_0 \left\{ g_0 D_0 + g_1 g_2 D_1 \left( \frac{t}{a_\sigma} \right)^n \right\}$$
 (3.24)

where n is found to be 0.17 and  $D_1$  is  $733 \times 10^{-6}$  MPa<sup>-1</sup>.  $D_0$  is equivalent to 1/E and is a function of temperature as shown in the table below.

T [°C]	$D_0 \times 10^{-6} [\text{MPa}^{-1}]$
23	667
60	3480



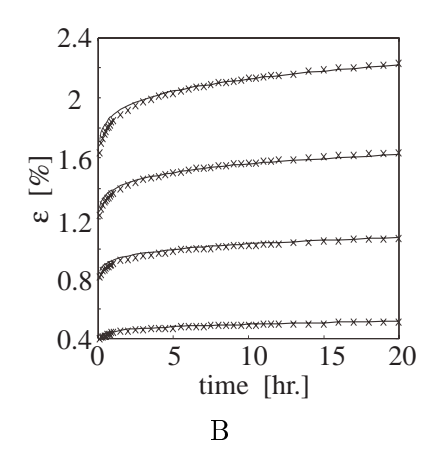


Figure 3.1: The creep data and the predicted strains for polypropylene at A) T=23 °C and B) T=60 °C.

As seen in the figure the experimental creep data and the predicted creep curves show very good agreement.

## 3.2.2 Recovery

After removal of the applied load an elastic contraction of the material is followed by a time dependent contraction. This contraction is known as recovery. The strains will asymptotically approach zero as time approaches infinity - provided that no yielding has occurred. The recovery strains are modelled by using equation (3.18). Applying a stress  $\sigma_a$  at time  $t = t_a$  and a stress  $\sigma_b$  at time  $t = t_b$ , carrying out the integration and equating  $\sigma_b$  to zero yields the recovery strain as [102]

$$\varepsilon_r(t) = g_2 D_1 \sigma \left(\frac{t_a}{a_\sigma}\right)^n \left[ (1 + a_\sigma \lambda)^n - (a_\sigma \lambda)^n \right]$$
(3.25)

where  $\lambda$  is equal to  $(t-t_a)/t_a$  and  $t_a$  corresponds to the time at which the load,  $\sigma$ , is removed.

#### 3.2.3 Relaxation

Relaxation is modelled using the expression by Schapery [102]

$$\sigma(t) = \varepsilon_0 \left\{ h_e E_e + h_1 h_2 \Delta E\left(\frac{t}{a_{\varepsilon}}\right) \right\}$$
 (3.26)

where a power law is assumed for the nonlinear relaxation modulus,  $\Delta E$ , which leads to

$$\sigma(t) = \varepsilon_0 \left\{ h_e E_e + h_1 h_2 E_1 \left( \frac{t}{a_{\varepsilon}} \right)^m \right\}$$
 (3.27)

The relaxation data are for strain levels of  $\varepsilon_0 = 0.04$ , 0.08, 0.2, 0.3, 0.4, 0.6, 0.8 and 1 % at temperature T = 23°C and  $\varepsilon_0 = 0.08$ , 0.2, 0.3, 0.4, 0.6, 0.8 and 1 % at T = 60°C. The values of the various parameters are found by applying a non-linear least squares data regression to the experimental data. It was found that the best fit between experimental data and theory was

obtained when  $a_{\varepsilon} = 1$ . The non-linear parameters  $h_e$  and  $h_1h_2$  are shown in equation (3.28) and  $E_e$  and  $E_1$  are shown in the table below.

$$h_{e}(\varepsilon, 23) = 10^{(-0.27 \log(\varepsilon) - 3.34)}$$

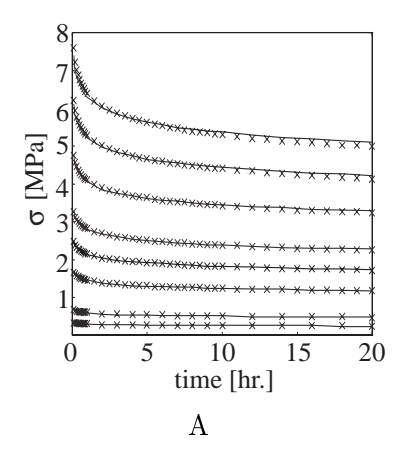
$$h_{1}h_{2}(\varepsilon, 23) = -2.36\varepsilon + 0.15$$

$$h_{e}(\varepsilon, 60) = 10^{(-0.37 \log(\varepsilon) - 2.62)}$$

$$h_{1}h_{2}(\varepsilon, 60) = -0.6\varepsilon + 0.14$$
(3.28)

T [°C]	$E_e$ [MPa]	$E_1$ [MPa]	m
23	1500	5050	-0.07
60	661	1600	-0.048

The experimental data together with equation (3.27), for the two temperatures, are shown in figure 3.2 and very good agreement is observed.



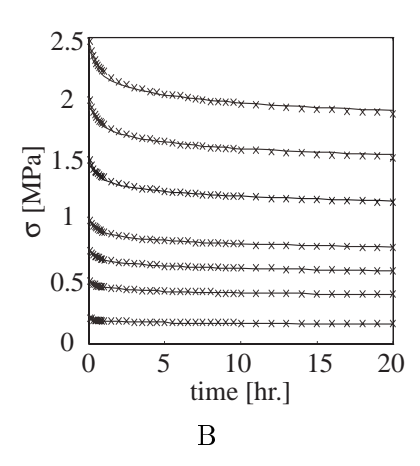
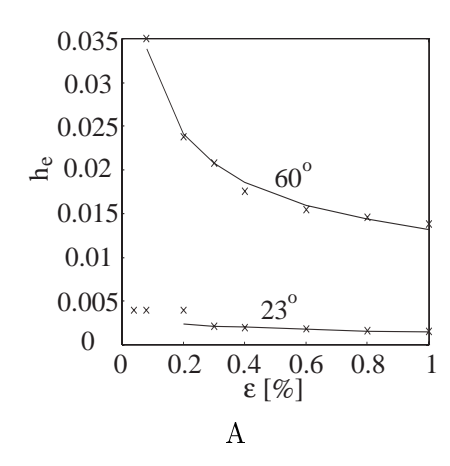


Figure 3.2: The experimental data along with the relaxation function, for temperatures A)  $23^{\circ}C$  and B)  $60^{\circ}C$ .

The non-linearising parameters  $h_e$  and  $h_1h_2$  are shown in figure 3.3.

It is seen from the graph of  $h_e(\varepsilon, 23^{\circ}C)$  that the instantaneous response of the material is first independent of strain. However, when the strain is larger than 0.2 %, the instantaneous response of the material is nonlinear. The strain at which the material response changes from independent of strain to a nonlinear function of strain corresponds to an applied load of 3 MPa, which is also the level at which the creep strain changes from linear to nonlinear. The graph of  $h_e(\varepsilon, 60^{\circ}C)$  shows that at this temperature the material is highly nonlinear.

The product of the parameters  $h_1h_2$  is continuously decreasing with strain, for both temperatures, indicating that the time dependent response of the material is softening with increasing strain but at different rates.



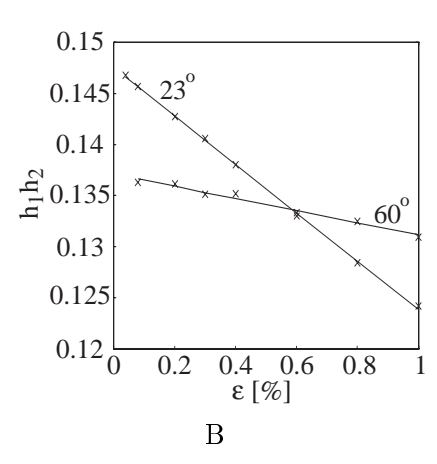


Figure 3.3: The figures show A) the non-linearising parameters  $h_e$  and B) the non-linearising parameter  $h_1h_2$  for the temperatures 23° C and 60° C.

## 3.3 3 - D Constitutive Model

From the uniaxial Schapery model it is possible to formulate a three dimensional constitutive model.

Using the generalised Hooke's law in terms of stress

$$\varepsilon_{ij} = \frac{1+\nu}{E}\sigma_{ij} - \frac{\nu}{E}\delta_{ij}\sigma_{kk} \tag{3.29}$$

defining  $\tilde{D}(t)$  as

$$\tilde{D}(t) \equiv \left(D_0 g_0 + g_1 g_2 D_1 \left(\frac{t}{a_\sigma}\right)^n\right) \tag{3.30}$$

and rewriting  $a_{\sigma}$  in terms of Von Mises effective stress,  $\sigma_e$ , given by  $\sqrt{(3/2)s_{ij}s_{ij}}$  where  $s_{ij}$  is the deviatoric stress tensor.

Substitution of the nonlinear creep compliance into Hooke's law and assuming that Poisson's ratio is independent of time or at least a weak function of time, the creep strains are obtained as

$$\varepsilon_{ij}(t) = \tilde{D}(t)(1 + \nu_m)\sigma_{ij} - \tilde{D}(t)\nu_m\delta_{ij}\sigma_{kk}$$
(3.31)

This equation is valid for any isotropic, time dependent material subjected to a constant applied load, [98].

The same approach is used when considering the stress variation with time. Defining  $\tilde{E}(t)$  as

$$\tilde{E}(t) \equiv (h_e E_e + h_1 h_2 E_1 (t)^m)$$
(3.32)

and rewriting  $h_e$  and  $h_1h_2$  in terms of the effective strain,  $\varepsilon_e$ , given by  $\varepsilon_e = \sqrt{(3/2)e_{ij}e_{ij}}$  and  $e_{ij}$  is the deviatoric strain tensor. The time dependent stress becomes

$$\sigma_{ij}(t) = \frac{\tilde{E}(t)}{1 + \nu_m} \left( \varepsilon_{ij} + \frac{\nu_m}{1 - 2\nu_m} \delta_{ij} \varepsilon_{kk} \right)$$
(3.33)

3.4. Summary

## 3.4 Summary

In this chapter it has been shown that the non-linear Schapery constitutive model predicts the creep strain and relaxation strain for polypropylene very well. To predict the creep strains a power law containing only one non-linearising parameter is necessary, namely  $a_{\sigma}$  which is found to be a continuously decreasing function of stress, whereas the relaxation stresses are found by using a power law expression containing two non-linearising parameters  $h_e$  and  $h_1h_2$  which are decreasing functions of strain. A three dimensional constitutive model has been proposed based on the combination of the one dimensional Schapery equation and Hooke's law of elasticity and the assumption that Poisson's ratio is independent of time or at least a weak function of time.

4

# **Experimental Results**

E and recovery is the scope of the present chapter. Various loading histories are applied to both the PP-U composites and the PP-MA composites. Results from the experiments are shown and discussed.

The improvement in mechanical performance of short fibre reinforced thermoplastics is greatly dependent on the constitution of the fibre-matrix interface. For a satisfactory transfer of stresses between the polymer matrix and the fibre reinforcement it is necessary that efficient load transfer mechanisms exist along the fibre-matrix interface.

Several investigations, using MRS, considered different factors affecting the interface bond quality, such as fibre sizing, Paipetis and Galiotis [79], axial modulus of fibres, Melanitis and Galiotis [65] and curing temperature, Huang and Young [43].

The load transfer efficiency is usually determined from conventional fragmentation tests performed with monotonicly increased load. However, the mechanical behaviour of short fibre composites is dominated by the complex stress distribution due to fibre discontinuities as well as residual stresses generated in the fibre after the manufacturing process. The presence of embedded fibres constrains the matrix deformation that can not develop freely under external loading and creates a disturbance in the stress/strain field. During creep loading conditions in particular, the interaction between residual stresses and relaxation behaviour of the matrix in the vicinity of the fibre may affect the load transfer efficiency depending upon the degree of adhesion between the fibre and matrix material. Thus the loading history by itself may have an influence on the load transfer quality.

Due to local relaxation effects in viscoelastic composite materials a variety of loading situations have been applied to the specimens in order to determine the loading history's influence upon the fibre strain. The loading histories are: Creep loading, mechanical conditioning/subsequent creep, creep/subsequent recovery, creep loading at an elevated temperature, creep loading on specimens with misaligned fibres and finally creep loading of specimens with interacting fibres.

## 4.1 Specimen Preparation and Materials Data

The specimens were prepared by placing a fibre between a polypropylene sheet and a polypropylene film, as shown in figure 4.1. Different specimens were prepared. Some specimens contained

fibres aligned parallel, (deviation from parallel was less than  $\pm$  5°), to the longitudinal axis of the specimen and some with misaligned fibres.

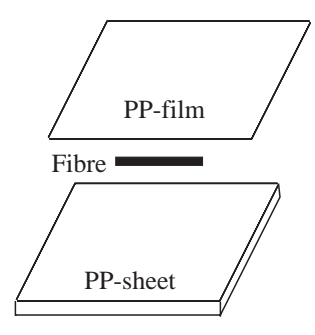


Figure 4.1: Specimen preparation.

This assembly was placed in an aluminium mould and placed in an oven at a temperature adjusted to ensure that the polypropylene film and sheet melted and joined completely. After removing the mould from the oven it was cooled in water, still containing the specimen. Since transcrystallinity around the fibre and nucleation of spherulites in the matrix may cause premature fibre breaks, the mould was subjected to a high cooling rate to prevent this nucleation. However, fibre breaks did occur during quenching, but these were primarily due to the different thermal properties of the fibre and matrix and not due to nucleation phenomena occurring in the matrix. After cooling the specimens were cut to a dog bone shape. The material properties for the matrix and fibre are shown in the table below and the specimen geometry is shown in figure 4.2.

Fibre	HM Carbon	Matrix	Polypropylene
$E_f^l$	350  GPa	$E_m$	1.5 GPa $(T = 23^{\circ})$
$E_f^t$	22 GPa	-	-
$ u_f^l $	0.006	$\nu_m$	0.35
$ u_f^t $	0.35	-	-
$\alpha_f^t$	$25 \times 10^{-6}  {}^{\circ}\mathrm{C}^{-1}$	$\alpha_m$	$1.35 \times 10^{-4}  {}^{\circ}\mathrm{C}^{-1}$
$\alpha_f^l$	$-1.3 \times 10^{-6}  {}^{\circ}\mathrm{C}^{-1}$	-	-

The fibre properties are quoted values from the manufacturer except for  $E_f^t$  which is taken from [23].

thickness: 3 - 4 mm

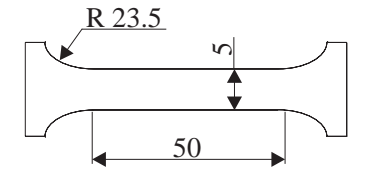


Figure 4.2: Specimen geometry.

The fibre diameter was measured on 24 plasma treated fibres, using SEM, and the mean fibre

diameter was found to be 6.1  $\mu$ m. The SEM was calibrated for the fibre diameter measurements using an optical scale.

Due to the nature of polypropylene, difficulties in obtaining strong interfacial bonding may be encountered. However, there are ways to improve the interfacial bonding, either by modification of the fibre surface or the polymer. In the first experimental series, plasma treated fibres were used in conjunction with unmodified polypropylene. The model composites consisting of this material combination are subsequently denoted as "PP-U" composites. The plasma treatment was carried out by NKT Research Center, Denmark. The specific conditions of the plasma treatment are known to the author, but will not be described here due to NKT's application for a patent on this specific treatment.

In all the subsequent figures showing experimentally measured fibre strains, the fibre end is situated at the origin of the coordinate system and  $L_f$  on the horisontal axes denotes distance along the fibre.

## 4.2 Experimental Results for PP-U Specimens

Plasma treatment of the fibres may enhance interfacial strength by modifying the nature and amount of functional surface groups. Bogoeva-Gaceva et al. [8] investigated the effect of different plasma treated fibres on interfacial strength. Comparisons between fibres with standard surface treatment and plasma treated fibres showed an increase in interfacial strength from 53 MPa to 61 MPa. Additionally, the plasma treatment was also shown to increase the surface roughness of the fibres and this was especially true for the fibres which were plasma treated in air. This indicates that the increase in interfacial strength may be due to a larger degree of mechanical interlocking, which was found by Schadler et al. [97]. Another important aspect was pointed out by Drzal et al. [21] who found that the plasma treatment was enhancing interfacial adhesion primarily by removing a weak surface layer - originating from the manufacture of the fibre - and thereby preventing cohesive failure in the fibre.

#### Initial Residual Strain

The first experimental series consisted of measurements of the initial residual strain - generated during manufacture - in the PP-U composites. The initial residual strains are due to manufacture of the specimen. This information is easily obtainable and is believed to give valuable insight to the nature of the load transfer mechanism. Several measurements on different specimens have been conducted; a part of them are shown in figure 4.3.

As seen from the figure the initial residual fibre strains in the specimens after manufacture display a linear behaviour with respect the longitudinal fibre axis. The solid line indicates the mean residual strain of the measurements and is given as

$$\varepsilon_f(x) = -0.35x - 0.1456 \tag{4.1}$$

This linear behaviour is not expected if the fibres are perfectly bonded to the matrix material. In the perfect bonded situation the fibre strains will be nonlinear with respect to the fibre axial coordinate. The linear behaviour indicates that the nature of the load transfer mechanism for this material combination may display some interesting features.

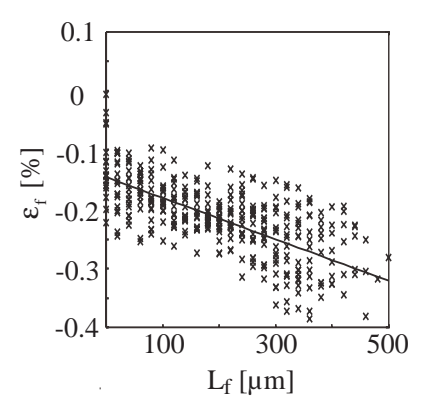


Figure 4.3: Initial residual strains for half the fibre lengths.

In conjunction with the measurements of the initial residual fibre strains the fibre lengths were measured. The fibre lengths were measured in the Raman microscope through an optical scale to an accuracy of 5  $\mu$ m. The mean length was found to be 740  $\mu$ m and no fibre breaks were observed, even for fibres with lengths larger than 1 mm.

In the following figures showing the fibre strains, all the specimens contain fibres aligned parallel to the loading axis, unless stated otherwise.

#### Initial Elastic Strain

The next set of experiments conducted were measurements of the initial elastic fibre strains in PP-U composites subjected to loads of 3, 5 and 7 MPa. The fibre strains for half the fibre length at the three load levels are shown in figure 4.4.

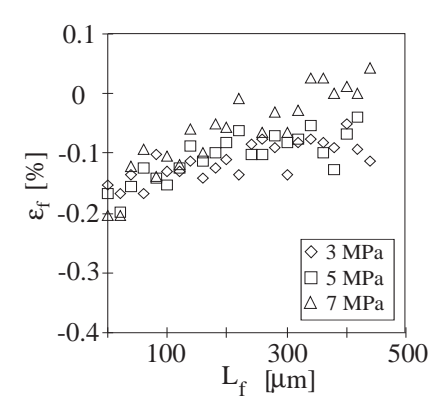


Figure 4.4: Initial elastic fibre strains at loads of 3, 5 and 7 MPa.

This figure displays some very indicative features. First, the maximum strain in the middle of the fibre at a load of 7 MPa is close to zero. Secondly, the shape of the strain profiles are very close to linear. Finally, only small differences between strain magnitude in the three cases are observed, even though they should be quite different, due to the difference in overall applied strain which is 0.2 %, 0.33 % and 0.47 %, respectively.

Considering the three load cases separately, the main reason for the strain to be close to zero at a load of 7 MPa might be large initial residual strains in the specimen due to manufacture.

However, considering the other two features, the shape of the strain profile and the small differences between the strain magnitude in the three situations, it is clear that residual strains alone can not be responsible for the observed strain profiles since large residual strains will affect the fibre strains equally in the elastic situation. An aspect thus needed to be considered is the load transfer at the interface which does not seem to reflect a perfect bonding, but rather seem to be of a friction-like or mechanical character as suggested by Di Landro and Pegoraro [53] and Jang [48]. Galiotis [29] also observed friction-like load transfer mechanisms in his study of load transfer in continuous and discontinuous model composites.

## 4.2.1 Mechanical Conditioning and Subsequent Creep

The next series of experiments conducted were mechanical conditioning and subsequent creep loading for 3 hours on PP-U composites. Results from this investigation can also be found in Schjødt-Thomsen and Pyrz [103]. The mechanical conditioning is 5 consecutive cycles of loading and unloading. The applied load level corresponds to the applied load for the subsequent creep. The purpose of the mechanical conditioning is to monitor its effect on the interfacial quality and subsequent creep.

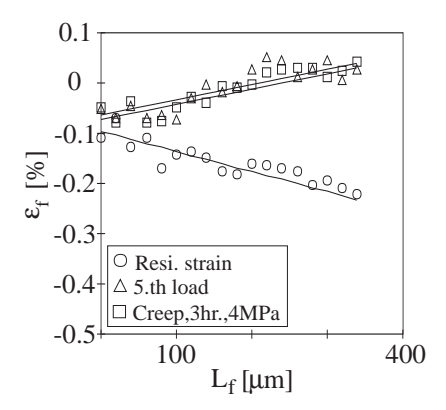


Figure 4.5: The initial residual strain, the strain after the fifth load application and the creep strain after 3 hours at 4 MPa.

Figure 4.5 presents the fibre strain measured at the fifth cycle and the corresponding 3 hour creep for a load of 4 MPa. The fibre strain is shown for half the fibre length.

The fibre strains after mechanical conditioning are principally the same as the strains induced in the subsequent creep loading. This observation strongly suggests, that the load transfer mechanism has frictional character since viscoelastic effects present in the matrix material do not alter the fibre strains during creep loading conditions. These observations indicate that the interface is damage intolerant, i.e. very few load cycles will reduce the load transfer efficiency.

Conducting a linear data regression and using the one dimensional balance of forces principle the interfacial shear stress can be obtained as

$$\tau_i(x) = \frac{d_f E_f^l}{4} \frac{d\varepsilon_f}{dx} \tag{4.2}$$

The interfacial shear stresses from the experiment shown in figure 4.5 are  $\tau_{resi.} = -2.1$  MPa,  $\tau_5 = 1.6$  MPa and  $\tau_{creep} = 1.6$  MPa, respectively.  $\tau_5$  denotes the interfacial shear stress at the fifth

load application. The decrease in interfacial shear stress upon loading is attributed to the damage intolerance of the interface.

The initial residual strain of figure 4.5 displays "localised" curvature, which is believed to be due to stick-slip effects between the fibre and matrix. The stick-slip effect is due to interaction between radial stresses and shear stresses as

$$\sigma_r < 0 \implies \tau_i < \mu_{fric}, \sigma_r \quad stick - condition$$
  
 $\sigma_r < 0 \implies \tau_i = \mu_{fric}, \sigma_r \quad slip - condition$ 

From the figure it is seen that the load is building up over a short length until the interface cannot sustain the actual load level and then decreases again and so on until it reaches a maximum at the middle of the fibre.

## 4.2.2 Creep and Subsequent Recovery

If the load is transferred from the matrix to the fibre by friction via a weak interface, the effect of the weak interface will also be reflected in the recovery strain behaviour, i.e. the recovery strain will not reach the same magnitude as the initial residual strain.

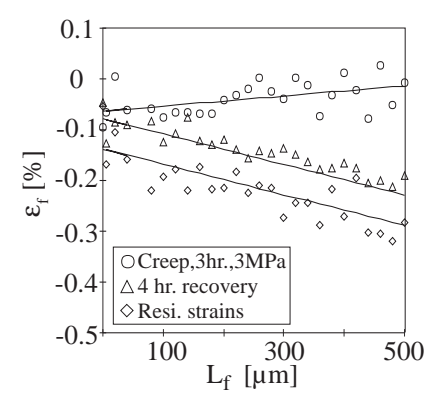


Figure 4.6: The initial residual strain along with the 3 hour creep strain and the recovery strain after 4 hours recovery at a load of 3 MPa.

Figure 4.6 shows the initial residual strain along with the creep strain after application of a load of 3 MPa and the strain after 4 hours recovery, for half the fibre length. Using a linear data regression and equation (4.2) the interfacial shear stresses are found to be  $\tau_{resi.} = -1.6$  MPa,  $\tau_{creep} = 0.53$  MPa and  $\tau_{recovery} = -1.6$  MPa. As expected the recovery strain is increased quite drastically compared to the initial residual strain. The magnitude of the recovery strain is only about half the magnitude of the initial residual strain. However, the interfacial shear stresses are the same in the two cases. This implies - as can also be seen from the figure - that the compressive load at the end of the fibre contributes significantly to the total amount of load carried by the fibre.

Figure 4.7 shows the initial residual strain along with the creep strain after application of a load

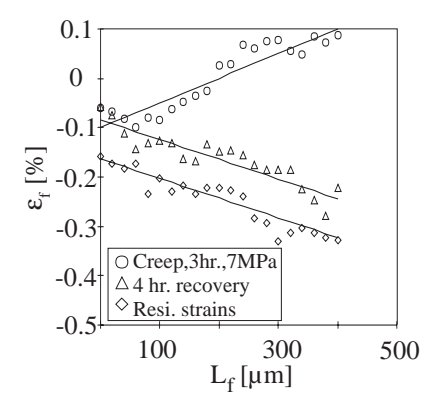


Figure 4.7: The initial residual strains along with the 3 hour creep strains and the recovery strains after 4 hours recovery at a load of 7 MPa.

of 7 MPa and the strain after 4 hours recovery, for half the fibre length. The same tendencies as in the previous figure appear. The recovery strain is increased compared to the initial residual strain. The overall matrix recovery strains, after loading at 3 and 7 MPa are 0.03 % and 0.17 %, respectively. Even this large difference in overall strain does not have any significant effect on the recovery strains. Again the initial residual strain is displaying the stick-slip effect. A linear data regression has been applied to the data and the interfacial shear stresses were found to be  $\tau_{resi.} = -2.1$  MPa,  $\tau_{creep} = 2.7$  MPa and  $\tau_{recovery} = -2.1$  MPa.

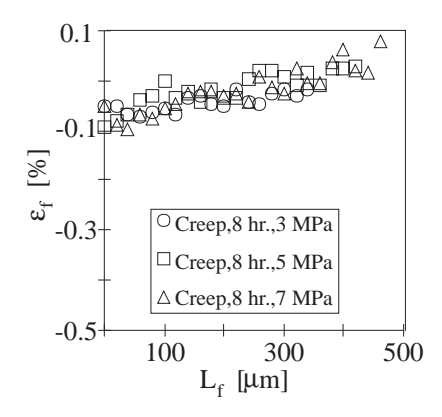


Figure 4.8: Fibre creep strains after 8 hours loading.

In order to check the strong indications of the existence of a frictional load transfer mechanism, 8 hour creep experiments were conducted at loads of 3, 5 and 7 MPa.

The fibre creep strains from this investigation are shown in figure 4.8, for half the fibre length. It is clear from the figure that the magnitude of the fibre creep strains show no significant differences in spite of the fact that the overall creep strains at these three load levels are 0.51 %, 0.91 % and 1.38 %, respectively. Comparison of figures 4.8 and 4.4 discloses that the viscoelastic effects does not have a pronounced effect on the magnitude of the fibre strains at these loading times. Furthermore, the result indicate that the magnitude of the load transfer between the matrix and fibre has reached a saturation level governed by the initial residual stresses and the coefficient of friction.

## 4.2.3 24 hour Creep

Based on the previous investigations it was concluded that the load transfer mechanism is of a frictional character and the next experiment set forth will give insight to how the model composite performs for longer loading times.

A load of 3 MPa was applied to the PP-U composites for 24 hours and a typical strain profile is shown in figure 4.9.

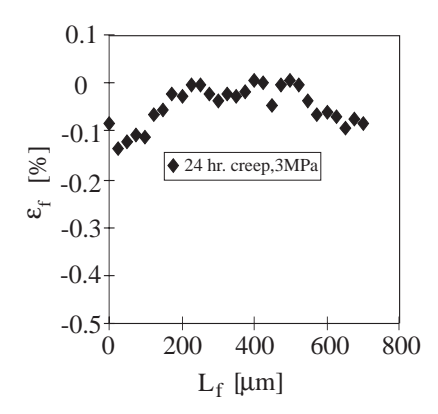


Figure 4.9: Fibre creep strains after 24 hours at a load of 3 MPa.

It is seen in the figure that the strain in the middle of the fibre is nearly constant, but very close to zero. This indicates that the viscoelastic nature of the matrix and the poor (or non-existent) adhesion between the fibre and matrix will reduce the radial stress at the interface. Since the load transfer is a result of friction, the radial pressure at the interface is governing the performance of the composite, and if the radial pressure decreases, due to relaxation, the fibres will carry less load and the composite will not perform as intended, but will probably perform worse than the pure matrix.

Finally, at a load of 7 MPa and loading times larger than 8 hours fibre pull-out was observed as shown in figure 4.10.

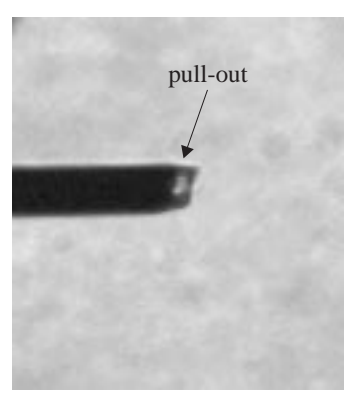


Figure 4.10: Observed pull-out at the fibre end.

It has been shown that the load transfer mechanism in the PP-U model composites is of a frictionlike character. This conclusion is based on the linearity of the fibre strain with respect to the fibre axis and the general behaviour displayed after application of different loading histories. Generally, the PP-U composites have displayed poor creep properties. However, in a real composite the frictional load transfer mechanism together with pull-out is a very energy consuming combination which is desired in e.g. impact situations where brittle fracture may then be avoided. Additional investigations may be necessary before a final conclusion can be reached, regarding real composite behaviour, because the interaction between fibres in a high volume fraction composite may affect the load transfer efficiency.

## 4.3 Experimental Results for PP-MA Specimens

An alternative to the plasma treatment of the fibres in order to improve interfacial adhesion is modification of the polymer itself. The apolar nature of polypropylene can be changed by grafting it with maleic-anhydride. Maleic-anhydride has proven to be very efficient at improving the load transfer efficiency in glass fibre reinforced polypropylene. Since polypropylene is an apolar polymer and has limited affinity to fibre sizings, maleic-anhydride grafted onto the polymer results in a more efficient interaction with fibre sizings. The bonds can be the result of chemical reactions, Xanthos [130], or physisorption with interdiffusion of the polymer chains into the sizing and local dipole-dipole bonding. Hydrogen bondings are also likely to be present, Lin [56] and De Roover et al. [94]. Gamstedt [32], considered fatigue and damage behaviour of glass fibre reinforced polypropylene and found a ten fold increase in fatigue life of the grafted polymer compared to the ungrafted polymer.

Model composites consisting of fibres with a standard surface treatment and polypropylene grafted with maleic-anhydride are subsequently denoted as "PP-MA" composites.

The fibre diameter was measured on 24 fibres using SEM and the mean fibre diameter was found to be 6.7  $\mu$ m for the fibres with the standard surface treatment.

#### Initial Residual Strain

As in the previous experimental series the residual fibre strains were measured in the PP-MA composites. In figure 4.11 the initial residual fibre strains are shown for a number of fibres, for half the fibre length, along with a solid line indicating a polynomial fit of the mean residual strain.

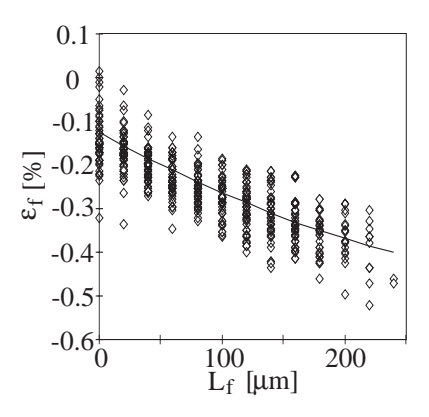


Figure 4.11: Initial residual fibre strains in the PP-MA composites.

As seen from the figure the initial residual strains in the PP-MA composites are significantly larger than the initial residual strains in the PP-U composites. Furthermore, all the fibre strain profiles display non-linearity with respect to the fibre axial coordinate. This is shown in a typical plot of the initial residual strain for half a fibre length in figure 4.12.

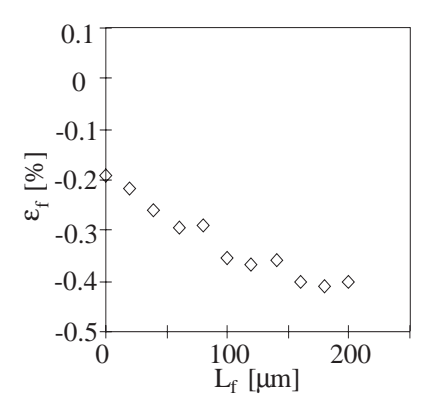


Figure 4.12: The initial residual fibre strain in a typical PP-MA composite.

As for the PP-U composites the fibre lengths in the PP-MA composites were measured and the mean fibre fragment length was found to be 450  $\mu$ m. The average fibre strain in the middle of a fibre of length 450  $\mu$ m is found from the data in figure 4.11 to be -0.39 %, which is close to what was found by Melanitis and Galiotis [64]. They used a bending rig for conducting compressive fragmentation of high modulus carbon fibres and found a strain to break of -0.45 %  $\pm$  0.05. Calculating the average fibre strain - for the PP-U composites - in the middle of a fibre of length 740  $\mu$ m the value of the average fibre strain is -0.27 %. A direct comparison between the PP-MA average strain and the PP-U average strain shows that the maleic-anhydride increases the initial residual fibre strain by a factor of approximately 1.5. This effect becomes more obvious when considering the strain carried per millimeter along the fibre length, as shown in figure 4.13.

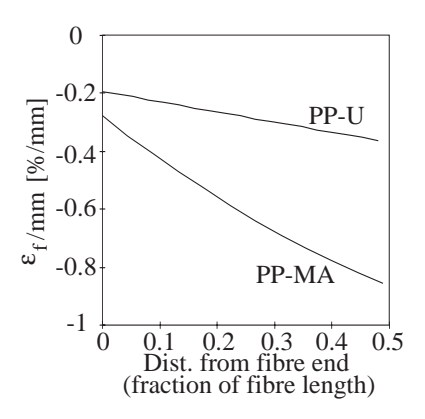


Figure 4.13: Strain per mm in the PP-U and the PP-MA specimens.

In figure 4.13 the distance from the fibre end is normalised with respect to the mean fibre fragment length, i.e. the data from the PP-U composites are shown for a fibre length corresponding to 740  $\mu$ m, whereas the PP-MA data are for a fibre length of 450  $\mu$ m. Even though the PP-U data are calculated for a fibre length nearly twice as large as for the PP-MA data the load transfer efficiency is very poor when considering the PP-U data. Considering the magnitude of load

transferred per millimeter it is seen that the PP-MA composites are about 3 times as efficient as the PP-U composites.

## 4.3.1 Creep

The following series of experiments consider the 3 hour creep of the PP-MA composites at different load levels.

From the experimentally measured fibre strain, the interfacial shear stresses were obtained through applying a nonlinear least squares data regression routine to the experimental data and subsequently using equation 4.2. The functions used in this procedure are the Gaussian function and the Lorentzian function given by

$$f_{Gauss}(x) = Ae^{\left(-\frac{(x-x_0)^2}{2w^2}\right)} + B$$

$$f_{Lorentz}(x) = \frac{A}{\frac{(x-x_0)^2}{w^2} + 1} + B$$
(4.3)

where A,  $x_0$ , w and B are shown schematically in figure 4.14.

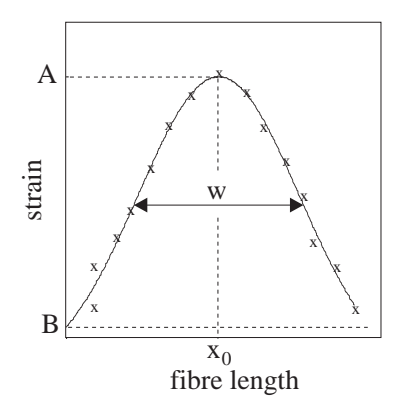
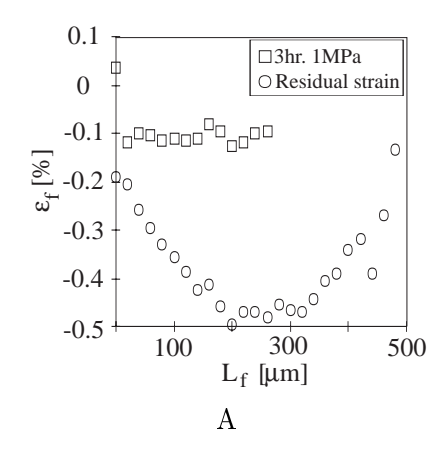


Figure 4.14: Schematic strains along with the fitted curve and the corresponding parameters.

In figure 4.15A the measured fibre creep strain after 3 hours at a load of 1 MPa is shown. The embedded fibre has a length of 480  $\mu$ m. The residual strains are building up in a nearly linear manner until the middle of the fibre where the strain levels off. The magnitude of the measured fibre strain is close to the compressive fracture strain of the used carbon fibres. After 3 hours of creep at a load of 1 MPa, the measured fibre strains are nearly constant, but below zero. The fact that the strain in the fibre is compressive after 3 hours of creep indicates that this load level and the overall matrix creep strain is not sufficient to create tension in the fibre, due to the restraining effect of the initial residual strains from manufacture. In figure 4.15B the corresponding interfacial shear stresses are shown.

The initial residual stress give rise to a symmetric interfacial shear stress distribution. The interfacial shear stress distribution is close to linear along the whole fibre length and reaches a maximum value of 13 MPa at the ends of the fibre. When the specimen is subjected to creep the interfacial shear stress is slowly increasing from the end of the fibre towards the middle and reaches a maximum value of -2 MPa at the end.



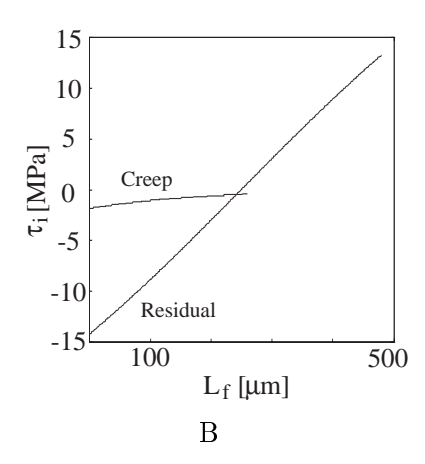
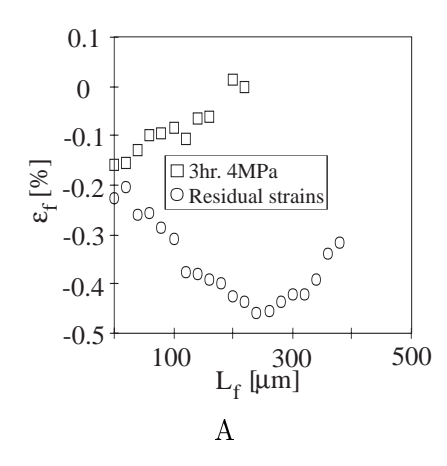


Figure 4.15: A) The initial residual strain and the fibre creep strain after 3 hours at a load of 1 MPa and B) the corresponding interfacial shear stress.



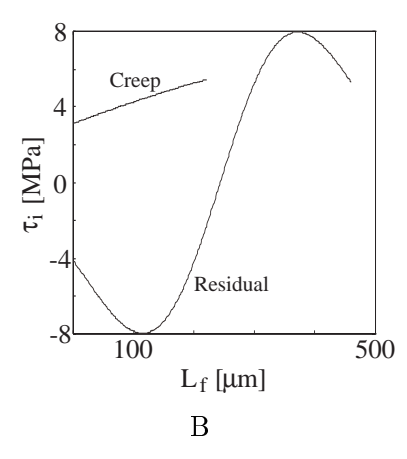
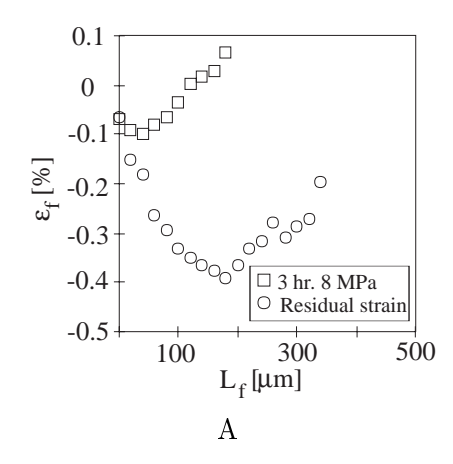


Figure 4.16: A) The initial residual strain and the fibre creep strain after 3 hours at a load of 4 MPa and B) the corresponding interfacial shear stress.

In figure 4.16A the measured fibre creep strain after 3 hours creep at a load of 4 MPa is shown. The embedded fibre has a length of 400  $\mu$ m. Again the residual fibre strain builds up nearly linearly towards the middle of the fibre where it abruptly changes slope and decreases towards the other end of the fibre. The fibre strains after 3 hours of creep at 4 MPa is seen to increase in a slightly nonlinear manner but only reaches a maximum value of approximately zero in spite of the fact that the overall strain after 3 hours of creep is 0.64 %. The interfacial shear stresses are shown in figure 4.16B. The initial residual strain causes interfacial shear stress which also displays a symmetric distribution. The maximum value of the interfacial shear stress is reached approximately 125  $\mu$ m from the ends of the fibre and is  $\pm$  8 MPa. The interfacial shear stress after 3 hours of creep reaches a maximum of 5 MPa at the middle of the fibre. The fact that the interfacial shear stress reaches a maximum at the middle of the fibre is entirely due to the experimental measured strain. Strains have only been measured for half the fibre length and the strain distribution in this situation is of a kind which causes the interfacial shear stress distribu-

tion to be questionable.



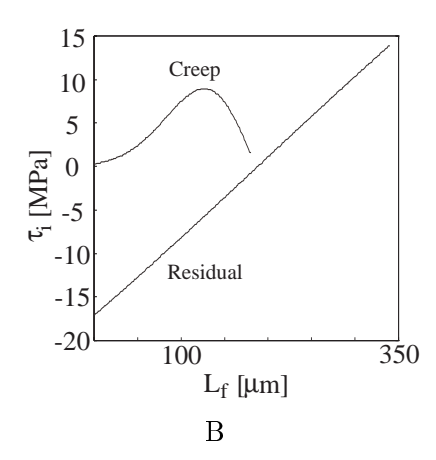


Figure 4.17: A) The initial residual strain and the fibre creep strain after 3 hours at a load of 8 MPa and B) the corresponding interfacial shear stress.

In figure 4.17A the measured fibre creep strain after 3 hours at a load of 8 MPa is shown. The embedded fibre has a length of 350  $\mu$ m. The residual fibre strains are building up in a nearly linear manner and abruptly changes slope at the middle of the fibre. The strain after 3 hours of creep at 8 MPa is now positive in the middle of the fibre and still negative at the end, where the strain profile is nonlinear with respect to the longitudinal coordinate. The interfacial shear stresses are shown in figure 4.17B. The interfacial shear stress, corresponding to the initial residual stress is slightly asymmetric and reaches a maximum value of -17 MPa at the left hand end of the fibre. The interfacial shear stress after 3 hours of creep reaches its maximum at 125  $\mu$ m from the fibre end and is 10 MPa.

The results from the three series of measurements show that the initial residual stress in the fibre is restricting the level of the fibre strain during subsequent creep loading. This is clearly seen since the maximum fibre creep strain in the three situations are compressive, zero and slightly positive, respectively, whereas the overall creep strains of the matrix are 0.15 %, 0.64 % and 1.38 %, respectively. Thus, the matrix strain is highly reduced in the vicinity of the fibre due to the initial residual fibre strain.

## 4.3.2 Mechanical Conditioning/Creep and Creep/Recovery

To further analyse the load carrying capability of the PP-MA composites they were subjected to mechanical conditioning and subsequent creep. In figure 4.18 the results for five consecutive load cycles and subsequent creep at a load of 1 MPa is shown for the whole fibre length. It is seen that the initial residual strain is close to being identical to the strain after the fifth load cycle. Furthermore, the nonlinearity with respect to the longitudinal fibre axis is obvious. The fibre creep strain is only slightly larger than the initial residual strain. This verifies the observations from figure 4.13, namely that the load carrying capability is much larger than compared to the PP-U composites. Additionally, figure 4.18 indicates that the initial residual strain has a restricting effect on the fibre strain since the fibre creep strain after 3 hours at 1 MPa is compressive.

The same experiment was conducted with a load of 4 MPa, and is shown in figure 4.19. Now,

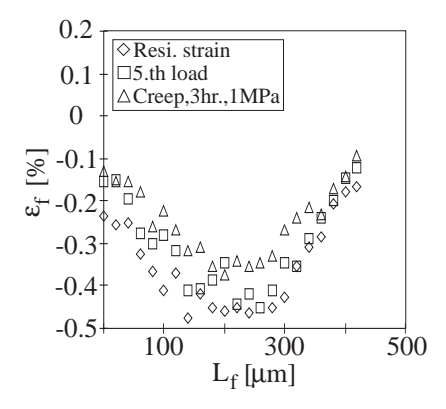


Figure 4.18: The initial residual strain along with the strain after the fifth load application and the 3 hour fibre creep strain at a load of 1 MPa.

the strain after the fifth load application is still very close to the the initial residual strain. The creep strain, shown for half the fibre length, is larger than in the previous load case and tends to being constant along the fibre length. It is important to notice that the creep strain is still compressive even though the overall composite strain is 0.64 %.

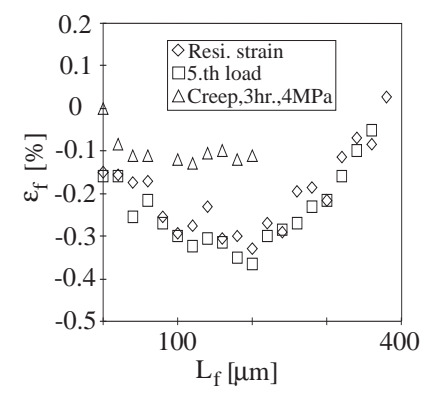


Figure 4.19: The initial residual strain along with the strain after the fifth load application and the 3 hour fibre creep strain at a load of 4 MPa.

The mechanical conditioning of the PP-MA composite does not influence the subsequent creep loading. For loads of 4 MPa the fibre creep strain is different than the fibre strain after the mechanical conditioning, i.e. the interface seems to be intact before creep loading is applied. This indicates that the load transfer mechanism may indeed be due to some kind of bonds formed at the interface.

### Creep and Subsequent Recovery

Now the PP-MA composites were subjected to 3 hours of creep and 4 hours of subsequent recovery. The loads applied were 3 and 7 MPa, respectively. In figure 4.20 the initial residual

strain is shown along with the creep strain for a load of 3 MPa and the recovery strain after 4 hours of recovery.

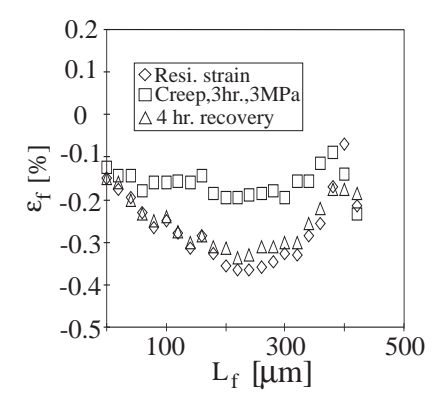


Figure 4.20: The initial residual strain, the creep strain after 3 hours at 3 MPa and the 4 hour recovery strains.

In the situation when the loading is 3 MPa the fibre creep strain is in compression and close to being constant along the length. The recovery strain is almost identical to the initial residual strains with the largest difference at the middle of the fibre where a small increase in strain is observed which is mainly due to the fact that the overall strain after 4 hours of recovery is not exactly zero.

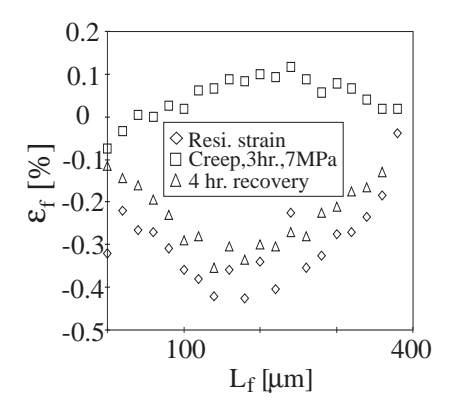


Figure 4.21: The initial residual strain, the creep strain after 3 hours at 7 MPa and the 4 hour recovery strains.

Considering figure 4.21 the load applied to the specimen is 7 MPa. The overall creep strain is now sufficient to cause a tensile strain of magnitude 0.1 % in the middle of the fibre. The recovery strain is now increased compared to the initial residual strain. The maximum increase in strain is at the middle of the fibre and is approximately 0.05 % larger than the initial residual strain. This difference is attributed to the overall strain of magnitude 0.17 %.

Comparison of the results from the mechanical conditioning and the creep/recovery experiments

suggest that the interface in the PP-MA composites are much more damage tolerant than the interface in the PP-U composites. In the PP-MA composites the mechanical conditioning leaves the fibre strain nearly unchanged compared to the initial residual fibre strain, whereas the fibre strain in the PP-U composites after the same loading history are nearly identical to the subsequent fibre creep strain.

## 4.3.3 24/48 hour Creep and Creep at an Elevated Temperature

To further investigate the interfacial quality and the fibre strain profiles of the PP-MA composites, experiments of longer duration and at an elevated temperature were set forth.

In figure 4.22 the initial residual strain and the creep strain after 24 hours are shown. The measurements, in this figure were conducted on a fibre of length 900  $\mu$ m with a fracture at 280  $\mu$ m.

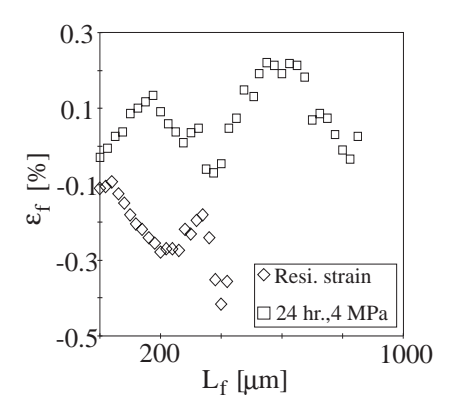


Figure 4.22: Initial residual strain along with the creep strains after 24 hours of loading at 4 MPa.

The initial residual strain is shown for one fragment, whereas the creep strain is shown for two fragments. Even though the initial residual strain is only 0.3 % the figure displays the fact that the fibre retains its load carrying capability for longer loading times as opposed to the PP-U specimens.

In figure 4.22 and some of the previous figures, such as 4.15 and 4.17 a linearity of the strain profiles is observed. This is believed to be due to yielding. This effect has also been reported by Tripathi *et al.* [114], using finite elements. They found that when shear yielding occurred at the fibre ends the normal stress in the fibre builds up linearly. Furthermore, they found that for a given value of applied overall strain the maximum value of stress at the middle of the fibre was controlled by the elastic modulus of the matrix, whereas the maximum obtainable stress in the middle of the fibre is controlled by the tensile yield strain of the matrix. This is depicted in figure 4.23, for two materials with Young's moduli  $E_1$  and  $E_2$  and yield strains  $\varepsilon_1$  and  $\varepsilon_2$ , respectively.

Another interesting feature Tripathi et al. showed is that when the applied strain increases, more stress is transferred from the matrix to the fibre. Therefore the tensile stress in the fibre increases. However, on further application of load, the matrix yields and is less efficient in transferring load to the fibre, thus causing the tensile stress in the fibre to decrease. This effect have also been

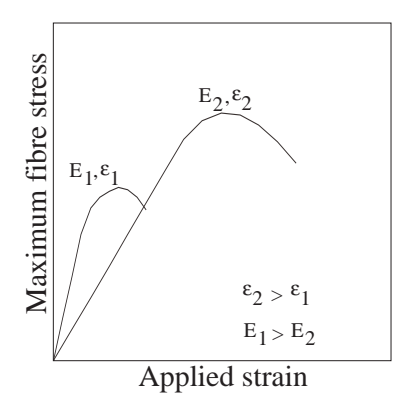


Figure 4.23: Effect of matrix modulus and tensile yield strain of the matrix on the maximum stress in the fibre.

observed in the present investigation. Consider figure 4.24 where the fibre strains are shown after 24 and 48 hours of loading at 4 MPa. It is clearly seen that the creep strains at 48 hours have decreased in comparison to the 24 hour creep strains, which indicates that yielding has occurred at the interface.

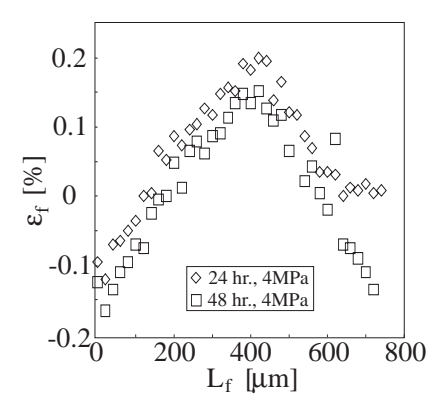


Figure 4.24: The fibre creep strains after 24 and 48 hours of loading at 4 MPa.

#### Creep at an Elevated Temperature

At present it seems that the PP-MA material combination works properly and no damage modes have been observed. However, the viscoelastic nature of the material is magnified at elevated temperatures. The influence of elevated temperature on the creep behaviour was investigated by increasing the temperature to  $60^{\circ}$ C and applying creep loading conditions to the specimens.

The specimen was heated in a small chamber purpose made to fit on the straining rig. The chamber mounted on the straining rig is shown in figure 4.25.

On the chamber a heating element is mounted. The element is controlled through a feed back loop in which the measured temperature on the specimen determines the output from the heating



Figure 4.25: The heat chamber mounted on the testing rig.

element. With this equipment it is possible to apply temperatures in the range -20°C to 120 °C.

The Raman band position of the carbon fibres shift with temperature. This has been investigated by Nielsen [73] who found a linear relationship between Raman band position and temperature. At  $T = 60^{\circ}$  C the zero strain Raman band position is shifted to 2659.4 cm<sup>-1</sup> which is taken into account in the following results.

In figure 4.26 the initial residual strain along with the creep strain for 3 hours creep at 4 MPa at temperature T = 60 °C is shown. At elevated temperatures it is expected that the fibre strain increases due to the larger overall strain for a given applied load. However, the creep strain is only just tensile at the middle of the fibre even though the overall strain is 1.97 %. This may be caused by two things. First, the larger degree of viscoelasticity due to the elevated temperature is increasing stress relaxation in the vicinity of the fibre which lowers the radial pressure on the fibre and thereby decreases the amount of load transferred from the matrix to the fibre. Second, elevation of the temperature may break some of the weak secondary bonds such as dipole bonds or hydrogen bonds formed by the presence of the maleic-anhydride.

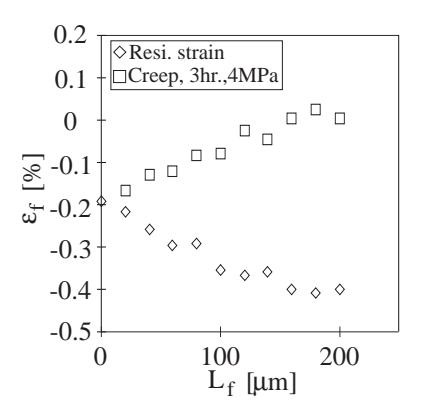


Figure 4.26: Initial residual strain at  $23^{\circ}$  C and creep strain at  $60^{\circ}$  C.

## 4.3.4 Creep Strain in Misaligned Fibres and Fibre Interaction

So far all the fibres have been parallel to the loading axis. However, in real short fibre composites the fibres are dispersed in the matrix and the fibre orientation may range from being parallel to perpendicular to the loading axis. Furthermore, when the loading axis is not parallel to the fibre axis the interface is subjected to larger normal forces which have to be transferred to the fibre. If the interface is weak this loading situation may lead to premature interfacial failure and reduced load transferred to the fibre. In the subsequent figures, the measured data are for 3 hours of loading at 4 MPa along the whole fibre length. The loading situation is shown in figure 4.27.

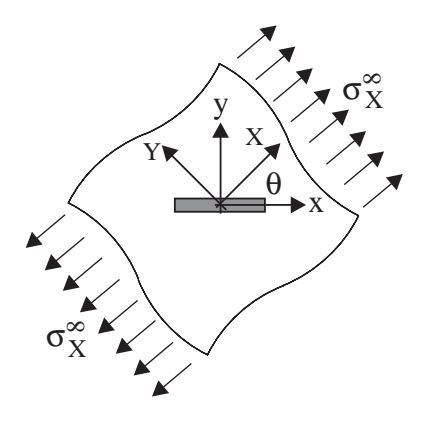


Figure 4.27: The loading situation.

In figure 4.28 the initial residual fibre strain along with the fibre strains after 3 hours creep are shown. The fibre is misaligned by an angle  $\theta=13^{\circ}$ . Along the first 100  $\mu$ m from the fibre ends the creep strain is building up, reaching a maximum value of approximately zero. Then a sudden drop in strain magnitude along the midsection of the fibre is observed. However, the strain along the midsection of the fibre is increased to about one third of the maximum initial residual strain value.

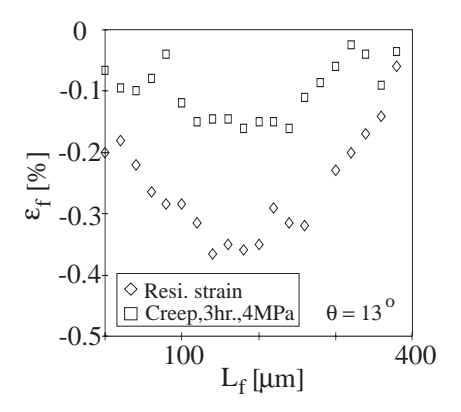


Figure 4.28: Initial residual strain along with the 3 hour creep strain for a load of 4 MPa. The misalignment is  $\theta = 13$ °.

Figure 4.29 shows the initial residual fibre strain along with the fibre strains after 3 hours creep.

The fibre is misaligned by an angle  $\theta=35^\circ$ . The fibre creep strain displays a decrease in magnitude along the fibre midsection. The creep strain magnitude at the fibre midsection is increased as compared to the initial residual strain. However, this increase is smaller than in the previous figure. The maximum creep strain is now approximately 60 % of the maximum initial residual strain.

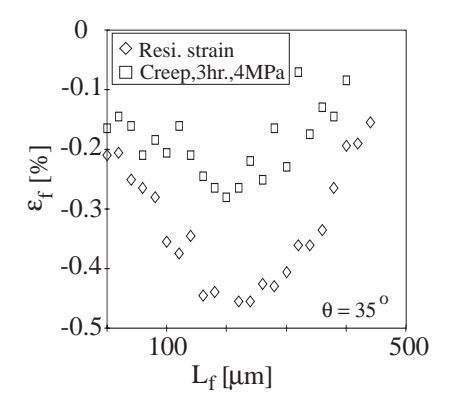


Figure 4.29: Initial residual strain along with the 3 hour creep strain for a load of 4 MPa. The misalignment is  $\theta = 35$  °.

Turning to figure 4.30 showing the initial residual fibre strain along with the fibre strains after 3 hours creep, for a fibre misaligned by an angle  $\theta = 45^{\circ}$ . The same tendencies appear, i.e. the creep strain in the midsection of the fibre is increased as compared to the initial residual strain. However, the increase is even smaller than previously observed. The maximum fibre strain after 3 hours of loading is now only increased to about 80 % of the maximum initial residual strain.

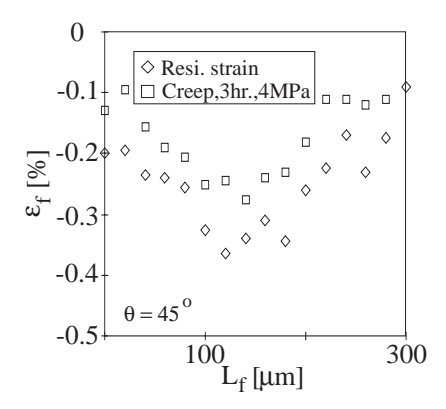


Figure 4.30: Initial residual strain along with the 3 hour creep strain for a load of 4 MPa. The misalignment is  $\theta=45$  °.

The next set of measurements were conducted on a fibre misaligned by an angle of  $\theta = 87^{\circ}$ . Figure 4.31 shows the initial residual fibre strain along with the fibre strains after 3 hours creep. Now the "drop" in creep strain along the midsection of the fibre is continuous along the whole fibre length. This is clearly due to the transverse contraction of the specimen, thus the fibre

strains are affected by the Poisson effect, and the creep strain is numerically larger than the initial residual strain.

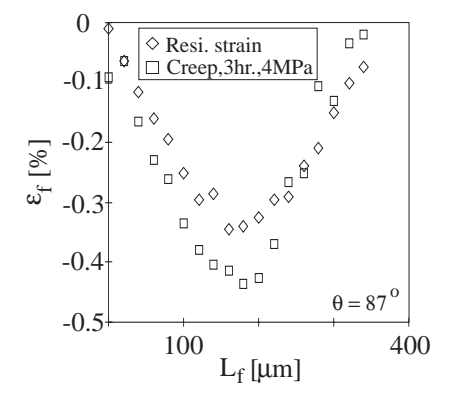


Figure 4.31: Initial residual strain along with the 3 hour creep strain for a load of 4 MPa. The misalignment is  $\theta = 87^{\circ}$ .

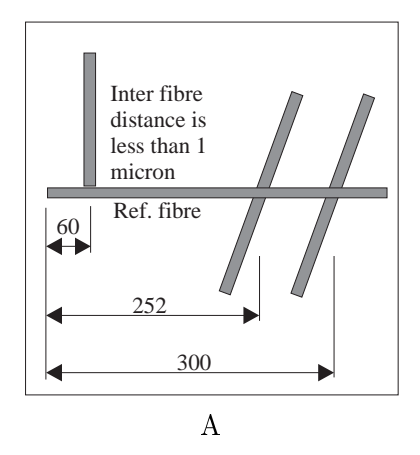
The previous observations clearly indicate that the fibre creep strain is decreasing as the misalignment angle,  $\theta$ , varies from  $0^{\circ}$  to  $90^{\circ}$ . This is due to two mechanisms. The first is the loading condition. As the misalignment angle increases the transverse loading of the interface is increased which reduces the effect of the radial pressure and thus the amount of load transferred to the fibre.

The second mechanism is due to the Poisson effect. The Poisson contribution to the longitudinal strain is increased as the misalignment angle increases and when the fibre is orthogonal to the loading direction it will experience compression only. In the situation when the fibre is nearly orthogonal to the loading direction the absolute value of the fibre strain gradient increases when the specimen is subjected to creep loading. This indicates that the interface is relatively strong. If the interface is weak the additional amount of load transferred to the fibre will only be due to compression at the fibre end and no increase in the fibre strain gradient will be observed.

#### Fibre Interaction

In this section the effect of adjacent fibres on the strain in a reference fibre is investigated. This investigation does not cover all aspects of interaction but should merely be considered as preliminary because interaction is not the primary object of this thesis. This series of investigation was carried out in order to see if interaction between fibres has a pronounced effect on the strain in a reference fibre.

In figure 4.32A the fibre configuration is shown, and the result of the interaction on the residual strain and the creep strain is shown in figure 4.32B. At 60  $\mu$ m from the left hand end of the reference fibre, a fibre is situated orthogonal to the reference fibre. The effect of this fibre is barely reflected in the residual strains, and only a slight increase is seen in the creep strain. The increase in creep strain is so small that it may be due experimental scatter. At the other end of the reference fibre two interacting fibres are overlapping. The effect of these fibres are seen in both the initial residual strain as well as in the creep strain as a decrease in the initial



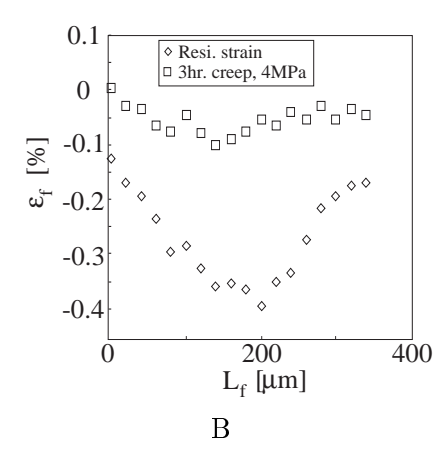
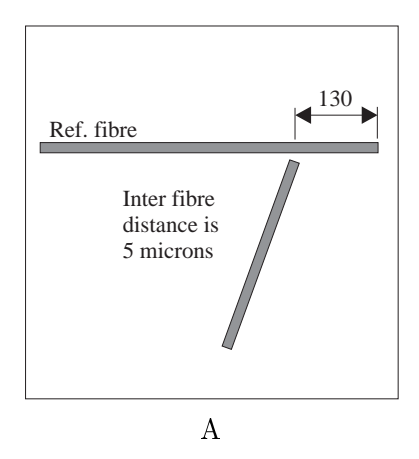


Figure 4.32: Fibre interaction: A) the fibre configuration and B) the fibre strains in the reference fibre. (Dimensions are in  $\mu$ m.)

residual strain level and a leveling off of the creep strain. If it is assumed that the initial residual strain is symmetrical without these two fibres being present, it seems that the strain level at the right hand end of the reference fibre is increased by approximately 0.1 %. The creep strains are not increased but seems to be leveling off at a constant value just below zero. The reason for this might be due to a combination of both yielding and a decrease in radial pressure on the reference fibre due to interaction.



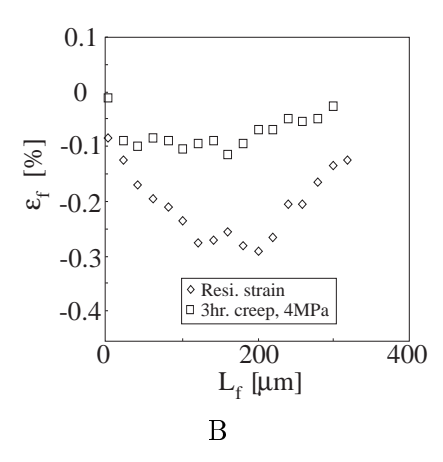
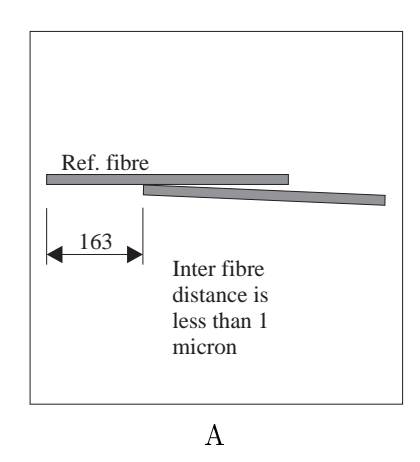


Figure 4.33: Fibre interaction: A) the fibre configuration and B) the fibre strains in the reference fibre. (Dimensions are in  $\mu$ m.)

In figure 4.33A the fibre configuration is shown, and the result of the interaction on the residual strain and the creep strain is shown in figure 4.33B. This pair of figures repeats the observations from the previous figures. The fibre situated at 130  $\mu$ m from the right hand end of the reference fibre causes the initial residual strain to decrease by 0.05 - 0.1 %, and the creep strain levels off at the right hand end of the fibre.

In figure 4.34A the fibre configuration is shown, and the result of the interaction on the residual



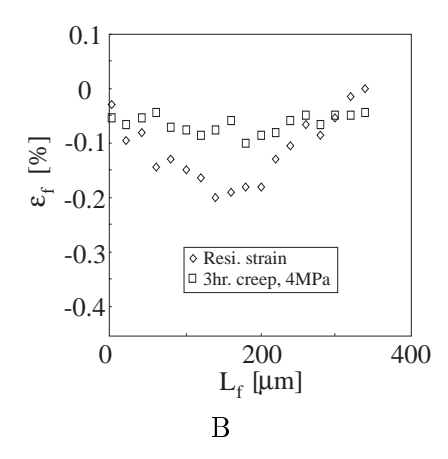


Figure 4.34: Fibre interaction: A) the fibre configuration and B) the fibre strains in the reference fibre. (Dimensions are in  $\mu$ m.)

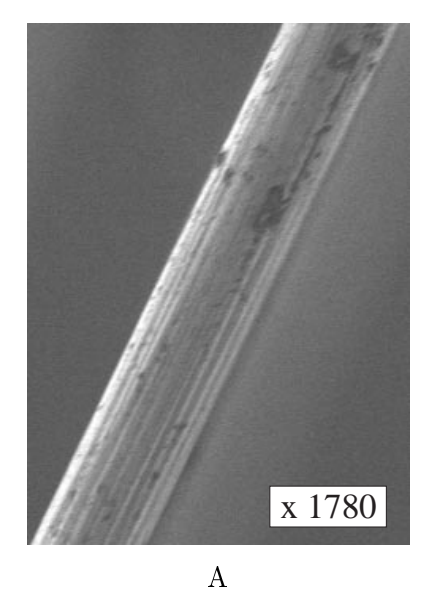
strain and the creep strain is shown in figure 4.34B. The interacting fibre is now almost parallel to the reference fibre and and a clear shielding effect is observed. The interacting fibre drastically reduces the residual strain in the reference fibre. The creep strain is also affected by the interacting fibre. Although the creep strains are close to zero all along the fibre length it is obvious that the presence of interacting fibre causes the creep strain to level off at the right hand end of the reference fibre. Extensive shear yielding between the two fibres decreases the efficiency with which the matrix transfers load to the fibre and thus the loading of the reference fibre decreases.

Several other investigators have considered interaction between fibres, such as Schadler et al. [95], Chohan and Galiotis [15], Wagner et al. [117] and Grubb et al. [35], who found the strain concentration factor, adjacent to a fibre break, to be approximately 1.5 for carbon fibres and 1.1 for kevlar fibres and the interaction distance to be around 5 fibre diameters for carbon fibres. In the present investigation the results indicate that the interaction distance is much smaller due to both viscoelastic effects and yielding. Furthermore, it seems that interaction is very dependent on fibre arrangement. As seen in figure 4.32B the interacting fibre at the left hand end has - if any - only a very small effect on the strains in the reference fibre, whereas overlapping fibres or nearly parallel fibres have an effect. This suggests that interaction between fibres is even more complicated when the response of the investigated model composite is not linear elastic. However, the interaction effect in the viscoelastic situation is not believed to be as pronounced as in the linear elastic situation, where interacting fibres causes fibre breaks and large strain concentrations.

### 4.3.5 Fibre Surface Morphology

The former investigations have indicated that the load transfer efficiency of the PP-MA composites is somewhat larger than that of the PP-U composites. In order to clarify the reason for this difference the fibre surfaces have been investigated by scanning electron microscopy and the micrographs of the fibre surfaces for the plasma treated fibres and standard surface treated fibres are shown in figure 4.35.

Figure 4.35B shows that the standard treated fibres have deep continuous grooves on the surface along the fibre axis, whereas the plasma treated fibre, figure 4.35A, has a more smooth surface with dark flakes. Remembering that the plasma treated fibres originally were the same as the



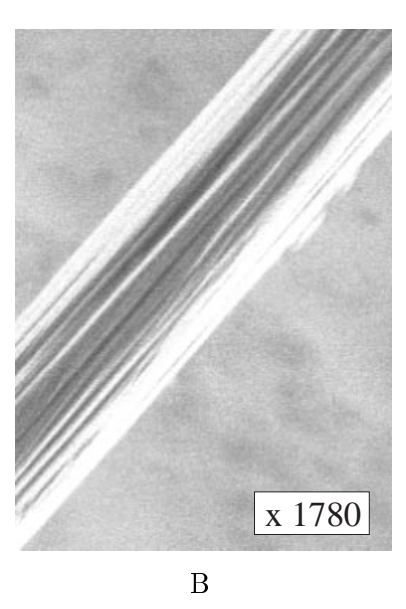


Figure 4.35: SEM micrographs of: A) a plasma treated fibre and B) a standard surface treated fibre.

standard fibre, it is clearly seen that the removal of an outer layer from the fibre have taken place. Indeed, the mean fibre diameter is less for the plasma treated fibre, (6.1  $\mu$ m), as compared to the standard fibres which have a mean diameter of 6.7  $\mu$ m.

These investigations indicate that interpenetration of the matrix into the fibre is improved due to the larger grooves on the standard treated fibres. The effect of maleic-anhydride and the relatively large grooves on the fibre surface increases the interfacial adhesion by possible bonding mechanisms and mechanical interlocking and thus enhancing the performance of the composite. The quantitative effect of the plasma treatment and the maleic-anhydride in terms of interfacial strength is investigated in more detail in the following section.

## 4.4 Interfacial Strength

This section deals with the determination of the interfacial shear strength as obtained from compressive fragmentation and from the strains measured by MRS.

Compressive fractures were observed in the PP-MA composites but not in the PP-U composites, indicating that the interfacial strength is increased due to presence of the maleic-anhydride and the deep continuous grooves on the fibre surface. The compressive fragmentation, used to determine the interfacial strength is discussed in terms of critical length and load transfer assumptions.

#### The Fragmentation Test

The fragmentation test is commonly used as a tool for evaluating the nature and quality of the interfacial adhesion in numerous fibre/matrix systems. In traditional fragmentation testing a single fibre is embedded in a matrix which is subjected to a monotonically increasing tensile strain in the direction of the fibre axis. Load transfer to the fibre then develops through shear

stresses at the fibre-matrix interface. Since the fibre failure strain is usually lower than that of the matrix, the fibre will progressively fracture into an incrasing number of fragments as the applied strain increases. The fragmentation process continues for higher levels of applied strain until a saturation level is reached. At this saturation stage the interfacial shear stresses are no longer capable of inducing further fracture of the fibre fragments. Although the fragmentation test is a single fibre test it tends to be employed to reproduce the microdamage occurring at the interface of multifibre composites during loading. The results from single fibre fragmentation tests might not be applicable for real composites but for evaluating different fibre/matrix systems it is adequate if the load transfer assumptions apply to the investigated fibre/matrix system.

The work of Kelly and Tyson [49] provided a tool for semi-empirical analysis of the test data from which interface properties can be deduced. This model, however, is based upon the assumption that the interfacial shear stress is constant at the interface. This assumption is only strictly valid if shear yielding occurs at the interface. The assumption, however, is a very good approximation in the case of frictional load transfer where the interfacial shear stress is also constant along the fibre. Kelly and Tyson also assumes that the fragment length at saturation is uniformly distributed in the interval  $l_c/2 < l_{frag} < l_c$ , where  $l_c$  is the "critical length" defined as the maximum fragment length at which the fibre will not break, regardless the level of applied strain.

Several attempts to model the stress field and evaluate the fragmentation test have been undertaken. The first load transfer model, still used widely, was the shear-lag analysis by Cox [18]. This model is a one dimensional model and makes use of the "matrix radius",  $R_m$ . This model does not take the effect of the radial and hoop stresses at the interface into account and in particular the radial stresses are affecting the load transfer efficiency. Whitney and Drzal [125] proposed a model based on the theory of elasticity but used shear-lag knowledge about the interfacial shear stresses in the solution. Furthermore, the stress in the fragments have been shown to be invalid for fragments with aspect ratios less than 50:1, [26].

McCartney [63] and Nairn [70] used variational mechanics to obtain a solution in the case of perfect bonding between an elastic matrix and elastic fibre. These solutions satisfies the equilibrium and boundary conditions exactly. Two of the four stress-strain relations in the cylindrical co-ordinate system are satisfied in an average sense in the McCartney model and the model of Nairn satisfies the compatibility equations approximately. In both these models the axial stress is assumed to be independent of the radial co-ordinate.

The most recent model has been proposed by Wu et al. [128], [129]. The model is established by modified variational mechanics based on the principle of minimum complementary energy. In the development of this model it is assumed that the axial stress is independent of the radial co-ordinate in the fibre, whereas it has a non-linear dependence of the radial co-ordinate inside the matrix. This model provides simpler final expressions than the former ones and has the capability of taking into account an interphase with properties differing from those of the fibre and matrix.

All these models consider perfect bonding and elastic materials, which is not always the case with polymeric composites. During fragmentation it is likely that interfacial debonding, local plastic flow or even matrix cracking occurs. This will have to be taken into account in order to fully be able to interpret the results from the fragmentation test.

Nairn and Liu [71] established a model based on Bessel-Fourier series which satisfies equilibrium and compatibility equations exactly and most of the boundary conditions. The approximation is that the axial stress in the fibre end at a break is only zero in an average sense. The model, however, is capable of taking into account the effect of imperfect interface or interphase and anisotropic fibres. Another model capable of taking the effect of a non-perfect interface into account has been proposed by Dollar and Steif [20] who used Muskhelishvilis complex stress po-

tentials to describe the load transfer in composites with a Coulomb friction interface. Finally Varna et al. [115] used finite element analysis incorporating interfacial debonding to evaluate the interfacial toughness from the fragmentation test.

In all the aforementioned models the main purpose has been to describe the load transfer and the resulting stress distribution in various single fibre composite systems. It is a well known fact, however, that brittle fibres such as carbon fibres do not have a fracture stress which can be uniquely described by a scalar variable. It is necessary to take into account that the fracture stress of these fibres are distributed in some way.

The Weibull distribution [122] has been used widely to describe failure situations. This distribution has been used in the analysis of failure of electronic components, ball bearings and motors as well as for the study of breaking strength and fatigue in textiles and for analysing particle size data [61] and in recent years in conjunction with the fragmentation test.

As such the Weibull distribution has been used in various aspects of the fragmentation test by Lienkamp and Schwartz [55], Lacroix *et al.* [51], [52], Baillie and Bader [3], Wagner *et al.* [118], Hui *et al.* [46], Huang and Young [42] and Wood *et al.* [126], [127].

#### 4.4.1 Results

As mentioned earlier the fragment lengths in the dog bone specimens used for subsequent creep experiments were measured after manufacture. 233 fibre fragment lengths in the PP-MA specimens were measured and the cumulative fragment length distribution is shown in figure 4.36.

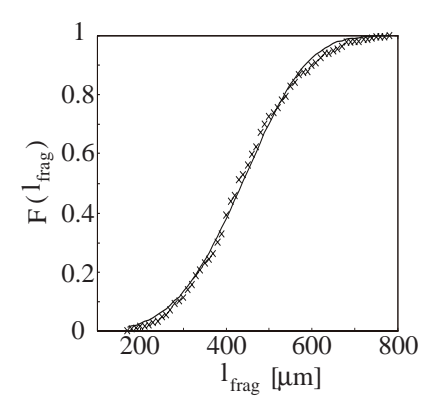


Figure 4.36: The cumulative fragment length distribution.

The fragment length distribution has been fitted to both a two-parameter Weibull distribution as well as a Gaussian distribution (not shown), but the Weibull distribution was found to be the best in a least squares sense. The two-parameter Weibull distribution is given as [61]

$$F(l_{frag}) = 1 - exp\left(-\left(\frac{l_{frag}}{\eta}\right)^{\beta}\right) \tag{4.4}$$

where  $l_{frag}$  is the fragment length,  $\eta$  is the scale parameter and  $\beta$  is the shape parameter. The values of  $\eta$  and  $\beta$  are 477.5  $\mu$ m and 4.16, respectively.

The mean fragment length is now obtained as

$$\langle l_{frag} \rangle = \eta, \ \left( 1 + \frac{1}{\beta} \right)$$
 (4.5)

where , is the gamma function and the value of the mean fragment length is  $\langle l_{frag} \rangle = 434~\mu \mathrm{m}.$ 

From the figure it is seen that the two-parameter Weibull distribution describes the fibre fragment lengths best at intermediate lengths. For small and large fibre fragment lengths the Weibull distribution deviates slightly from the experimental data. This effect is easier seen if  $\ln(-\ln(1-F))$  is plotted against  $\ln(\frac{l_{frag.}}{d_f})$  as shown in figure 4.37.

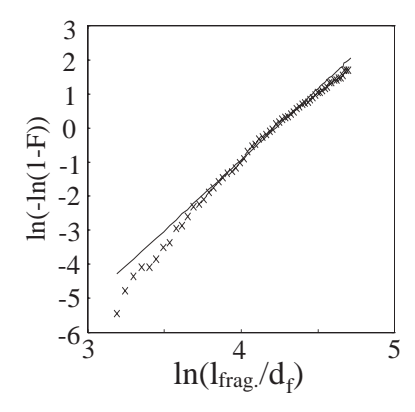


Figure 4.37: Weibull distribution of fibre fragment aspect ratios.

This deviation have been pointed out by several investigators including Huang and Young [42] in their investigation of PAN and pitch-based fibres.

In the traditional fragmentation analysis the critical fragment length can now be found as 4/3 times the mean fragment length, but Lacroix et al. [51] have shown that the critical length is not always a material parameter but it depends on the load transfer model used and Feillard et al. [26] concludes that there exists no analytical relationship between the mean fragment length and the critical length. With these findings in mind, the mean fragment length is used as an input parameter in the following determination of the interfacial shear strength.

The Weibull distribution of fibre strength has mostly been used to simulate the tensile stresses of brittle fibres but Melanitis and Galiotis [64], and Wood et al. [126],[127], have investigated the compressional behaviour and the compressional fragmentation of carbon fibres, respectively. Melanitis and Galiotis used a bending rig for the compression tests of HM carbon fibres and found a strain to break of  $0.45 \% \pm 0.05$ , regardless of fibre length.

The assumption made by Kelly and Tyson regarding yielding in the interface has been questioned by Piggott [82], [83], [84] who claims that yielding at the interface does not occur. These conclusions are made on the basis of a Cox model, the rule of mixtures and macroscopic tensile tests.

He also suggests that a new failure process should be considered since polymers do not fail in shear but in tension at 45° to the shear plane, [80], [81].

In the present analysis, however, it is assumed that the maximum interfacial shear stress can be regarded as a constant due to either yielding or as a result of the viscoelastic nature of the 4.5. Summary

polymer. Furthermore, it is assumed that the maximum stress in the interface obeys the Von Mises yield criterion, which states that at the onset of yielding the second invariant of the deviatoric stress tensor equals some constant depending only on the material

$$J_2 = \frac{1}{2} s_{ij} s_{ij} = \frac{\sigma_Y^2}{3} \tag{4.6}$$

where  $\sigma_Y$  is the yield stress obtained from a uniaxial tensile test. In pure shear the shear yield strength equals

$$\tau_Y = \frac{\sigma_Y}{\sqrt{3}} \tag{4.7}$$

For polypropylene the tensile yield strength is  $\sigma_Y = 30$  MPa and thus the shear yield strength is  $\tau_Y = 17$  MPa. Using the maximum value of the mean fibre strain, (0.39 %), and assuming that  $\sigma_f = E_f \varepsilon$  the fracture stress equals 1365 MPa. Inserting this into the Kelly - Tyson equation gives the interfacial shear strength for the PP-MA composite system

$$\tau_{iu} = \frac{\varepsilon_{fu} E_f d_f}{2\langle l_{frag} \rangle} \tag{4.8}$$

 $\tau_{iu}$  is thus calculated to be 11 MPa.

The PP-U composite were subjected to the same investigation, but no fibre fragments were found, even for fibres longer than 1 mm. Before subsequent creep load application the residual fibre strains were measured in all the investigated fibres. In the PP-U specimens the fibre strain variation along the fibre length were found to be linear - regardless of fibre length and the mean value of the initial residual strain has been shown earlier to be

$$\varepsilon_f = -0.35x - 0.1456 \tag{4.9}$$

from this expression the interfacial shear stress is obtained as

$$\tau_i = \frac{E_f d_f}{4} \left( \frac{d\varepsilon_f}{dx} \right) \tag{4.10}$$

yielding a value of  $\tau_i = 2.1$  MPa.

It is commonly suggested that the interface is a phase with mechanical properties differing from those of the matrix and fibre. Since these properties are unknown the calculated values of the interfacial shear strength are believed to be reasonable. The value of 11 MPa is in fact in very close correlation with the value found by Folkes [27] who found that quenched PP samples had a shear yield strength and tensile yield strength of 13.1 MPa and 18.6 MPa, respectively.

It is obvious from this investigation that standard carbon fibres and PP-MA constitutes a material combination that will result in a larger interfacial shear strength.

## 4.5 Summary

Model composites consisting of two material combinations have been investigated in order to gain insight into the load transfer mechanisms between the matrix and fibre.

Various loading histories have been applied since the loading history by itself may have an influence on the load transfer quality.

The model composites consisting of plasma treated fibres and unmodified polypropylene, (PP-U composites), have been shown to display a friction-like load transfer. Due to the linearity of the measured fibre strains it was expected that the load transfer in the PP-U model composites was not due to a perfect bonding between the fibre and matrix. This was expected because the initial elastic fibre strains are very similar even for different applied loads and for loads of 7 MPa the fibre strains are close to zero. Additionally, the initial residual fibre strain showed a linear dependence of the longitudinal fibre co-ordinate.

Different loading histories did not show pronounced differences which lead to the conclusion that the load transfer mechanism has frictional character since viscoelastic effects present in the matrix material do not alter the fibre strains during creep loading conditions.

Furthermore, the results indicate that the magnitude of the load transfer between the matrix and fibre reached a saturation level governed by the initial residual stresses and the coefficient of friction.

For longer loading times the fibre creep strains were shown to be very close to zero, indicating that a PP-U composite will not perform as intended, which is also supported by observations of fibre pull-out.

SEM micrographs were taken of the plasma treated fibres and these investigations revealed some of the reasons for the poor interfacial quality. The fibres have a relatively smooth surface which suppresses mechanical interlocking. Finally, the interfacial shear strength was calculated from measured fibre strains and found to be 2.1 MPa.

The other material combination consisting of fibres with a standard surface treatment embedded in a polypropylene matrix grafted with maleic-anhydride, (PP-MA composites). These model composites displayed a much more efficient load transfer. In fact the load transferred per millimeter fibre length is 3 times higher than in the PP-U composites. Also the maximum initial residual strains are 1.5 times larger than the initial residual fibre strain in the PP-U composites, which corresponds to -0.39 % which is close to the compressive fracture strain found by other investigators. The various measurements on the PP-MA composites showed that the initial residual fibre strains along with the apparently strong interface has a strong restricting effect on the fibre strains during creep. This manifests itself in the fact that the load has to be larger than 4 MPa for the fibre strain to be tensile after 3 hours of creep.

Some of the fibre strains showed pronounced linearity with respect to the longitudinal fibre coordinate which is attributed to shear yielding at the interface. This has also been reported by other authors along with the interesting fact that for increasing loading times the fibre strain decreases. This effect have been observed in the present investigation as well. This is due to the fact that when the applied strain increases, more stress is transferred from the matrix to the fibre. Therefore the tensile stress in the fibre increases. However, on further application of load, the matrix yields and is less efficient in transferring load to the fibre, thus causing the tensile stress in the fibre to decrease.

Fibre misalignment has been considered and it was found that the fibre strain decreases towards values smaller than the initial residual strain as the misalignment angle increased. This is assumed to be due to two mechanisms. First the loading condition itself. As the misalignment angle increases the transverse loading of the interface increases, reducing the effect of the radial pressure and thus the amount of load transferred to the fibre. Secondly, the Poisson contribution 70 4.5. Summary

to the longitudinal strain is increased as the misalignment angle increases and when the fibre is orthogonal to the loading direction it will experience compression only.

Preliminary investigations of fibre interaction have been undertaken. Although the results are preliminary it seems that the interaction distance is much smaller than in the elastic case. Furthermore, it seems that interaction is very dependent on fibre arrangement. This suggests that interaction between fibres is even more complicated when the response of the investigated model composite is not linear elastic.

SEM micrographs were taken and the fibre surface was found to be much more rough than the plasma treated fibres thus enhancing mechanical interlocking which combined with the maleicanhydride yields a stronger interface. The interfacial shear strength has been calculated from the Kelly-Tyson equation together with the mean fragment length and was found to be 11 MPa, or more than five times as strong as for the PP-U composites.

5

# Single Fibre Creep Modelling

This chapter describes two approaches to modelling the stress and strain fields due to one fibre in a viscoelastic matrix material. The first one is partly theoretical and partly experimental, i.e. the strains obtained from experiments are used as input to a theoretical approach describing the matrix strains at the instant of time when the fibre strains were measured. The second approach is purely theoretical and incorporates the effect of thermal stress induced in the specimen after manufacture.

When a solid is used in a situation which may involve significant loading and deformation it is essential that adequate design should be included in the manufacture of the component. This may be necessary to ensure efficient material utilisation, to prevent unacceptable deformation during service or to avoid failure of the component. In part these design requirements can be met by providing methods for stress and deformation analysis for the relevant material behaviour. Essentially this requires some form of theory to model the behaviour, experimental techniques for measuring the material parameters, and methods for calculations relevant to the application. Obviously the degree of sophistication employed will be governed by the application and the methods of calculation may involve detailed mathematical or numerical analysis or the use of simplified engineering theories. Whatever method is employed the theoretical basis and experimental data should have a corresponding degree of sophistication.

Due to the fact that only one component of the fibre strain is measured by Raman spectroscopy there would be a sophistication discrepancy between the experimental data and the theoretical modelling if a highly sophisticated model were used. On this basis two simpler but adequate approaches will be proposed in this chapter.

Since the matrix is the load transferring media, it is crucial that a theoretical model describes the field quantities in the matrix properly. It is important to have an adequately qualitative description of the field quantities in order to improve the overall performance of the composite, e.g. optimise the creep strength by enhancing interfacial properties and to understand the mechanisms of the load transfer.

The main objective in the present study is to investigate the localised phenomena from a micromechanical point of view.

Similar investigations using various approaches have been undertaken by other researchers, such as Pachalis and Chou [76] who developed a model for predicting the steady-state creep behaviour

of misaligned short-fibre reinforced ceramic matrix composites. Their model is based on an advanced shear-lag model. One of the major assumptions in their analysis is that there is no stress transfer from the matrix to the fibre at the fibre end surface.

The authors analyses the effect of fibre orientation and the effect of the coefficient of sliding friction between the matrix and the fibre.

It is shown that the creep rate increases - with increasing orientation angle - until the fibre orientation angle reaches about 60 degrees, relative to the loading axis, where the creep rate reaches an asymptotic value. At low values of the coefficient of sliding friction the composite behaves as a pure matrix with holes.

No experimental data for comparison or validation of their model have been shown.

Sørensen [111], investigated the creep behaviour of short fibre reinforced metal-matrix composites. The experimental work included creep tests and neutron diffraction tensile tests at elevated temperatures, performed on SiC-whisker reinforced aluminium. Calculations were carried out using finite elements.

In the numerical analysis the fibres were assumed to be perfectly bonded to the matrix material. Using a hyperbolic sinusoidal creep law Sørensen analysed the effects of inclusion shape and fibre misalignment. It was found that for inclusions of circular cross section the volume fraction has to be approximately twice that of a square cross section fibre to give the same creep resistance. The misalignment of the fibres gives rise to a lower creep resistance due to the lower constraining of the fibre on the matrix. Furthermore, it is seen that the larger misalignment the larger rotation of the fibres towards a parallel position.

Comparison of experimental results with numerical calculations show that the stresses found in the experiments are larger than the those predicted by the model. This might be caused by dislocation-particle interaction, (e.g. Orowan looping), and that the oxide particles in the aluminium powder serve as barriers to dislocation movements.

Goto and McLean [33], developed a shear lag-like model and used it to analyse the effect of various interfaces on the creep behaviour in metal-matrix composites.

It was assumed that the matrix deformation obeys power law creep and that no load is transmitted along the fibre ends. By applying the rule of mixtures the creep rate of a unit cell, containing one fibre, was obtained. Introducing an interface of thickness,  $\delta$ , enables the description of the creep rate in terms of a parameter which can be regarded as describing the creep strength of the interface. According to the authors there are only very few results against which this model can be validated.

The principal prediction from this model is that the interface strength influences the creep behaviour strongly, meaning that if the interface has no strength, the creep resistance of the composite is lower than that of the pure matrix. Furthermore, the creep performance is sensitive to fibre aspect ratio and fibre volume fraction.

Song et al. [109], analyses continuous fibre reinforced ceramic- and metal-matrix composites. A cylindrical cell model was considered. This cell model consists of one broken fibre which is influenced by six intact surrounding fibres. The matrix is assumed to obey power law creep and the fibres are assumed to be isotropic linear elastic and perfectly bonded to the matrix. The calculations are carried out using finite elements.

It was found that the presence of the broken fibre has great influence on the creep strain rate. If broken fibres are present the creep strain rate does not stabilise, not even after very long time. Creep strains are concentrated at the crack tip region and the creep zone expands with time, primarily along the fibre-matrix interface. This is caused by the large shear stress induced by the crack in the interface. This may cause interface sliding and have a pronounced effect on the relaxation of the matrix stresses. No experimental results for verification are shown, but the

model is compared to other models and shows reasonable agreement.

Wang and Chou [121], proposed a model based on advanced shear lag theory. The shear lag approach is applied to a unit cell containing one fibre, which can be "misaligned" by an angle  $\theta$  relative to the loading axis.

It is assumed that both the fibre and the matrix creep but at different rates. Both phases are assumed to carry axial and shear loads. Furthermore, sliding along the interface is considered and a sliding factor is incorporated in the analysis. Power law creep is assumed for uniaxial tension and the Prandtl - Reuss flow rule used in order to account for three dimensional stress states. A linear distribution of the interfacial shear stress is assumed and the rule of mixtures is applied to solve the problem.

Numerical calculations show that the longitudinal creep strain rates with perfect and no bonding are 31 % and 80 % of the pure matrix, respectively.

The longitudinal creep controls the unit cell when the fibre "misalignment angle" is less than  $15^{\circ}$ , the shear creep becomes dominant when  $\theta$  is between  $15^{\circ}$  and  $75^{\circ}$ , and the transverse creep contributes mostly to the creep strain rate when the angle is larger than  $75^{\circ}$ . When the interfacial sliding factor becomes high, (weak bonding), the resistance to shear and transverse creep diminishes.

## 5.1 Creep Modelling, Approach I

In this section a semi - theoretical approach is outlined in order to describe the local matrix creep strains and has also been used in Schjødt-Thomsen and Pyrz [104]. The approach is semi - theoretical, i.e. it uses experimental results as an input parameter for the modelling and thus the creep strains are only obtained at a loading time corresponding to the time, during the experiment, at which the measurement was conducted.

This approach is inspired by Fukuda and Kawata [28]. They used the concept of point forces in an infinite plate to investigate the elastic stresses and strains in a composite with a regular array of fibres. The interfacial tractions for one fibre due to an externally applied load are calculated. These tractions are integrated along the boundary of the fibre, thereby giving the stresses in the matrix material.

In Fukuda and Kawata's analysis it is assumed that the stresses and strains are identical for all the fibres in the array. For one fibre the results obtained are quite good compared to experiments.

The present approach differs from Fukuda and Kawata's by incorporating the actual variation of interface tractions along the fibre boundary, as obtained through force equilibrium at the interface based on the fibre strains from the MRS investigations. The interfacial stresses along the fibre are obtained from the actual fibre strain at various times. The interfacial stresses are then integrated along the fibre boundary giving the stresses in the matrix material. The matrix stresses are then inserted into the three dimensional constitutive equation of the matrix, thus giving the creep strain distribution in the matrix material around the fibre. Additionally, this model is able to consider misalignment of the fibre.

#### **Pointforces**

In modelling the forces acting on the interface between the fibre and the matrix material, only the interfacial shear stress,  $\tau_{xy}^*$ , and the transverse normal tractions,  $\sigma_y^*$ , are considered.

The stresses in the matrix,  $\sigma_{ij}^{(1)}$ , due to the applied load,  $\sigma_{IJ}^{\infty}$ , are given by

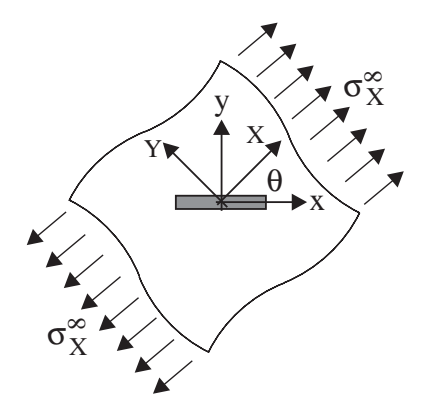


Figure 5.1: The figure shows the loading situation.

$$\left\{ \begin{array}{l} \sigma_x^{(1)} \\ \sigma_y^{(1)} \\ \sigma_{xy}^{(1)} \end{array} \right\} = \left[ \begin{array}{ccc} m^2 & n^2 & 2mn \\ n^2 & m^2 & -2mn \\ -mn & mn & (m^2 - n^2) \end{array} \right] \left\{ \begin{array}{l} \sigma_X^{\infty} \\ \sigma_Y^{\infty} \\ \sigma_{XY}^{\infty} \end{array} \right\}$$
(5.1)

where capital letters refer to the global coordinate system.  $m = \cos \theta$ ,  $n = \sin \theta$  and  $\theta$  is the angle between the fibre x axis and the global X axis, as shown in figure 5.1.

From Timoshenko [113], it is known that a force, P, acting in the x-direction at a point  $(x_0, y_0)$  in an infinite plate creates the stresses  $\sigma_x(x, y)$ ,  $\sigma_y(x, y)$  and  $\tau_{xy}(x, y)$  given by

$$\sigma_{x}(x,y) = \frac{P}{4\pi} \frac{(x-x_{0})}{(x-x_{0})^{2} + (y-y_{0})^{2}} \left\{ -(3+\nu) + 2(1+\nu) \frac{(y-y_{0})^{2}}{(x-x_{0})^{2} + (y-y_{0})^{2}} \right\}$$

$$\sigma_{y}(x,y) = \frac{P}{4\pi} \frac{(x-x_{0})}{(x-x_{0})^{2} + (y-y_{0})^{2}} \left\{ (1-\nu) - 2(1+\nu) \frac{(y-y_{0})^{2}}{(x-x_{0})^{2} + (y-y_{0})^{2}} \right\}$$

$$\tau_{xy}(x,y) = \frac{P}{4\pi} \frac{(y-y_{0})}{(x-x_{0})^{2} + (y-y_{0})^{2}} \left\{ (1-\nu) + 2(1+\nu) \frac{(x-x_{0})^{2}}{(x-x_{0})^{2} + (y-y_{0})^{2}} \right\}$$
(5.2)

Equations (5.2) are used to find the stresses in the matrix material after rewriting them and replacing P by the interfacial stresses as

$$\sigma_{x}^{(2)}(x,y) = \frac{1}{4\pi} \int_{0}^{l_{f}/2} \tau_{xy}^{*}(\xi) \left[ \frac{(x-x_{1})}{(x-x_{1})^{2} + (y-y_{1})^{2}} \right]$$

$$\times \left\{ -(3+\nu) + 2(1+\nu) \frac{(y-y_{1})^{2}}{(x-x_{1})^{2} + (y-y_{1})^{2}} \right\} + \frac{(x-x_{1})}{(x-x_{1})^{2} + (y-y_{2})^{2}}$$

$$\times \left\{ -(3+\nu) + 2(1+\nu) \frac{(y-y_{2})^{2}}{(x-x_{1})^{2} + (y-y_{2})^{2}} \right\} - \frac{(x-x_{2})}{(x-x_{2})^{2} + (y-y_{1})^{2}}$$

$$\times \left\{ -(3+\nu) + 2(1+\nu) \frac{(y-y_{1})^{2}}{(x-x_{2})^{2} + (y-y_{1})^{2}} \right\} - \frac{(x-x_{2})}{(x-x_{2})^{2} + (y-y_{2})^{2}}$$

$$\times \left\{ -(3+\nu) + 2(1+\nu) \frac{(y-y_{2})^{2}}{(x-x_{2})^{2} + (y-y_{2})^{2}} \right\} \right] d\xi$$

$$(5.3)$$

where  $x_1, x_2, y_1, \text{ and } y_2 \text{ are given by}$ 

$$\begin{array}{rcl} x_1 & = & x_0 + \xi \\ x_2 & = & x_0 - \xi \\ y_1 & = & y_0 + d_f/2 \\ y_2 & = & y_0 - d_f/2 \end{array}$$

For convenience only the stress in the x-direction due to the interfacial shear stress is shown here, since the others are analoguous. The expressions for the remaining components can be found in appendix A. After carrying out the integrations the stress field in the matrix material due to the presence of the fibre is obtained. The stresses in the matrix material due to the applied load, the interfacial shear stress and the transverse normal tractions are denoted as  $\sigma_{ij}^{(1)}$ ,  $\sigma_{ij}^{(2)}$  and  $\sigma_{ij}^{(3)}$ , respectively.

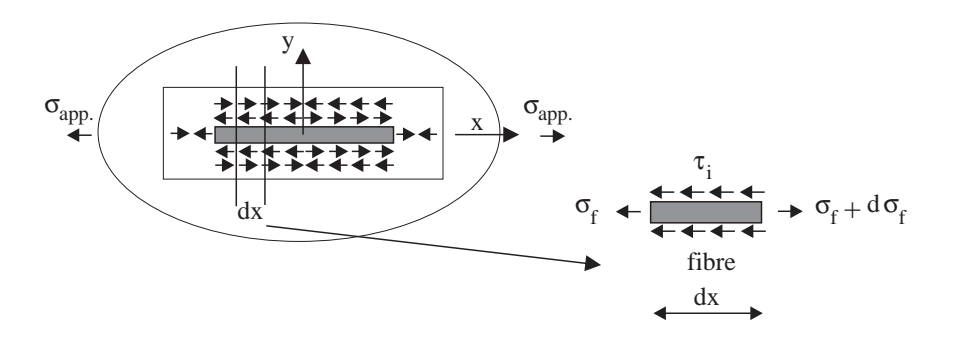


Figure 5.2: The free body diagram of the fibre.

The interfacial shear stress excerted on the fibre is obtained by equilibrating forces as shown in figure 5.2 and the equilibrium equation for the fibre becomes

$$d_f \frac{d\sigma_f(x)}{dx} - 4\tau_{xy}^*(x) = 0 (5.4)$$

where  $d_f$  is the fibre diameter.

Expressing the fibre stress  $\sigma_f$  as  $E_f^l \varepsilon_f$  the interfacial shear stress can be stated as

$$\tau_{xy}^*(x) = \frac{d_f E_f^l}{4} \frac{d\varepsilon_f}{dx} \tag{5.5}$$

where  $\varepsilon_f$  is the fibre strain obtained from experiments.

In some situations the fibre strain distribution may be linear. This linear distribution may occur when interfacial debonding is present, [43], if the load transfer mechanism is governed by friction, [48], [53] or if shear yielding occurs, [49]. In the previous chapter it was shown that the load transfer mechanism in the PP-U model composites is governed by the initial residual stress and the coefficient of friction. This friction is assumed to be Coulomb friction and thus the following relation is assumed to be valid

$$\tau_{xy}^*(x) = -\mu_{fric}\sigma_y^*(x) \tag{5.6}$$

where  $\mu_{fric}$  is the coefficient of friction.

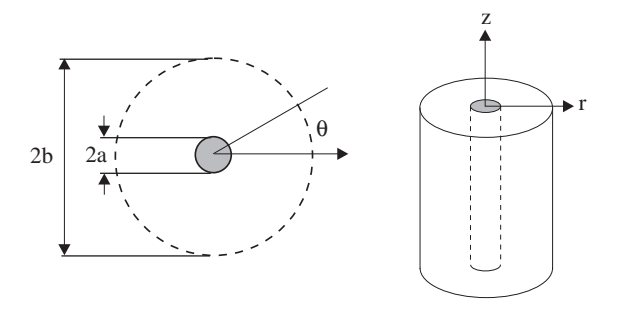


Figure 5.3: Coaxial cylinders used in the Lamé solution.

The initial transverse traction is a radial pressure due to manufacture of the specimen and can be obtained from the Lamé solution, see e.g. [12]. The Lamé solution is obtained by assuming that the fibre and matrix can be modelled as two coaxial cylinders with radii a and b, respectively, figure 5.3.

Assuming a displacement field of the form

$$u_r = f(r) \qquad u_\theta = 0 \qquad u_z = C_0 z \tag{5.7}$$

where  $u_{\theta} = 0$  due to symmetry. Inserting the assumed displacement field into the only non-vanishing equilibrium equation (the remaining equilibrium equations are identically satisfied due to rotational symmetry and due to the infinite length of the fibre/matrix cylinder)

$$\frac{\partial \sigma_r}{\partial r} + \frac{\sigma_r - \sigma_\theta}{r} = 0 \tag{5.8}$$

gives a second order differential equation of the form

$$\frac{\partial^2 u_r}{\partial r^2} + \frac{1}{r} \frac{\partial u_r}{\partial r} - \frac{u_r}{r^2} = 0 \tag{5.9}$$

which is solved subject to the following conditions

- Radial stresses in the matrix are zero at r = b, i.e.  $\sigma_r^m(b) = 0$ .
- Continuity of stress at the interface, i.e.  $\sigma_r^f(a) = \sigma_r^m(a)$ .
- Equilibrium of forces at the composite cylinder cross section,  $\sigma_z^f A_f + \sigma_z^m A_m = 0$ .

The radial stress in the matrix is then obtained as

$$\sigma_r^m = \frac{k_4(\alpha_m - \alpha_f^l) + k_2(\alpha_f^t - \alpha_m)}{k_1 k_4 - k_2 k_3} \left(1 - \frac{b^2}{r^2}\right) \Delta T$$
 (5.10)

where the constants  $k_i$  are given by

$$k_{1} = 2\left(\frac{\nu_{m}}{E_{m}} + \frac{\nu_{f}^{l}}{E_{f}^{l}} \frac{1 - \xi}{\xi}\right)$$

$$k_{2} = -\left(\frac{1}{E_{m}} + \frac{1}{E_{f}^{l}} \frac{1 - \xi}{\xi}\right)$$

$$k_{3} = -\frac{1 - \nu_{m}}{E_{m}} - \frac{1 + \nu_{m}}{E_{m}} \frac{1}{\xi} - \frac{1 - \nu_{f}^{t}}{E_{f}^{t}} \frac{1 - \xi}{\xi}$$

$$k_{4} = \frac{\nu_{m}}{E_{m}} + \frac{\nu_{f}^{l}}{E_{f}^{l}} \frac{1 - \xi}{\xi}$$

where  $E_m$  and  $\nu_m$  are Young's modulus and Poisson ratio of the matrix respectively.  $\alpha_m$ ,  $\alpha_f^l$ ,  $\alpha_f^t$  are coefficients of thermal expansion in the longitudinal and the transverse direction of the fibre respectively.  $E_f^l$  and  $E_f^t$  are Young's moduli of the fibre in the longitudinal and transverse direction respectively.  $\nu_f^l$  and  $\nu_f^t$  are the Poisson ratios in the longitudinal and transverse direction respectively.  $\xi$  is the ratio of the squared diameters of the fibre and matrix, respectively and given as  $\xi = a^2/b^2$ .  $\Delta T$  equals the difference between the crystallisation temperature and ambient temperature. For cooling rates of  $\approx 100$  °C/min, DSC measurements have shown that the crystallisation temperature is  $\approx 103$  °C [73]. Combining equations (5.5), (5.6) and (5.10) the coefficient of friction is found to be  $\mu_{fric} = 0.21$ . The resulting stresses in the matrix material are now obtained by a simple superposition of the three contributions,  $\sigma_{ij}^{(1)}$ ,  $\sigma_{ij}^{(2)}$  and  $\sigma_{ij}^{(3)}$ . These stresses and the appropriate time are inserted into the constitutive law of the matrix material, equation (3.31), and then the matrix creep strains can be found.

# 5.2 Creep Modelling, Approach II

In this section a theoretical approach is described from which the stress and strain in the matrix material can be obtained at any desired time. This approach is an extension of the method just shown and results from this approach can also be found in the papers by Schjødt-Thomsen and Pyrz [105] and [106].

The approach is inspired by a paper by Argon [2]. On the basis of Eshelby's thought experiment the elastic stress and strain in a composite consisting of one short fibre embedded in an infinite matrix are calculated. The fibre and matrix are linearly elastic isotropic and assumed to have identical Poisson's ratios and only load applied parallel to the fibre axis is considered.

In the present analysis the stress and strain during creep are calculated using Eshelby's thought experiment and an incremental stress/strain formulation of the Schapery model. Furthermore, off - axis loading, different Poisson's ratios, transversely isotropic fibres as well as thermal effects are considered.

An exact solution to the problem of a cylindrical fibre of finite length embedded in an infinite matrix is very difficult to obtain but a usefull and reasonably accurate solution is obtainable by means of Eshelby's thought experiment. Eshelby originally used this approach to model the stress/strain field due to martensitic formation in metals. He solved the problem in the following elegant way.

Cut the inclusion from its surrounding matrix. Allow the inclusion to transform. Apply surface tractions which restore the inclusion to its original form, put it back in the matrix and rejoin the material across the cut. The stress is now zero in the matrix and has a known constant value in the inclusion. The applied surface tractions have become built in as a layer of body force spread over the interface between the inclusion and matrix. To complete the solution this unwanted layer is removed by applying an equal and opposite layer of body force. The additional elastic field thus introduced is found by integration from the expression for the elastic field of a pointforce, [24].

This approach gives the initial elastic stresses in the matrix. Inserting the initial stresses into the three dimensional constitutive law of the matrix, equation (3.31), gives the initial elastic strains. These strains give rise to stress relaxation during a small amount of time, dt. The stress relaxation during time dt creates a new state of stress which is used to calculate the strains for the next time increment etc.

A transversely isotropic fibre of length  $l_f$  and diameter  $d_f$  is embedded in an infinite initially elastic matrix with Youngs modulus  $E_m$  and Poisson's ratio  $\nu_m$ . The system is subjected to tensile stresses  $\sigma_{IJ}^{\infty}$  at the remote boundary. If the fibre is misaligned with respect to the loading axis the applied stress is transformed into the fibre co-ordinate system through equation (5.1), thus  $\sigma_x^{\infty}$ ,  $\sigma_y^{\infty}$  and the interfacial shear stress can be determined.

To find the initial stress in the matrix the fibre is removed from the infinitely extended matrix and replaced by matrix material.  $\sigma_x^{\infty}$ ,  $\sigma_y^{\infty}$  and a temperature change,  $\Delta T$ , are applied, causing strains  $\varepsilon_x^{\infty}$  and  $\varepsilon_y^{\infty}$ . The matrix material occupying the position of the fibre is removed and surface tractions,  $\sigma_x^{\infty}$  and  $\sigma_y^{\infty}$  are placed along the boundary of the "hole", as shown in figure 5.4A.

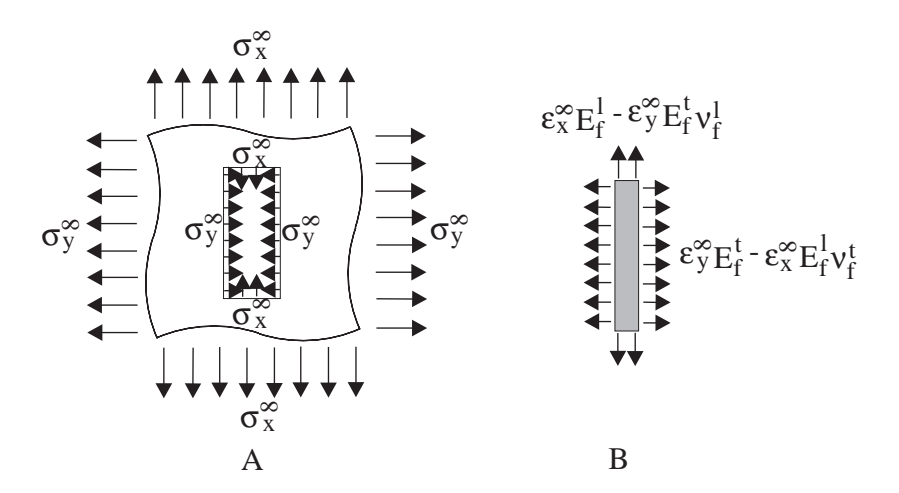


Figure 5.4: Tractions A) on the matrix and B) on the fibre.

Tractions of magnitude  $\varepsilon_x^{\infty} E_f^l$  are applied to the ends of the fibre and  $\varepsilon_y^{\infty} E_f^t$  are applied to the sides of the fibre in order to make it fit perfectly into the deformed hole of the matrix. The traction applied to the end of the fibre causes additionally transverse stresses of magnitude  $-\nu_f^t \varepsilon_x^{\infty} E_f^l$ . Furthermore the transverse traction,  $\varepsilon_y^{\infty} E_f^t$ , causes a longitudinal stress of magnitude  $-\varepsilon_y^{\infty} E_f^t \nu_f^l$ , figure 5.4B. The additional longitudinal stress will make yet another contribution to the transverse stress but this is neglected since it contains higher order terms of the Poisson's ratios, such

as  $\nu_m \nu_f^l$ .

The interfacial tractions in the composite when the fibre is put back into the matrix are now readily obtained as

$$\sigma_x^* = -\sigma_x^{\infty} + \frac{\sigma_x^{\infty}}{E_m} E_f^l - \frac{\sigma_y^{\infty}}{E_m} E_f^t \nu_f^l + \alpha_m \Delta T (E_f^t \nu_l - E_f^l)$$

$$\sigma_y^* = -\sigma_y^{\infty} + \frac{\sigma_y^{\infty}}{E_m} E_f^t - \frac{\sigma_x^{\infty}}{E_m} E_f^l \nu_f^t + \alpha_m \Delta T (E_f^t - E_f^l \nu_t)$$
(5.11)

In this equation the only thermal contributions are due to the matrix. The contributions from the fibre are neglected since  $\alpha_m \gg \alpha_f$ .

If the tractions in equation (5.11) are used as they are and applied directly to the matrix at the interface they will cause an incompatible displacement field. So in order to ensure compatibility and to determine the interfacial forces to be integrated along the fibre boundary it is necessary to determine the fraction of force which is carried by the fibre and matrix, respectively. This is done by combining the stress-strain relations and the strain-displacement relations as

$$\frac{\partial u_x}{\partial x} = \frac{1}{E'_m} \left( \sigma_x - \nu'_m \sigma_y \right) \qquad \frac{\partial u_y}{\partial y} = \frac{1}{E'_m} \left( \sigma_y - \nu'_m \sigma_x \right)$$
 (5.12)

where  $E'_m$  and  $\nu'_m$  depends on whether the deformation state is plane stress or plane strain and are given by

$$E'_m = \begin{cases} E_m & plane stress \\ \frac{E_m}{1-\nu_m^2} & plane strain \end{cases}$$
 $\nu'_m = \begin{cases} \nu_m & plane stress \\ \frac{\nu_m}{1-\nu_m} & plane strain \end{cases}$ 

where the plane strain assumption is used in this approach.

Both  $u_x$  and  $u_y$  consist of two contributions; one from the longitudinal interfacial tractions and one from the transverse interfacial tractions. The stresses in the matrix material due to these tractions are obtained by rewriting equations (5.2) as

$$\sigma_{x}(x,y) = \frac{P_{x}}{4\pi} \left\{ \left( \frac{(x+l_{f}/2)}{(x+l_{f}/2)^{2} + (y)^{2}} \right) \left( -(3+\nu) + 2(1+\nu) \frac{(y)^{2}}{(x+l_{f}/2)^{2} + (y)^{2}} \right) \right.$$

$$\left. - \left( \frac{(x-l_{f}/2)}{(x-l_{f}/2)^{2} + (y)^{2}} \right) \left( -(3+\nu) + 2(1+\nu) \frac{(y)^{2}}{(x-l_{f}/2)^{2} + (y)^{2}} \right) \right\}$$

$$\sigma_{y}(x,y) = \frac{P_{x}}{4\pi} \left\{ \left( \frac{(x+l_{f}/2)}{(x+l_{f}/2)^{2} + (y)^{2}} \right) \left( (1-\nu) - 2(1+\nu) \frac{(y)^{2}}{(x+l_{f}/2)^{2} + (y)^{2}} \right) \right.$$

$$\left. - \left( \frac{(x-l_{f}/2)}{(x-l_{f}/2)^{2} + (y)^{2}} \right) \left( (1-\nu) - 2(1+\nu) \frac{(y)^{2}}{(x-l_{f}/2)^{2} + (y)^{2}} \right) \right\}$$

$$\sigma_{x}(x,y) = \frac{P_{y}}{4\pi} \left\{ \left( \frac{(y+d_{f}/2)}{(x)^{2} + (y+d_{f}/2)^{2}} \right) \left( (1-\nu) - 2(1+\nu) \frac{(x)^{2}}{(x)^{2} + (y+d_{f}/2)^{2}} \right) \right.$$

$$\left. - \left( \frac{(y-d_{f}/2)}{(x)^{2} + (y-d_{f}/2)^{2}} \right) \left( (1-\nu) - 2(1+\nu) \frac{(x)^{2}}{(x)^{2} + (y+d_{f}/2)^{2}} \right) \right\}$$

$$\sigma_y(x,y) = \frac{P_y}{4\pi} \left\{ \left( \frac{(y+d_f/2)}{(x)^2 + (y+d_f/2)^2} \right) \left( -(3+\nu) + 2(1+\nu) \frac{(x)^2}{(x)^2 + (y+d_f/2)^2} \right) - \left( \frac{(y-d_f/2)}{(x)^2 + (y-d_f/2)^2} \right) \left( -(3+\nu) + 2(1+\nu) \frac{(x)^2}{(x)^2 + (y-d_f/2)^2} \right) \right\}$$

which correspond to the stresses in an infinite plane due to a point force in the x-direction at  $(x, y) = (\pm l_f/2, 0)$  and a point force in the y-direction at  $(x, y) = (0, \pm d_f/2)$ , respectively. Now  $u_x$  and  $u_y$  are readily found by inserting these stresses into the stress-displacement relations given in equations (5.12). The displacements are now obtained as functions of both x and y as

$$u_x = f(x, y) + h(y)$$
  $u_y = g(x, y) + q(x)$  (5.14)

where h(y) and q(x) are arbitrary functions due to the integration. h(y) and q(x) need to be zero in order to keep  $u_x$  and  $u_y$  symmetric about x = 0 and y = 0, respectively.

The displacements  $u_x$  and  $u_y$  are singular for  $(x, y) = (\pm l_f/2, 0)$  and  $(x, y) = (0, \pm d_f/2)$ . To determine the fraction of force carried by the fibre and the matrix it is necessary to define average displacements across the fibre end,  $\langle u_x \rangle$ , and along the sides of the fibre,  $\langle u_y \rangle$ , as

$$\langle u_x \rangle = \frac{2}{d_f} \int_0^{d_f/2} u_x dy$$
  
 $\langle u_y \rangle = \frac{2}{l_f} \int_0^{l_f/2} u_y dx$ 

These average displacements are non-singular at  $x = \pm l_f/2$  and  $y = \pm d_f/2$ .  $\langle u_i \rangle$  are of the form

$$\langle u_i \rangle = \pm \frac{P}{8\pi E_m d_f} \left\{ f(\nu_m, d_f, l_f), \tan^{-1}(d_f, l_f) \right\}$$
 (5.15)

 $\langle u_x \rangle$  and  $\langle u_y \rangle$  gives the average displacements due to a force P and can be rearranged to give the displacement due to a unit force dP. The relation between the displacements  $\langle u_x \rangle$  and  $\langle u_y \rangle$  and the unit force dP can be thought of as being the stiffness of the infinite medium in the x- and y-direction, respectively. These stiffnesses are obtained as

$$K_x^m = \frac{dP}{d\langle u_x \rangle} \qquad K_y^m = \frac{dP}{d\langle u_y \rangle} \tag{5.16}$$

The stiffnesses of the fibre in the x- and y-direction are calculated as

$$K_x^f = \frac{d_f E_f^l}{l_f} \qquad K_y^f = \frac{l_f E_f^t}{d_f} \tag{5.17}$$

Now the stiffnesses of the matrix and the fibre are used to determine the fraction of the interfacial force carried by the fibre and matrix, respectively. The fraction of the force carried by the matrix in the x- and y-direction are denoted as  $\Delta P_y^m$  and  $\Delta P_y^m$  and are determined as

$$\Delta P_i^m = K_i^m \Delta u_i$$

where  $\Delta u_i$  are given as

$$\Delta u_x = -\frac{\sigma_x^* d_f}{K_x^m + K_x^f} \qquad \Delta u_y = -\frac{\sigma_y^* l_f}{K_y^m + K_y^f}$$
 (5.18)

The final interfacial tractions to be integrated along the fibre boundary are now found to be

$$\sigma_x^{int.} = -\frac{\sigma_x^* K_x^m}{K_x^m + K_x^f} \qquad \sigma_y^{int.} = -\frac{\sigma_y^* K_y^m}{K_y^m + K_y^f}$$
 (5.19)

If the fibre is misaligned the interfacial shear stress is found using equation 5.1, inserted into the first of equation 5.19 replacing  $\sigma_x^*$  and finally integrated using the expressions in appendix A.

#### **Creep Strains**

The disturbed stress field is obtained by integrating the tractions along the fibre boundary and inserting the resulting matrix stresses into the three dimensional constitutive law of the matrix for t = 0, thus giving the initial elastic strain disturbance. This strain causes stress relaxation during a time step dt, resulting in a new state of stress  $\sigma_{ij} + d\sigma_{ij}$  to be used in the next time increment together with t = dt, causing a new state of strain which again causes stress relaxation and so on. This is repeated until t is equal to the desired time of duration.

In order to do that the incremental stresses and strains are needed. The incremental strains are found by differentiating equation (3.31) and are given as

$$d\varepsilon_{ij}(t) = \{(1+\nu_m)\sigma_{ij} - \nu_m \sigma_{kk}\delta_{ij}\} \frac{\partial \tilde{D}(t)}{\partial t} dt$$
(5.20)

where it is assumed that the stresses are constant during the time increment dt. The time varying stresses are obtained in the same manner as

$$d\sigma_{ij}(t) = \frac{1}{1 + \nu_m} \left\{ \varepsilon_{ij} + \frac{\nu_m}{1 - 2\nu_m} \delta_{ij} \varepsilon_{kk} \right\} \frac{\partial E(t)}{\partial t} dt$$
 (5.21)

where it is assumed that the strains are constant during the time increment.

To calculate the creep strains around the fibre the following procedure is now applied:

- 1. Calculate the initial matrix stresses,  $\sigma^0_{ij}$ , from the tractions.
- 2. Insert the initial stresses into equation (3.31) together with time, t = 0, thus giving the initial elastic strains,  $\varepsilon_{ij}^0$ .
- 3. Insert the initial strains into equation (5.21), thus giving  $d\sigma_{ij}(t)$ .
- 4.  $\sigma_{ij}(t) = \sigma_{ij}^0 + d\sigma_{ij}(t)$ .
- 5. Insert  $\sigma_{ij}(t)$  and the appropriate time into equation (5.20), thus giving the incremental strain,  $d\varepsilon_{ij}(t)$ .
- 6.  $\varepsilon_{ij}(t) = \varepsilon_{ij}^0 + d\varepsilon_{ij}(t)$ .

- 7. Insert the "new" strain  $\varepsilon_{ii}(t)$  and appropriate time into equation (5.21).
- 8. Repeat step 3 to 7 until t equals the desired time.
- 9. Add the farfield stress and strain to obtain the complete solution.

### 5.3 Finite Element Analysis

Nonlinear finite element models are considered in this section. Only models with fibres aligned along the loading direction are analysed by FEM, in order to treat the models axisymmetrically. The program used is the commercial FE program, COSMOS/M.

The main purpose of the FE - analysis is to do further checking of the frictional load transfer assumption and the apparent yielding in the interface between the fibre and matrix.

Finite element analysis combined with Raman spectroscopy has not been widely used in spite of the fact that this is a suitable combination for investigating the complex stress/strain state surrounding the fibres in short fibre reinforced composites.

Although some investigations have dealt with FEM, it seems that the effects of both nonlinearity and thermal history are neglected in these analysis.

Fan and Hsu [25] investigated the effect of fibre end shapes on load transfer efficiency in the linear elastic case. They found that a blunt end would cause much higher stresses in the vicinity of the fibre than a tapered end, which might lead to premature failure, whereas fibres with tapered ends enhance the load transfer efficiency due to the constant level of stress in the fibre. A good agreement is found between FE analysis and Raman experiments, for both kind of fibre ends.

Guild et al. [37] investigated the stress transfer in model composites by both Raman spectroscopy and FEM. The FE model incorporates the effect of matrix plasticity. It is concluded that plasticity has a pronounced effect on the load transfer. Two fibre geometries are considered. One with a rounded end and one with sharp corners at the end. Comparison between Raman measurements and these two geometries show generally good agreement but since the Raman results differs from the FE results in the case of sharp fibre corners, the authors conclude that this fibre geometry should not be used in the FE models since on a molecular level all corners are rounded.

Schaffer and Adams [98] used the nonlinear single-integral constitutive equations developed by Schapery in their FE analysis of a unidirectional composite subjected to transverse loading. They found a good agreement with experimental results in the case of uniaxial loading.

The present analysis differs from those mentioned above because the effect of thermal residual strains and stresses on subsequent creep strains are accounted for in the FE model. Furthermore, matrix plasticity and frictional load transfer at the interface is considered.

#### The FE Models

The models are considered as being axi-symmetric and thus only one quarter of the cross section of the model is considered. The models considering the PP-U model composites have outer diameters of 80  $\mu$ m, whereas the models considering the PP-MA model composites have outer

diameters of 130  $\mu$ m. The diameters corresponds to twice the thickness of the polypropylene films.

The finite element meshes used for the PP-U and PP-MA model composites are shown in figures 5.5A and 5.5B, respectively. The fibre is modelled as being transversely isotropic. The fibre diameters for the plasma treated fibre and the standard surface treated fibre were measured in the previous chapter and were found to be 6.1  $\mu$ m and 6.7  $\mu$ m, respectively. The fibre diameter in the FE models are taken to be the same in each case at 6.5  $\mu$ m. The fibre length modelled in both cases corresponds to the mean fibre length, i.e. 740  $\mu$ m and 450  $\mu$ m, respectively.

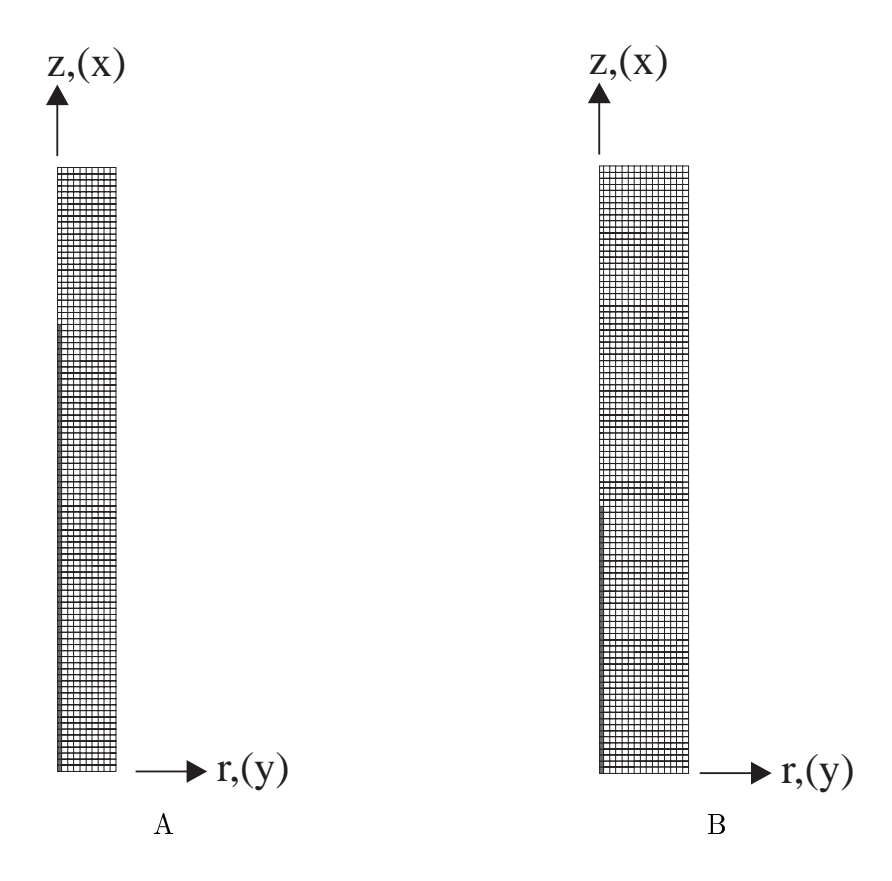


Figure 5.5: The FE mesh used for A) the PP-U model composites and B) the PP-MA model composites. Letters in parenthesis corresponds to the directions used in the theoretical approaches.

The elements used in the analysis are 4 and 8 node isoparametric elements. In the mesh used for the PP-MA FE models, figure 5.5B, there are in fact 4 times as many elements as shown. However, a figure with the correct number of elements is nearly totally black and is therefore not shown. Using this small element size enables the plotting of matrix field quantities at a radial distance of 1  $\mu$ m from the fibre surface. In the PP-U FE models the interfacial quantities are plotted along the fibre matrix boundary, because in this situation the material properties are not "mixed" along the fibre/matrix interface.

#### Thermal loading

To incorporate the effect of thermal history upon subsequent loading it is necessary to simu-

late the cooling process of the material. This is done by subjecting all the nodes in the model to a uniform temperature of  $103~^{\circ}$ C at the beginning of the analysis. The model is then cooled down to  $20~^{\circ}$ C in 0.01 hour. The response of the model to subsequent loading will now depend on the thermal history.

To apply the thermal and mechanical loading histories, "time-temperature curves" are defined. The FE model is then subjected to loading histories corresponding to these time-temperature curves. The time-temperature curve for the cooling procedure and subsequent creep loading is shown in figure 5.6.

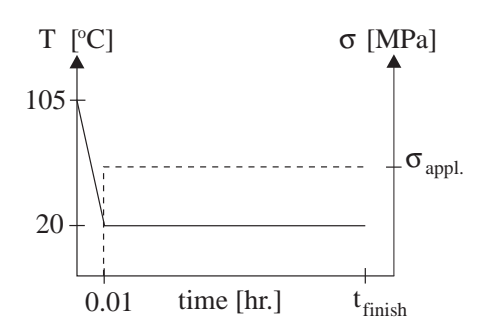


Figure 5.6: The "time-temperature curves" defining the thermal and mechanical loadings in the FE program.

The effect of temperature on Young's modulus of the matrix material is accounted for by defining a "temperature-property" curve, which is analogous to the time-temperature curves. Young's modulus as a function of temperature is shown in figure 5.7. The data has been provided by BASF.

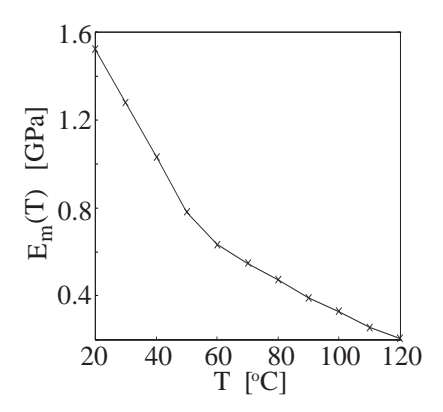


Figure 5.7: Variation of Young's modulus with temperature.

The FE program interpolates linearly between the defined points to determine the value of Young's modulus at a certain temperature.

During the cooling process the coefficients of thermal expansion are assumed to be independent of temperature.

#### Creep constitutive law

The creep modelling in the FE program is based upon a classical power law for creep, the Bailey - Norton law, which describes the uniaxial creep strain as a function of the uniaxial stress, time and temperature and is expressed as

$$\varepsilon^{c} = C_{0} \sigma^{C_{1}} t^{C_{2}} e^{\left(\frac{-C_{T}}{T + T_{ref}}\right)}$$
(5.22)

where  $C_1 > 0$ ,  $0 < C_2 < 1$ , T is temperature,  $T_{ref}$  is a stress free temperature and  $C_T$  is a material constant defining the creep-temperature dependency.

This creep law represents both the transient and the steady creep regime, but does *not* take into account the elastic response which must be considered when the constants are determined from experimental data.

In order to extend this law to multiaxial behaviour the following assumptions are made [110]:

- The uniaxial creep law remains valid if the uniaxial creep strain and the uniaxial stress are replaced by their effective values.
- Material is isotropic, i.e. stresses and strains are independent of orientation.
- The creep strains are incompressible, i.e.  $e_{ij}^c = \varepsilon_{ij}^c$

The third assumption enables the use of the Von-Mises flow rule

$$\dot{\varepsilon}_{ij}^c = \frac{\sqrt{K_2}}{\sqrt{J_2}} s_{ij} \tag{5.23}$$

where  $K_2$  and  $J_2$  are the second invariants of  $\dot{e}_{ij}^c$ ,  $(K_2 = \frac{1}{2}\dot{e}_{ij}^c\dot{e}_{ij}^c)$  and the deviatoric stress  $s_{ij}$   $(J_2 = \frac{1}{2}s_{ij}s_{ij})$ , respectively. This simplifies the numerical solution procedure and is also the reason why creep is sometimes called "rate dependent plasticity".

Due to the simplicity of the creep constitutive model and the fact that polypropylene is highly nonlinear it is necessary to use different values of the parameters for each load case. This means that  $C_1$  in the Bailey - Norton creep law changes slightly as a function of stress, from being 1 at  $\sigma = 1$  MPa to 1.2128 at  $\sigma = 8$  MPa. The experimental data along with the Bailey - Norton law is shown in figure 5.8

#### **Frictional Elements**

As shown earlier the fibre strain in the PP-U composites show a linear dependence on the axial coordinate and it has been concluded that the load transfer is governed by friction.

To model frictional phenomena "node-to-node" gap elements are specified along the boundary between the fibre and the matrix.

Two node gap elements are used in contact problems when two bodies are coming in contact with each other due to the application of external forces. The main assumption in the modelling of this type of element is that the direction of the normal force and the contact points are known in advance and remain unchanged during the analysis. The two node gap elements are placed between two nodes of the contacting bodies (one node on each body) such that the direction of

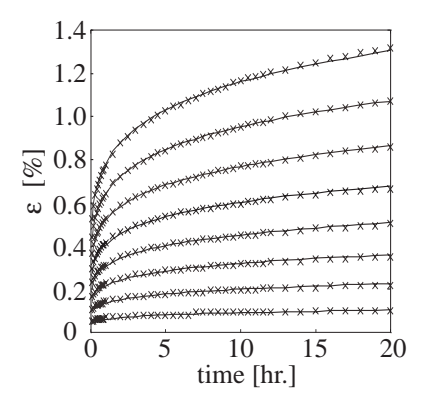


Figure 5.8: The experimental data along with the Bailey - Norton creep law.

the gap element - represented by a straight line joining the initial locations of its two nodes - coincides with the direction of the normal contact force, see figure 5.9. Depending on the type of contact problems the gap element can be specified to be either a compressive gap (limiting the relative contraction between nodes) or a tensile gap (limiting the relative expansion between nodes). Friction can then be considered using compressive gap elements, [110].

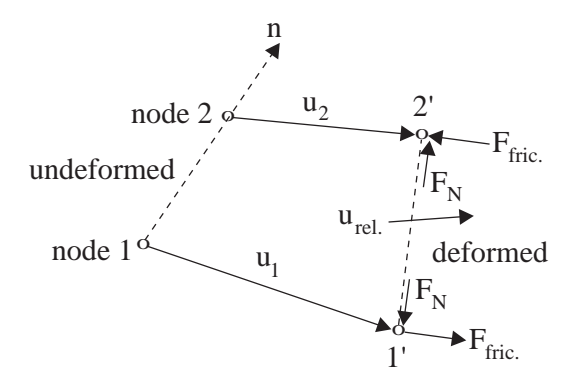


Figure 5.9: Two-node gap element.

In the present models the part of the fibre which is in contact with the matrix material is defined as the "contact surface" and the matrix is defined as the "contactor body". The nodes of the gap are now allowed to move relative to each other until contact between the fibre and matrix is established. After contact the nodes can not penetrate into the fibre and a friction force is developed due to the normal force. Care must be taken when defining the gap elements because a wrong orientation of the elements will cause the fibre to be penetrateable for the nodes.

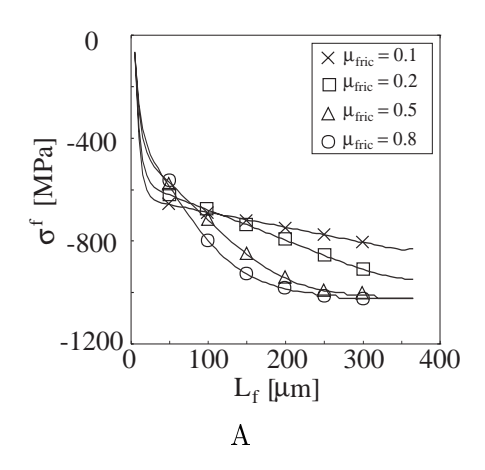
# 5.4 Results from Approaches I, II and FEM

In this section some selected results from experiments are compared to results obtained from both the two theoretical approaches and FEM.

When the interface is "strong" as in the PP-MA model composites, approach II is used. When the interface is weaker and the load transfer is of a frictional character, as in the PP-U model composites, approach I is used.

Calculations have been conducted in order to investigate the influence of the magnitude of the coefficient of friction on the stress profile in the fibre.

Figure 5.10A shows the longitudinal thermal residual stresses in the fibre as a function of the coefficient of friction. It is seen from the calculations that for low values of  $\mu_{fric}$  the end effect is more pronounced and contributes more to the magnitude of the fibre stress. For values of  $\mu_{fric}$  of 0.5 and 0.8 the fibre stress shows a pronounced nonlinearity with respect to the longitudinal coordinate. For even larger values of  $\mu_{fric}$  there is virtually no difference in the stress profile compared to the perfectly bonded case, figure 5.10B. This implies that it is very difficult to determine if the load transfer is frictional or due to an adhesive bond just from the shape of the strain profile obtained from the MRS measurements.



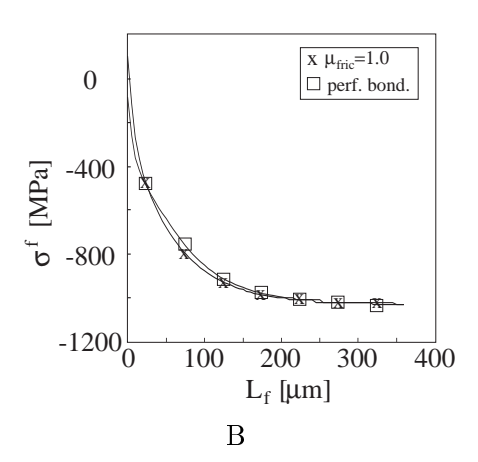


Figure 5.10: A) The thermal residual fibre stress for various values of  $\mu_{fric}$ . B) The thermal residual fibre stress in the perfect bonded case and in case of a large value of  $\mu_{fric}$ .

In figure 5.11 the thermal residual fibre stresses from a cooling analysis with Coulomb friction acting at the interface is shown along with the mean value obtained from the Raman experiments and a good agreement between the FEM values and the experimental values is obtained. This good agreement between experiments and modelling verifies the assumption that the load is transferred by friction. It is also apparent from the figure that the zone of influence from the fibre end is very small, corresponding to a distance of approximately 4 fibre diameters. However, as mentioned before the end effect contributes significantly to the magnitude of the fibre stress.

In figure 5.12 the calculated longitudinal fibre stress is shown along with the measured fibre stress. From the figure it is seen that even though the zone of influence of the fibre end is small it has a large effect on the fibre stress level. This is also the reason for the discrepancy between the experimental values and the calculated values. The experimentally determined fibre stress is lower than the fibre stress from FEM. The reason is that the fibre end is believed to debond on the application of load, whereas the fibre is perfectly bonded to the matrix in the FE model. However, the linearity of the stress approximately 20  $\mu$ m away from the fibre end shows a slope very close to that of the experimental stress, which again verifies the frictional load transfer mechanism.

In figure 5.13 the interfacial shear stress along with the radial stress are shown. In conjunction with the use of the Lamé solution it is assumed - for the fibre lengths considered here - that the

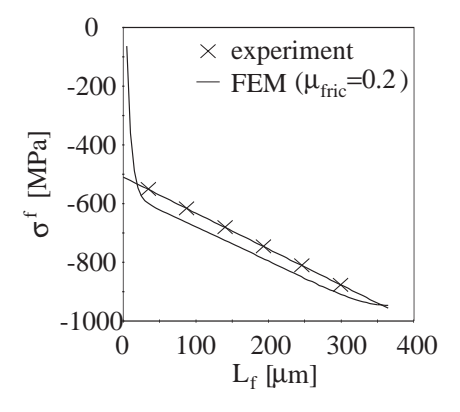


Figure 5.11: The initial residual fibre stress from experiments and FEM.

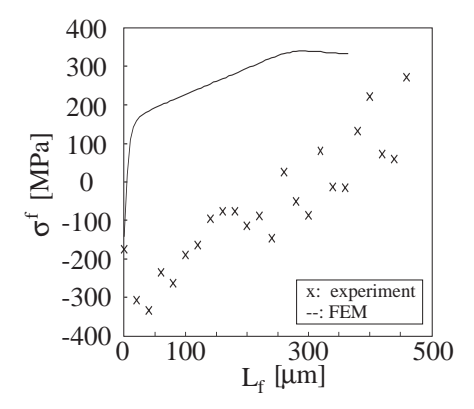


Figure 5.12: The fibre stress from experiments and FEM after 3 hours of creep at 7 MPa.

interfacial shear stress and the radial pressure on the fibre are constant along the fibre length. That this is a quite accurate assumption can be seen from the figure. The two stress components deviate from being constant only along the first 25  $\mu$ m, corresponding to 3-4 fibre diameters.

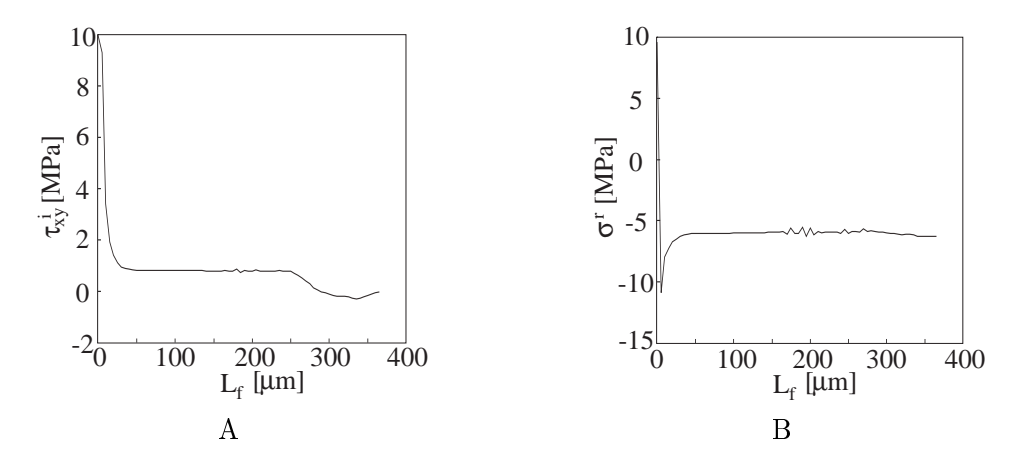
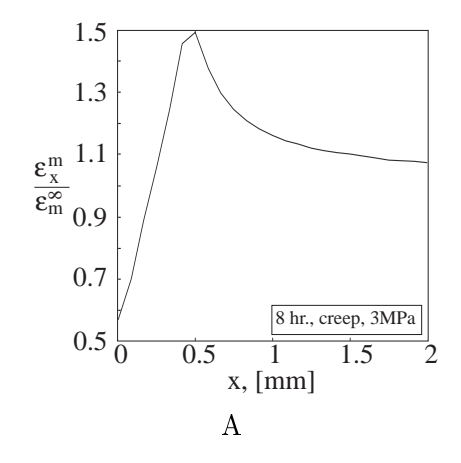


Figure 5.13: A) Interfacial shear stress and B) the radial stress after 3 hours creep at 7 MPa.

Figures 5.14A and 5.14B show the creep strain in the direction of the fibre for two load cases corresponding to 3 MPa and 7 MPa, respectively applied to the PP-U composites. The results

are obtained using approach I. The interfacial shear stresses in the two situations are 0.9 MPa and 2.7 MPa, and calculated from the data in figure 4.8.



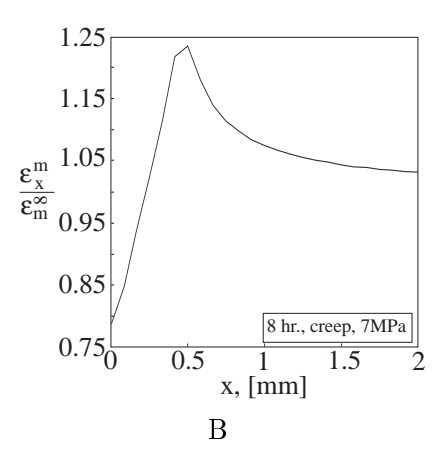


Figure 5.14: Matrix creep strain adjacent to the fibre after 8 hours creep at A) 3 MPa and B) 7 MPa.

The fibre is situated with its centre point at the origin of the coordinate system and the fibre end is at 0.45 mm. The fibre has a restraining effect on the strain along approximately 220  $\mu$ m of the fibre, but the relatively large strains at the end of the fibre suggest that stress relaxation will occur. The stress relaxation in the matrix will cause the fibre to carry more load - provided that the interface is perfect. Thus, stress relaxation will cause a load redistribution and the fibre will either carry more or less load as time and/or load increases, depending on the interfacial quality.

It is clearly seen from figure 5.14B that stress relaxation has occurred at the end of the fibre, thus decreasing the strain concentration due to the poor adhesion between the fibre and matrix. If the interfacial bonding is strong the fibre strain will increase during creep, causing the interfacial shear stress to increase at the fibre ends - provided that no yielding occurs. This also means that the strain concentration at the fibre end will increase during creep. From figure 5.14B it is clearly seen that the strain is decreased, meaning that the ratio of fibre load to applied load is decreased. This suggests that for even longer loading times and/or larger levels of applied load the fibre will not be carrying any load and the composite will not perform as intended. That this is true have been shown in the previous chapter in figure 4.9, where the strains in the middle of the fibre are approximately constant, and close to zero.

The theoretical model, using Eshelby's thought experiment, have been used to calculate the fibre strains after 3 hours creep at three load levels corresponding to 1, 4 and 8 MPa. All the calculated values are shown for half the fibre length only, due to symmetry.

In Fig. 5.15B the measured fibre strains are shown. The embedded fibre has a length of 500  $\mu$ m. The residual strains are building up in a nearly linear manner until the middle of the fibre where the strain levels off. The magnitude of the measured fibre strain is close to the compressive fracture strain of the used carbon fibres. After 3 hours of creep at a load of 1 MPa, the measured fibre strains are nearly constant, but below zero. In Fig. 5.15A the calculated fibre strains are shown. Here, it is important to notice that the magnitudes of the calculated strains and the experimentally measured strains can not be compared directly because the calculations are based on a plane strain assumption. However, the tendencies are obvious. The calculated fibre strain

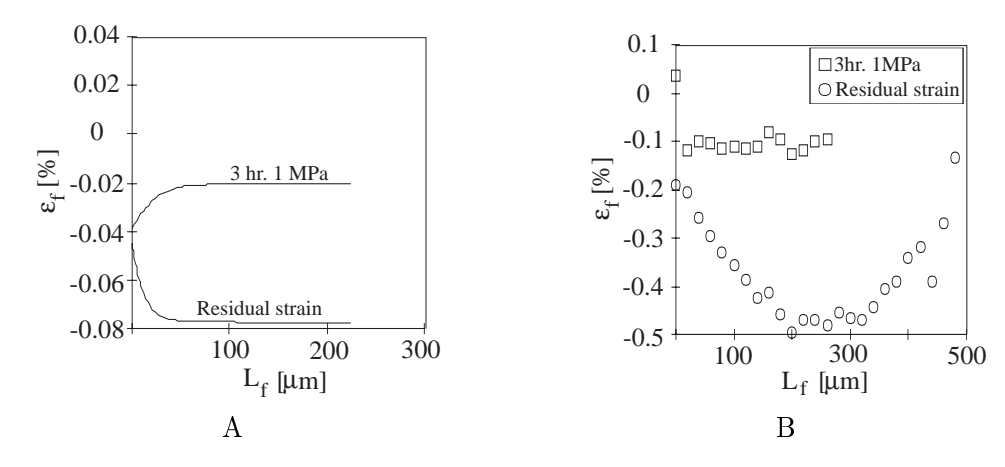


Figure 5.15: Fibre strain A) calculated and B) measured.

is also compressive after 3 hours of creep at 1 MPa load. The rate at which the fibre strains are building up is higher for the calculated fibre strain than for the measured fibre strain. This is due to the fact that the interfacial tractions are assumed to be constant. The constant interfacial tractions affect the interfacial shear stresses which are governing the shape of the fibre strain profile.

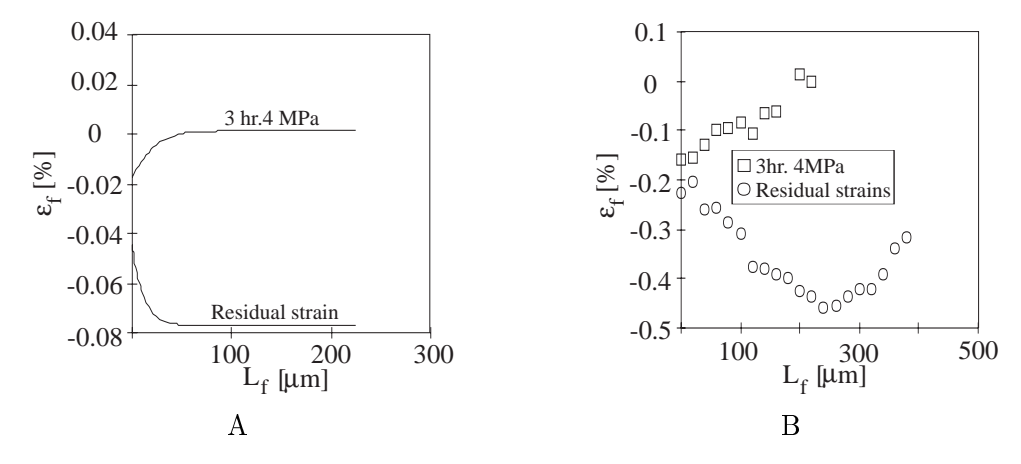
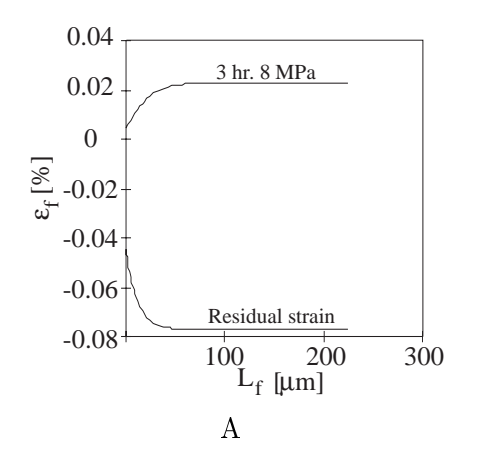


Figure 5.16: Fibre strain A) calculated and B) measured.

In Fig. 5.16B the measured fibre strains are shown. The embedded fibre has a length of 400  $\mu$ m. Again the residual fibre strain builds up linearly towards the middle of the fibre where it abruptly changes slope and decreases towards the other end of the fibre. The fibre strains after 3 hours of creep at 4 MPa is seen to increase in a slightly nonlinear manner but only reaches a maximum value of approximately zero in spite of the fact that the overall strain after 3 hours of creep is 0.64 %. In Fig. 5.16A the calculated fibre strains are shown. Again the characteristics of the experiment is displayed in the calculations. The fibre strain after 3 hours creep is just above zero. An interesting aspect to notice is that the model predicts both compression and tension in the fibre after 3 hours of loading.

In Fig. 5.17B the measured fibre strains are shown. The embedded fibre has a length of 350  $\mu$ m. The residual fibre strains are building up in a nearly linear manner and abruptly changes slope at the middle of the fibre. The strain after 3 hours of creep at 8 MPa is now positive in the middle of the fibre and still negative at the end, where the strain profile is very nonlinear



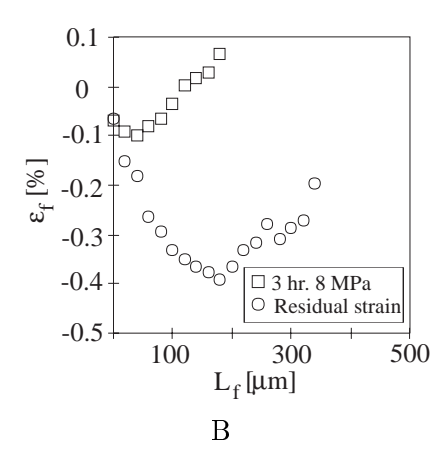
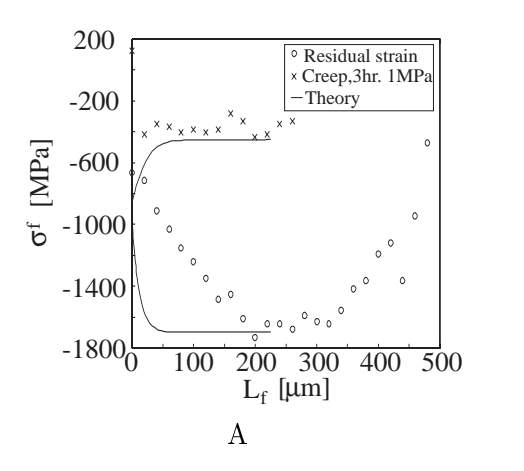


Figure 5.17: Fibre strain A) calculated and B) measured.

with respect to the longitudinal coordinate. In Fig. 5.17A the calculated fibre strain is shown. The characteristics of the experiment is predicted by the model. However, all of the fibre is in tension, whereas the experiment shows compression at the end of the fibre. This difference may again be due to the assumption of the constant interfacial tractions.



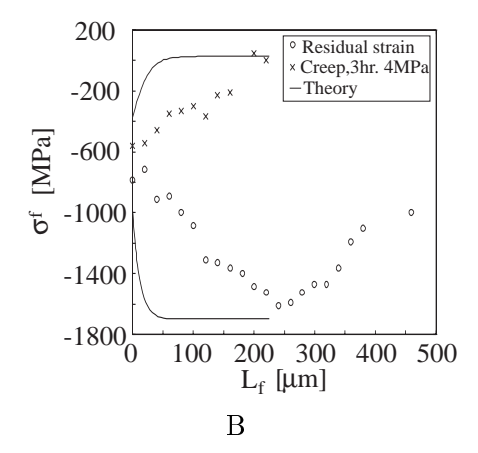


Figure 5.18: Fibre strain A) for a load of 1 MPa and B) for a load of 4 MPa.

As mentioned previously the magnitude of the measured fibre strains and the calculated fibre strains are not directly comparable due to the assumption of plane strain. However, the differences between the maximum longitudinal fibre stress in the plane strain situation and experiments are almost exactly equal to  $2\pi$ . This is also the case when comparing an axisymmetric FE model to a plane strain FE model, subjected to the same farfield stress.

Integrating the calculated interfacial shear stress along the fibre and around the circumference of a circular fibre and multiplying by  $2\pi$  the agreement is quite good with respect to the maximum stress value of the calculated and measured fibre axial stress. The results for cases corresponding to applied loads of 1 and 4 MPa are shown in figures 5.18A and B, respectively.

In figure 5.19 the strain in the matrix after 3 hours of creep at 1 MPa load is shown. The fibre strains are calculated at a distance of 1  $\mu$ m from the outer surface of the fibre and no residual stresses are accounted for in this result. The overall applied strain is 0.15 % and along the fibre the local matrix strain is restricted to a strain level of approximately 0.1 %. At the ends of the fibre, however, a large strain concentration is present which suggests the possibility of localised

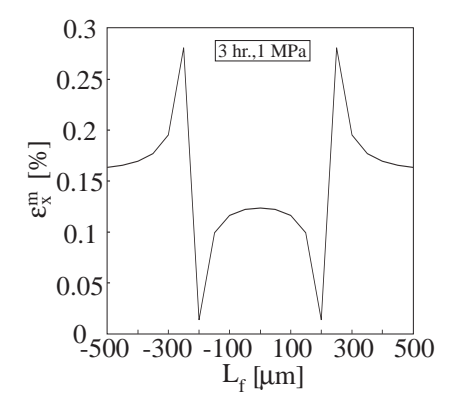


Figure 5.19: Matrix creep strain adjacent to the fibre after 3 hours creep.

yielding.

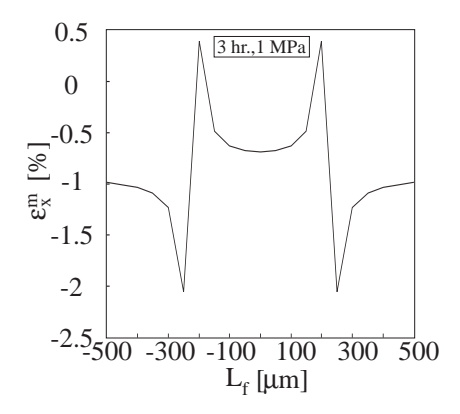


Figure 5.20: Matrix creep strain adjacent to the fibre after 3 hours creep. Residual strains are present in the matrix.

In figure 5.20 the strain in the matrix after 3 hours of creep at 1 MPa load is shown. The fibre strains are calculated at a distance of 1  $\mu$ m from the outer surface of the fibre and residual stresses are accounted for in this result. The overall applied load is - as previously - 0.15 %. In this situation where residual stresses are present the local matrix strain is compressive. A very interesting prediction can be made from this result. If the large compressive strains at the fibre ends can be minimised to avoid yielding and compressive fibre fractures the initial residual strains are beneficial for the overall performance of the composite, i.e. more load can be applied before any fibre fractures occur. However, that may be an extremely difficult task because other phenomena may occur in the interface and adjacent matrix such as nucleation of spherulites which may also lead to fibre fractures. Another important aspect of figures 5.19 and 5.20 are the pronounced singularities at the fibre ends. These singularities are due to 1) plasticity not being accounted for in the model and 2) the nature of the point forces. A comparison of the initial residual stresses at the interface as predicted by the model and FEM is shown in figure 5.21. No nonlinear phenomena except the Young's moduli as a function of temperature is considered.

It is clearly seen that the stresses calculated by the FE model displays a pronounced singularity

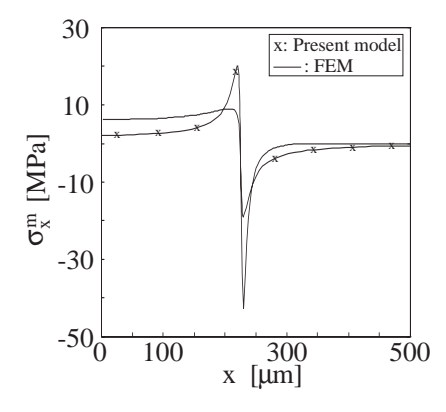


Figure 5.21: Initial residual stress in the matrix adjacent to the fibre.

at the fibre end, which lead to compressive stresses of magnitude -40 MPa. The present model displays an oscillating behaviour at the fibre end causing stresses of  $\pm$  20 MPa. However, both the model and FEM predict a large stress concentration at the fibre end which will most likely lead to severe yielding at the interface which may be the reason for the linearity of the measured strain profiles in figures 5.15B, 5.16B and 5.17B.

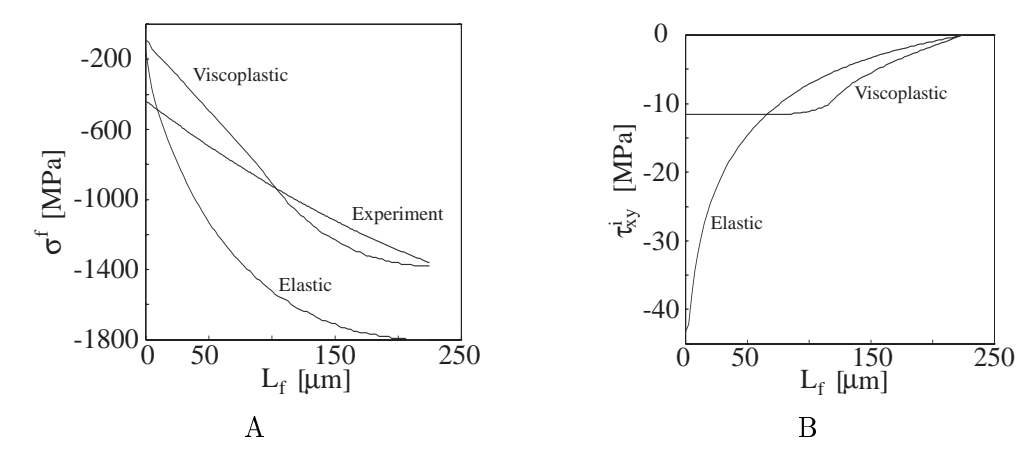


Figure 5.22: Initial residual stresses: A) longitudinal fibre stress and B) interfacial shear stress.

In figure 5.22A the calculated and measured initial residual fibre strains are shown. The elastic and visco-plastic stresses are calculated using FEM. The visco-plastic stresses are found using the Bailey-Norton creep law in conjunction with the von Mises yield criterion. The yield strength of PP is found as  $\sqrt{3}$  times the calculated shear yield strength determined in the previous chapter, thus  $\sigma_Y = 11\sqrt{3} = 19$  MPa. From the figure it is clearly seen that the slope of the calculated stress is decreased towards a constant value if yielding is taken into account. Comparing the magnitude of the visco-plastic stresses with the magnitude of the stress calculated from the measured strain a relatively good agreement is seen, whereas the slopes are different.

Considering figure 5.22B which shows the initial residual interfacial shear stress. From the viscoplastic shear stress a linear plateau is seen, which indicates the length of the yield zone along the fibre. It is seen that the yield zone expands to more than 100  $\mu$ m away from the fibre end. This is in quite good agreement with the linear parts of the measured strains in figures 5.15B, 5.16B and 5.17B.

The last result obtained from approach II is shown in figure 5.23, where the fibre strain in a misaligned fibre is shown. In figure 5.23A the calculated fibre strain is shown and in figure 5.23B the measured fibre strain is shown.

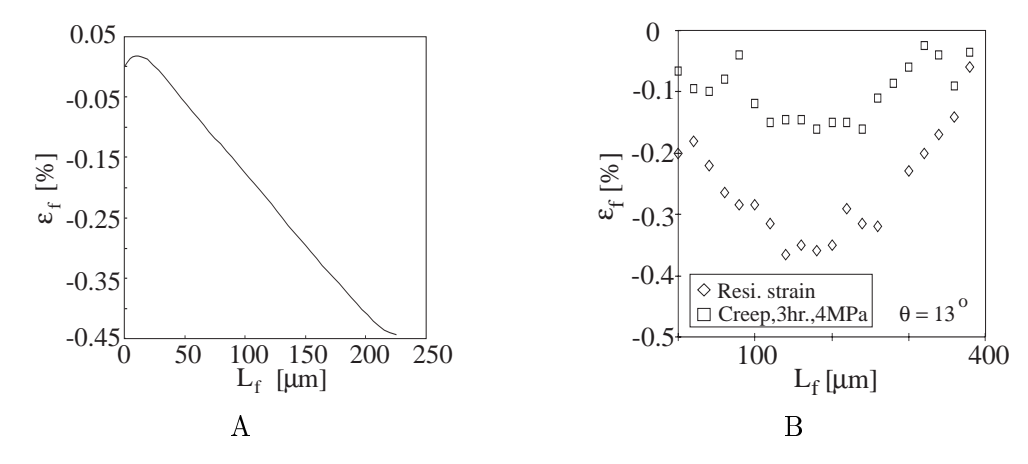


Figure 5.23: Fibre strain A) calculated and B) measured in a fibre misaligned by  $\theta = 13^{\circ}$ .

From figure 5.23A it is clear that the model captures the tendencies of the experiment but again the magnitude of the calculated fibre strain differs. The calculated fibre strains are now larger than the measured fibre strains. The interfacial shear stress calculated via equation (5.1) is constant along the fibre boundary and therefore contributes too much to the fibre normal stress at the middle of the fibre. However, as seen in the figure approach II predicts an increase in fibre strain at the first portion of the fibre and then a decay in fibre strain, just as observed in the experiments.

In figure 5.24 the fibre stress is shown after 3 hours of creep at 8 MPa.

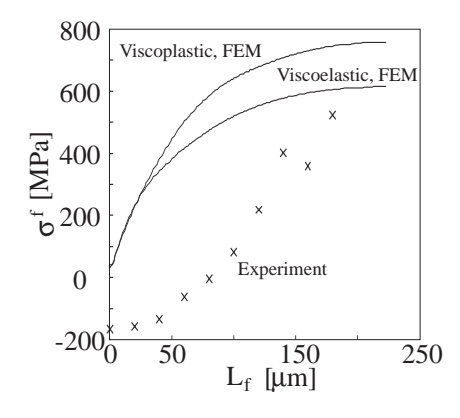


Figure 5.24: The fibre stress after 3 hours of creep at 8 MPa.

Calculated results were obtained from a viscoelastic finite element model and from a viscoplastic finite element model. The experimental result corresponds to the mean value obtained from the experiments conducted at this load level. From the figure it is clearly seen that the viscoplastic FE model predicts larger fibre stress than the viscoelastic FE model because the matrix yields and thus more load needs to be transferred to the fibre to maintain equilibrium. A very interesting feature is seen in the figure. The fibre is in compression at the end which seems unlikely

since the overall strain is larger than the initial thermal strain and thus the fibre should be in tension. However, other investigators such as Huang and Young [43], Melanitis et al. [66] and Paipetis and Galiotis [79] measured compressive strains at fibre ends or at fibre fractures. A possible explanation may be found in the paper by Day and Young [19] who pointed out that effects from the matrix may lead to a different peak position being found for a fibre within a composite, compared to that measured in air for the same type of fibre at the same laser power and load level. This may explain the compressive strains at the fibre end because the "zero strain" peak position may be different - when the fibre is embedded in the matrix - from that found in air. However, since the results for the initial residual stress are quite good this may not be the entire explanation.

Deviations in the shape of the fibre longitudinal stress are most likely due to the fact that the yield stress is temperature dependent and not a constant as used in the FE modelling. Since the yield stress is calculated on the basis of the initial thermal residual strains the calculated value may be an averaged value over the temperature interval and not the actual value of the yield stress at room temperature.

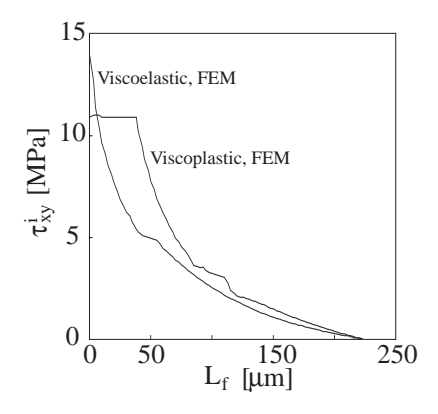


Figure 5.25: The interfacial shear stress after 3 hours of creep at 8 MPa.

Another feature to notice is the linear distribution along the first 50  $\mu$ m which indicates the yield zone, as can also be seen in figure 5.25.

# 5.5 Summary

Two slightly different approaches to determine the matrix creep strains have been shown. Approach I is used when the load transfer is friction-like and approach II is used when the load transfer is due to better adhesion between the fibre and matrix.

The first approach uses and determines the coefficient of friction. From experimental measurements of the fibre strain the interfacial shear stress is calculated. The transverse normal stress from a Lamé solution together with the interfacial shear stress is then used to calculate the coefficient of friction. The interfacial shear stress and the transverse normal stress are then integrated along the fibre boundary, thus giving the stresses everywhere in the matrix. The calculated stresses are inserted into the three dimensional constitutive law of the matrix thus giving the creep strains in the matrix.

The major assumptions are that no stresses are transferred across the fibre ends and that the

96 5.5. Summary

matrix strain can be calculated due to stresses which are not varied in time but are the result of the actual loading history. Another restriction in the use of this approach is that the Lamé solution is derived for infinitely long fibres. When using the Lamé solution for short fibres it must be ensured that the "short" fibre is sufficiently long so that the fibre stress build up zone is short compared to the zone of constant longitudinal fibre stress, otherwise the calculated coefficient of friction may be far from approximately correct.

The creep strains in the matrix - obtained from approach I - are too large mainly due to the fact that stress relaxation is not considered in this model. However, the model predicts some of the observations from experiments, eg. the fact that the fibres will carry less and less load for increasing loading times or increasing load.

The load transfer mechanism may not be entirely due to Coulomb friction but due to interaction of the surface roughness of the matrix and fibre, respectively. However, the Coulomb friction assumption yields the linear fibre strain profile and is supported by [48] and [53] and the FEM calculations.

The second approach is purely theoretical and based on Eshelby's thought experiment which leads to expressions for the initial elastic interface tractions which are integrated along the fibre boundary, thus giving the initial elastic stresses in the matrix. These stresses are inserted into the three dimensional constitutive law of the matrix to obtain the initial elastic strains. The elastic strains cause stress relaxation during time, dt, which leads to a new state of stress used in the next time step. From this approach the creep strains in the matrix can be calculated at any time and at small misalignment angles of the fibre.

The major approximations are that for small angles of misalignment with respect to the loading direction the shear stresses at the interface are calculated through the transformation of second order tensors. Secondly, shear stresses across the fibre ends are neglected. Finally, the disturbed stress/strain field is assumed to be additive with the applied uniform stress/strain field. This seems reasonable since the overall applied stress is not relaxed during the time of duration.

The magnitude of the fibre strains calculated using this model are not directly comparable to experiment because the model assumes plane strain. The difference between experimental results and results from the plane model corresponds to  $2\pi$  which is also observed when comparing a plane strain FE model to an axisymmetric FE model, both subjected to the same farfield stress. The nature of the interfacial tractions controls the form of the interfacial shear stress which also governs the shape of the longitudinal fibre stress profile. As a consequence the rates at which the strain is built up in the fibre are different when comparing calculations and experiments. The major contributor to this deviation is that yielding occurs at the interface which is not considered by this approach. However, the characteristics of the experiments are reflected in the theoretical predictions and it is believed that this approach has potential for refinement in order to improve the results. The main reason for refining the model is that the computational time for one of the analysis shown previously is about 15-30 minutes, whereas the same analysis takes several hours using nonlinear FEM.

The two approaches do not incorporate the effects of an interface with mechanical properties differing from that of the fibre and matrix material but it will be possible to take that into consideration through an iterative interaction procedure.

A general trend is that the initial residual stress in the fibre is restricting the level of the fibre strain during subsequent creep loading, which is also observed in the experiments. This may actually be beneficial for the composite regarding tensile fibre fractures. Comparisons between experiments and FEM have shown the best agreement when comparing initial residual stress, whereas the creep modelling using FEM has not been quite as successful. For the FE models with the frictional interface the reason for the deviation between experimental results and calculated results is that the fibre and matrix are debonding at the end at load application and this is not accounted for in the FE models.

The results from the FE models used for comparison with the PP-MA composites also differ from experiments when creep loading is applied and the most likely explanation is that the yield stress is in fact temperature dependent and not a constant as used in the FE modelling.

98 5.5. Summary

6

# **Overall Creep Modelling**

The fibres are oriented differently in the matrix through a distribution function of the Euler angles. No fibre length distribution function is used, i.e. the fibres are of the same length. The approach is based upon the Mori-Tanaka mean field theory in which the fibres are considered as inhomogeneities containing equivalent eigenstrains. Furthermore, the effect of an imperfect interface is considered through a modified Eshelby tensor.

## 6.1 Overall modelling

Micromechanical analysis of composite materials provides their overall behaviour from the known properties of the individual constituents and their detailed interaction. In the macromechanical approach the heterogeneous structure is replaced by a homogeneous medium with anisotropic properties which have to be determined. The advantage of the micromechanical approach is that no a priori assumptions are necessary for the establishment of the composite response since the analysis provides the requested average behaviour. Since the behaviour of the composite is generally anisotropic it is of great importance that no directionally dependent responses are assumed. The micromechanical approach has another advantage since only constituent properties are used and thus avoids the difficulty of having to evaluate all kinds of fibre-matrix combinations.

An adequate prediction of the overall properties of a material must be the final goal if the material is to be used by a practicing engineer in "real life" situations. Therefore large efforts have been put into establishing methods to determine the overall response of various composite materials. Some of these approaches are based on sophisticated micromechanics and some of them are more simple.

The first method to determine the overall stiffness of a two phase material was suggested by Voigt in 1889 and is probably the simplest one, (Rule of mixtures), assuming that the stiffness of the constituents are additive multiplied by their respective volume fractions. Another simplistic model is the one suggested by Reuss in 1929. It is analogous to the Voigt model but uses the compliances of the constituents and thus gives the overall compliance of a two phase material, [1].

Later, in 1952 Hill showed that the Reuss and Voigt models in fact correspond to the upper and lower bounds of the actual elastic moduli of a two phase composite. These bounds, however, are only of interest in the case of small fibre volume fractions and only in case of small mismatchs

between the matrix and fibre moduli. Better universal bounds have been established by Hashin and Shtrikman [38], by the use of variational principles.

In 1957 Eshelby suggested the equivalent inclusion method, [24], which incorporates his transformation strain also known as Mura's equivalent eigenstrain, [69]. The eigenstrains can be considered as being body forces i.e. the eigenstrains contributions to the equations of equilibrium are equivalent to that of a body force.

Eshelby used the equivalent inclusion method in conjunction with the formation of twins and the martensitic transformation in metals. This is a very elegant approach and the concept of equivalent eigenstrains have been used widely within the field of micromechanics. However, the equivalent inclusion method does not take the interaction of neighbouring fibres into account and is therefore only suited for dilute concentrations of fibres.

In the case where the material considered is a polycrystal the concept of a matrix with embedded fibres is no longer relevant and the concentrations of fibres is no longer dilute. In this situation a suitable method for calculating the overall properties is the self consistent method which was first proposed by Hershey in 1954 and used for calculating the overall moduli of polycrystals [72]. In 1965 Budiansky applied the self consistent method to composites. In this approach a single typical fibre is embedded in an infinite homogeneous material with the yet unknown overall moduli and the local average quantities are estimated and used to obtain the overall moduli. The self consistent method have been used to estimate the overall elastic moduli of composite materials by Walpole [116] and Chou et al. [16], to model the elastoplastic behaviour of polycrystals by Hill [40], and to model the viscoelastic behaviour of metals by Weng [123], [124] and Lin et al. [57].

The self consistent model does take interaction affects into account - to a certain extent. Since the fibre is embedded in an infinitely extended solid the interaction between the fibres and their immediate surrounding matrix material of different elastic moduli is not directly included in the model. In fact the self consistent model should be used with caution when the volume fraction of fibres is larger than  $\approx 0.4$  [1]. To take interaction more directly into account the Mori - Tanaka model is a better alternative.

The Mori - Tanaka model was established by Mori and Tanaka in 1973, [68]. This model assumes that the average strain in the interacting fibres can be approximated by that of a single fibre embedded in an infinite matrix subjected to a uniform average matrix strain. To solve this problem a single fibre is embedded in a volume of *finite* size and subjected to the uniform average matrix strain. This method has been used widely and is the method to be used to model the overall creep behaviour in the present work. The Mori -Tanaka method has been used by Chen et al. [13] and Benveniste et al. [6] to find the stress field in a composite with coated fibres and by Chen et al. [14] to find the overall elastic moduli of composites with different fibre distributions. Finally Wang and Weng [119], [120] and Zhu and Weng [136] based their viscoelastic modelling on the Mori - Tanaka method.

These approaches are not the only ones but many of the other existing models are derivatives of the models mentioned above. One such approach is the generalised self consistent method (also called the three phase model) in which a single inclusion surrounded by matrix material of finite size is embedded in an infinite homogeneous medium with the as yet unknown elastic properties of the composite. Unfortunatelly, analytical solutions are only obtainable in special cases. Thus, the generalised self consistent method usually provides an analytical solution when considering coated spheres or coated infinitely long cylindrical fibres, loaded transversely.

The aforementioned models only considered perfect interfaces. When the interface is imperfect

some additional approaches have been undertaken. Pagano and Tandon [77], [78] used a traction formulation in cylindrical coordinates for each inhomogeneity subjected to local boundary conditions and ensuring equilibrium on any cross section in the composite. A similar approach has been undertaken by Dvorak and Benveniste [22] and Benveniste [5].

The approach which will be used here is the one proposed by Qu [88], [89], where a modified Eshelby tensor is formulated which takes into account the effect of a weakened interface. The modified Eshelby tensor is used in conjunction with the Mori - Tanaka model in order to predict the overall behaviour of a composite with weakened interfaces.

### 6.2 Incremental Creep Modelling

In order to calculate the overall creep strain of the composite the average stress of the matrix containing the fibres will be calculated by means of the Mori - Tanaka method [68]. In the approach the overall moduli of the composite is calculated and used to determine the initial mean stress in the composite. Then the matrix is allowed to creep during a small time increment and the load distribution between the fibre and matrix is determined through a change in the eigenstrains. To use this approach the incremental creep strain of the matrix is repeated here.

Remembering the tensorial creep expression

$$\varepsilon_{ij} = \tilde{D}(t) \left\{ (1 + \nu)\sigma_{ij} - \nu \sigma_{kk} \delta_{ij} \right\}$$
(6.1)

this, when differentiated with respect to time gives the incremental creep strain as

$$d\varepsilon_{ij} = \{(1+\nu)\sigma_{ij} - \nu\sigma_{kk}\delta_{ij}\}\frac{\partial \tilde{D}(t)}{\partial t}dt$$
(6.2)

#### Initial Mean Stress of the Matrix

The composite is subjected to a boundary traction giving rise to a uniform stress  $\bar{\sigma}_{ij}$ . Now an equivalent material is introduced, which has the same mechanical properties as the matrix material of the composite system, and is subjected to the same boundary tractions. The uniform strain in the equivalent material is then given as

$$\varepsilon_{kl}^0 = [C_{ijkl}^{(1)}]^{-1} \bar{\sigma}_{ij} \tag{6.3}$$

A superscript (1) and (2) will subsequently denote matrix and fibre quantities, respectively. Due to the presence of the fibres the average stress and strain of the matrix in the composite system will usually differ from the uniform stress  $\bar{\sigma}_{ij}$  and the uniform strain  $\varepsilon_{kl}^0$ . These differences are denoted by  $\tilde{\sigma}_{ij}$  and  $\tilde{\varepsilon}_{ij}$ , respectively, giving the average matrix stress as

$$\sigma_{ij}^{(1)} = \bar{\sigma}_{ij} + \tilde{\sigma}_{ij} = C_{ijkl}^{(1)}(\varepsilon_{kl}^0 + \tilde{\varepsilon}_{kl})$$

$$(6.4)$$

As mentioned previously the fibres are modelled as inhomogeneities containing Eshelby's equivalent eigenstrains. Due to the different stiffness properties of the fibre and matrix, the fibre stress and fibre strain will furthermore differ from the mean matrix stress and strain by the perturbed

stress,  $\sigma_{ij}^{pt}$  and strain  $\varepsilon_{ij}^{pt}$ , such that the mean fibre stress can be written in terms of their own elastic moduli as well as in terms of Eshelby's equivalence principle

$$\sigma_{ij}^{(2)} = \bar{\sigma}_{ij} + \tilde{\sigma}_{ij} + \sigma_{ij}^{pt} = C_{ijkl}^{(2)}(\varepsilon_{kl}^0 + \tilde{\varepsilon}_{kl} + \varepsilon_{kl}^{pt}) = C_{ijkl}^{(1)}(\varepsilon_{kl}^0 + \tilde{\varepsilon}_{kl} + \varepsilon_{kl}^{pt} - \varepsilon_{kl}^*)$$
(6.5)

where  $\varepsilon_{kl}^*$  is the equivalent eigenstrain introduced into the regions of the comparison material corresponding to the sites of the composite occupied by the fibres to cause the same mean fibre stress  $\sigma_{ij}^{(2)}$ . The perturbed strain is related to the equivalent eigenstrain in terms of the Eshelby tensor  $S_{ijkl}$ 

$$\varepsilon_{ij}^{pt} = S_{ijkl} \varepsilon_{kl}^* \tag{6.6}$$

where the Eshelby tensor is given in terms of second order derivatives of Green's function  $G_{im}(\mathbf{x} - \mathbf{x}')$ 

$$S_{ijkl} = -C_{mnkl}^{(1)} \int_{\Omega} G_{im,nj}(\mathbf{x} - \mathbf{x}') d\mathbf{x}$$

$$(6.7)$$

where the integration is taken over a volume,  $\Omega$ , corresponding to the volume occupied by the fibre.  $G_{im}(\mathbf{x} - \mathbf{x}')$  is Green's function and is a fundamental solution to Navier's equation expressed in terms of displacements. Green's function represents the displacement component in the  $x_i$  direction at point  $\mathbf{x}$  when a unit body force in the  $x_m$  direction is applied at point  $\mathbf{x}'$ . The expression for the Eshelby tensor reduces to some simple algebraic expressions containing only the aspect ratio of the fibres and Poisson's ratio for the matrix material.

As a consequence of the average stress theorem, (Appendix B), the mean composite stress can be written as

$$\bar{\sigma}_{ij} = \sum c_r \sigma_{ij}^{(r)} \tag{6.8}$$

where  $c_r$  is the volume fraction of phase r. Combining this with equations (6.4) and (6.5) the stress difference  $\tilde{\sigma}_{ij}$  and the strain difference  $\tilde{\varepsilon}_{ij}$  in the matrix are readily found

$$\tilde{\sigma}_{ij} = -c_2 \sigma_{ij}^{pt} 
\tilde{\varepsilon}_{ij} = -c_2 (S_{ijmn} - I_{ijmn}) \varepsilon_{mn}^*$$
(6.9)

where  $I_{ijmn}$  is the fourth order identity tensor given by

$$I_{ijmn} = \frac{1}{2} \left( \delta_{im} \delta_{jn} + \delta_{in} \delta_{jm} \right) \tag{6.10}$$

These are now inserted into equation (6.5) and the relation between the strain in the comparison material  $\varepsilon_{kl}^0$  and the eigenstrain  $\varepsilon_{mn}^*$  is

$$\varepsilon_{mn}^* = A_{mnkl} \varepsilon_{kl}^0 \tag{6.11}$$

where the fourth order tensor  $A_{mnkl}$  is given by

$$A_{mnkl} = -\left[ \left( C_{ijkl}^{(2)} - C_{ijkl}^{(1)} \right) \left( c_1 S_{klmn} + c_2 I_{klmn} \right) + C_{ijmn}^{(1)} \right]^{-1} \left( C_{ijkl}^{(2)} - C_{ijkl}^{(1)} \right)$$
(6.12)

Using the average strain theorem (Appendix B) and equation (6.6) the initial mean strain in the composite at time t = 0 is obtained as

$$\bar{\varepsilon}_{ij} = \varepsilon_{ij}^{0} + c_{2} \varepsilon_{ij}^{*}$$

$$\bar{\varepsilon}_{ij} = (I_{ijkl} + c_{2} A_{ijkl}) \varepsilon_{kl}^{0}$$
(6.13)

and the initial mean stress of the matrix

$$\sigma_{ij}^{(1)} = [I_{ijkl} - c_2 C_{ijpq}^{(1)} (S_{pqmn} - I_{pqmn}) A_{mnrs} C_{klrs}^{(1)}] \bar{\sigma}_{kl}$$
(6.14)

where  $\bar{\sigma}_{kl}$  is the applied load.

#### Subsequent Load Redistribution

The application of  $\bar{\sigma}_{ij}$  creates an initial creep strain which, over a time increment dt, creates an incremental creep strain,  $d\varepsilon_{ij}^c$ . The next concern is the stress redistribution between the matrix and fibre following an incremental creep with  $\bar{\sigma}_{ij}$  kept constant. The incremental creep of the matrix is followed by a stress reduction which has to be carried by the elastic fibres in order to maintain a constant  $\bar{\sigma}_{ij}$ . This is not an easy task for a nonlinear matrix undergoing both primary and secondary creep. It is therefore assumed that for small increments of stress the constraint of the matrix is elastic. This assumption is essential in solving the problem because if the incremental response, in each time step, is time dependent one needs the time dependent properties of the composite as a whole and this corresponds to solving the entire composite creep problem.

In order to estimate the average stress variation in both phases, the fibres are first taken out of the matrix and the matrix is allowed to creep homogeneously over a short time dt. The fibres are then subjected to a boundary traction corresponding to a homogeneous stress  $C_{ijkl}^{(2)}d\varepsilon_{kl}^{c}$  so that they will fit perfectly into the deformed holes of the matrix, figure 6.1. A boundary traction of the opposite sign  $-C_{ijkl}^{(2)}d\varepsilon_{kl}^{c}$  is now applied to the interface between the matrix and fibre in order to remove the traction discontinuity. This is equivalent to having a stress free eigenstrain

$$d\varepsilon_{ij}^{**} = -d\varepsilon_{ij}^c \tag{6.15}$$

The average stress variation in the matrix is now obtained as

$$d\sigma_{ij}^{(1)} = d\tilde{\sigma}_{ij} = C_{ijkl}^{(1)} d\tilde{\varepsilon}_{kl} \tag{6.16}$$

Noting that a stress free eigenstrain variation  $d\varepsilon_{kl}^{**}$  already existed in the inclusion and  $d\varepsilon_{kl}^{*}$  is the equivalent eigenstrain variation due to the different mechanical properties of the fibre and matrix, the total eigenstrain variations give the perturbed strain variations,  $d\varepsilon_{ij}^{pt}$  and  $d\tilde{\varepsilon}_{ij}$  as

$$d\tilde{\varepsilon}_{ij} = -c_2 (S_{ijkl} - I_{ijkl}) (d\varepsilon_{kl}^* + d\varepsilon_{kl}^{**}) d\varepsilon_{ij}^{pt} = S_{ijkl} (d\varepsilon_{kl}^* + d\varepsilon_{kl}^{**})$$

$$(6.17)$$

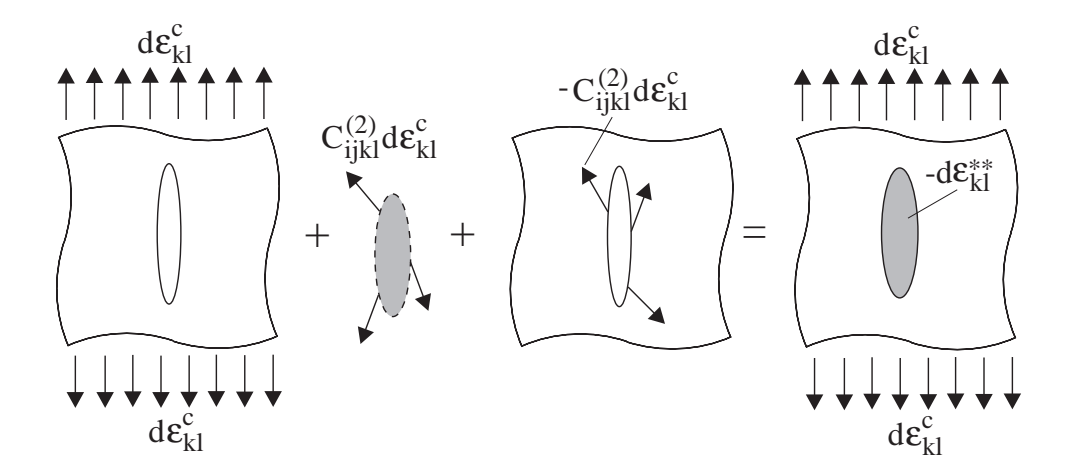


Figure 6.1: Superposition of the pure deformed matrix, the inclusion with surface tractions and the surface tractions of opposite sign at the interface gives the homogeneous material with a distribution of eigenstrains.

Using the average stress theorem the overall creep strain variation over time dt is now obtained as

$$d\bar{\varepsilon}_{ij}^c = d\varepsilon_{ij}^c + c_2(d\varepsilon_{ij}^* + d\varepsilon_{ij}^{**})$$
(6.18)

thus the central aspect in the determination of the load redistribution is the determination of the eigenstrain variations  $d\varepsilon_{kl}^* + d\varepsilon_{kl}^{**}$ . Using both of equations (6.17) and equation (6.5) leads to

$$[(C_{ijkl}^{(2)} - C_{ijkl}^{(1)})(c_2 I_{klmn} + c_1 S_{klmn}) + C_{ijmn}^{(1)}](d\varepsilon_{mn}^* + d\varepsilon_{mn}^{**}) = -C_{ijkl}^{(2)} d\varepsilon_{kl}^c$$
(6.19)

where  $d\varepsilon_{kl}^c$  is the creep strain variation in the matrix material. Now the eigenstrain variation can be found by inserting the initial stress into equation (6.2). Then  $d\varepsilon_{ij}^c$  is inserted into the equation above giving a set of 6 algebraic equations in the 6 unknown eigenstrain variations,  $(d\varepsilon_{mn}^* + d\varepsilon_{mn}^{**})$ .

The stress variation in the matrix are now obtained as

$$d\sigma_{ij}^{(1)} = -c_2 C_{ijkl}^{(1)} (S_{klmn} - I_{klmn}) (d\varepsilon_{mn}^* + d\varepsilon_{mn}^{**})$$
(6.20)

This equation together with the initial stress, equation (6.14), provides a new state of stress in the next time increment.

The fact that the fibre and interface are subjected to boundary conditions of magnitude  $C_{ijkl}d\varepsilon_{kl}^c$  restricts the time increments and the resulting  $d\varepsilon_{kl}^c$  to be very small in order to ensure that this approach does not lead to erroneous results.

### 6.3 Imperfect Interface

The experimental results have shown the load transfer from the matrix to the fibres in the PP-U specimens were governed by the initial residual stress and the coefficient of friction. This non-perfect load transfer is accounted for in the overall creep modelling by using the modified Eshelby tensor for sligthly weakened interfaces as proposed by Qu [88], [89]. By introducing a displacement discontinuity in the interface conditions the displacement field can be expressed as an integral equation in terms of the displacement discontinuity and second order derivatives of Green's function. An asymptotic solution to this integral equation is then used to model the effect of a weakened interface.

The interface between the inclusion and matrix is assumed nonperfect. A spring layer of vanishing thickness will be used to characterise the nonperfect bonding. The interfacial tractions are still continuous, but a displacement discontinuity may occur at the interface. Although some nonlinear relations between the interfacial traction and displacement jumps may be proposed, a linear spring model is used. If S and  $n_i$  denotes the interface and its unit outward normal, the interfacial conditions are [88]

$$\Delta \sigma_{ij} n_j = [\sigma_{ij}(\mathbf{x})|_{S^+} - \sigma_{ij}(\mathbf{x})|_{S^-}] n_j = 0$$
  
$$\Delta u_i = u_i(\mathbf{x})|_{S^+} - u_i(\mathbf{x})|_{S^-} = \eta_{ij}\sigma_{jk} n_k$$

where  $S^+$  and  $S^-$  indicates approaching the interface from outside or inside of the inclusion, respectively.  $\eta_{ij}$  represents the compliance of the spring layer and  $\eta_{ij} = 0$  corresponds to the perfect bonding whereas  $\eta_{ij} \to \infty$  represents complete debonding. The specific form of  $\eta_{ij}$  used in this investigation is given by

$$\eta_{ij} = \alpha \delta_{ij} + (\beta - \alpha) n_i n_j \tag{6.21}$$

where  $\alpha$  and  $\beta$  represent the compliance in the tangential and normal directions, respectively. If  $\beta \neq 0$  then material interpenetration may take place, which is a violation of the compatibility equations and thus only  $\alpha \neq 0$  in this work.  $\alpha \neq 0$  implies that relative sliding at the interface between the fibre and matrix may occur.

If a domain,  $\Omega$ , contains eigenstrains,  $\varepsilon_{ij}^*$ , the equilibrium equations in terms of displacements can be expressed as

$$C_{ijkl}u_{k,lj} - C_{ijkl}\varepsilon_{kl,j}^* = 0 \qquad \text{in } \Omega$$
 (6.22)

where  $C_{ijkl}\varepsilon_{kl,j}^*$  can be considered equivalent to a body force. Since the eigenstrains are fictious the stresses are obtained as

$$\sigma_{ij} = C_{ijkl}(u_{k,l} - \varepsilon_{kl}^*) \tag{6.23}$$

This can be formulated into an integral representation of the displacement field  $u_i$  from which the strain can be obtained.

If it is assumed that the eigenstrains are uniform in  $\Omega$  then the strains are

$$\varepsilon_{ij}(\mathbf{x}) = -\varepsilon_{kl}^* C_{klmn} \int_{\Omega} \Phi_{ijmn}(\xi - \mathbf{x}) dv(\xi) - C_{klmn} \int_{S} \Delta u_k(\xi) \Phi_{ijmn}(\xi - \mathbf{x}) n_l ds(\xi)$$
(6.24)

where  $\Phi_{ijmn}$  are second order derivatives of Green's function,  $G_{ij}(\mathbf{x})$ , as

$$\Phi_{ijmn}(\mathbf{x}) = \frac{1}{4} (G_{mi,nj}(\mathbf{x}) + G_{mj,ni}(\mathbf{x}) + G_{ni,mj}(\mathbf{x}) + G_{nj,mi}(\mathbf{x}))$$

and the first integral of equation (6.24) equals the traditional Eshelby tensor. In general the second integral cannot be evaluated analytically and thus an asymptotic solution is used for small values of  $\eta_{ij}$ . Using the interfacial condition,  $\Delta u_i = \eta_{ij}\sigma_{jk}n_k$ , and inserting the expression for stress, equation (6.23), into the second integral of equation 6.24 one obtains

$$\varepsilon_{ij}(\mathbf{x}) = S_{ijkl}\varepsilon_{kl}^* + C_{klmn}C_{pqst}\varepsilon_{st}^* \int_S \eta_{kp} \mathbf{\Phi}_{ijmn}(\xi - \mathbf{x}) n_q n_l ds(\xi)$$
$$-C_{klmn}C_{pqst} \int_S \eta_{kp}\varepsilon_{st}(\xi) \mathbf{\Phi}_{ijmn}(\xi - \mathbf{x}) n_q n_l ds(\xi)$$
(6.25)

from which an iteration procedure can be formulated as

$$\varepsilon_{ij}^{(n)}(\mathbf{x}) = S_{ijkl}\varepsilon_{kl}^* + C_{klmn}C_{pqst}\varepsilon_{st}^* \int_S \eta_{kp} \mathbf{\Phi}_{ijmn}(\xi - \mathbf{x}) n_q n_l ds(\xi)$$
$$-C_{klmn}C_{pqst} \int_S \eta_{kp}\varepsilon_{st}^{(n-1)}(\xi) \mathbf{\Phi}_{ijmn}(\xi - \mathbf{x}) n_q n_l ds(\xi)$$
(6.26)

where n = 1, 2... and the initial value of the strain can be taken to be

$$\varepsilon_{ij}^{(0)} = S_{ijkl} \varepsilon_{kl}^* \tag{6.27}$$

the leading order solution for small values of  $\eta_{ij}$  is now obtained as

$$\varepsilon_{ij}(\mathbf{x}) \approx \varepsilon_{ij}^{(1)}(\mathbf{x}) = S_{ijkl}\varepsilon_{kl}^* + T_{ijst}(\mathbf{x})(I_{stkl} - S_{stkl})\varepsilon_{kl}^*$$
(6.28)

where the fourth order tensor  $T_{ijst}(\mathbf{x})$  is given as

$$T_{ijst}(\mathbf{x}) = C_{klmn}C_{stpq} \int_{S} \eta_{kp} \mathbf{\Phi}_{ijmn}(\xi - \mathbf{x}) n_q n_l ds(\xi)$$
(6.29)

which leads to the modified Eshelby tensor  $S^{M}_{ijkl}(\mathbf{x})$ 

$$S_{ijkl}^{M}(\mathbf{x}) = S_{ijkl} + T_{ijst}(\mathbf{x})(I_{stkl} - S_{stkl})$$

$$\tag{6.30}$$

and it is seen that the strains are no longer uniform inside the inclusion.

The nonuniformity of strain inside the inclusion restricts this approach to small values of  $\eta_{ij}$  sligthly weakened interfaces - because in equation (6.28) it is assumed that  $\varepsilon_{ij} = S_{ijkl}\varepsilon_{kl}^*$  and the
traditional Eshelby tensor  $S_{ijkl}$  is derived on the basis of a constant strain in the inclusion.

Now the volume averaged modified Eshelby tensor  $\langle S_{ijkl}^M \rangle$ , to be used in conjunction with the Mori - Tanaka approach, is given as [89]

$$\langle S_{ijkl}^{M} \rangle = S_{ijkl} + (I_{ijpq} - S_{ijpq}) H_{pqrs} C_{rsmn} (I_{mnkl} - S_{mnkl})$$

$$\tag{6.31}$$

where

$$H_{ijkl} = \alpha P_{ijkl} + (\beta - \alpha) Q_{ijkl} \tag{6.32}$$

and  $P_{ijkl}$  and  $Q_{ijkl}$  are given as

$$P_{ijkl} = \frac{3}{16\pi} \int_0^{\pi} \left[ \int_0^{2\pi} \left( \delta_{ik} n_j n_l + \delta_{jk} n_i n_l + \delta_{il} n_k n_j + \delta_{jl} n_k n_i \right) n^{-1} d\phi \right] \sin(\theta) d\theta$$

$$Q_{ijkl} = \frac{3}{4\pi} \int_0^{\pi} \left[ \int_0^{2\pi} n_i n_j n_k n_l n^{-3} d\phi \right] \sin(\theta) d\theta$$

where  $n = \sqrt{n_i n_i}$  and  $n_i$  is

$$n_i = \left(\frac{\cos \theta}{a_1}, \frac{\sin \phi \sin \theta}{a_2}, \frac{\sin \theta \cos \phi}{a_3}\right)^T \tag{6.33}$$

in which  $a_1$ ,  $a_2$  and  $a_3$  are the three semi axes of the ellipsoid.

In this approach the fibres are considered to be infinitely long since it can be shown that when the aspect ratio of the inclusions are larger than 25 the difference between the general expressions for the Eshelby tensor and the expressions for infinitely long fibres differ by less than 0.5 %. Thus  $S_{ijkl}$  are given as

$$S_{1111} = 0$$

$$S_{2222} = \frac{5 - 4\nu^{(1)}}{8(1 - \nu^{(1)})}$$

$$S_{3333} = S_{2222}$$

$$S_{2233} = \frac{4\nu^{(1)} - 1}{8(1 - \nu^{(1)})}$$

$$S_{3322} = S_{2233}$$

$$S_{2211} = \frac{\nu^{(1)}}{2(1 - \nu^{(1)})}$$

$$S_{3311} = S_{2211}$$

$$S_{1122} = 0$$

$$S_{1133} = S_{1122}$$

$$S_{2323} = \frac{3 - 4\nu^{(1)}}{8(1 - \nu^{(1)})}$$

$$S_{1212} = \frac{1}{4}$$

$$S_{1313} = S_{1212}$$

### 6.4 Fibre Orientation

The behaviour of short fibre reinforced composites is not only a function of the constituents properties. The internal structure of the material plays a significant role in determining the

performance. The most important feature of the internal structure of short fibre reinforced composites is the state of orientation of the reinforcing fibres. In real short fibre composites processed by injection moulding the fibres are neither aligned nor dispersed in random directions. The consequence of this state of orientation may be that the strength of the moulded part is governed by material regions in which the orientation of minimum strength coincides with that of maximum stress. Due to this state of orientation throughout the material, the material is inherently anisotropic and heterogeneous and thus precludes the use of isotropic analysis, hence increasing the complexity of the analysis. These consequences have been recognised by Pipes et al. [85] and by Bozarth et al. [10] in their investigation of influence of fibre orientation upon thermoelastic properties of short fibre reinforced composites. Takao et al. [112] modelled the effective Youngs modulus in short fibre reinforced composites and Maekawa et al. [62] developed a laminate theory incorporating a fibre distribution function.

To take this anisotropy into account a fibre distribution function is incorporated in the Mori - Tanaka method in the subsequent creep modelling.

In figure 6.2a, a unit sphere is shown within which it is possible to illustrate the fibre distribution. If the orientation directions of all fibres contained in the material are translated towards the unit sphere in such a way that they become attached to the centre point of the sphere, then the directions lines will cross a part of the surface of the unit sphere enclosed by a great circle with radius determined by the angle  $\theta$  provided that all the fibres directions lie in the interval  $[0, \theta]$ .

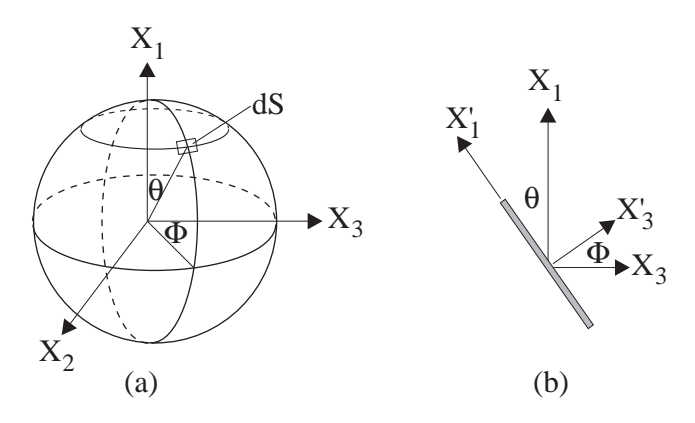


Figure 6.2: a) Unit sphere. b) The fibre in its local coordinate system.

The orientation distribution function  $g(\theta, \Phi)$  describes a number of fibre directions which cross a unit surface area, dS, of the sphere. Assuming that the fibre orientations are uniformly distributed with respect to  $\Phi$  - which is usually the case for injection moulded components where the thickness is much smaller than the other dimensions - the orientation distribution function depends only upon the angle  $\theta$ , where  $\theta = [0, \pi/2]$ . The independence of  $\Phi$  makes the composites considered here transversely isotropic. Since the fibres are considered as being transversely isotropic the third Euler angle is neglected, because a rotation of the fibre with respect to its longitudinal axis does not change the orientation or the directional properties.

In this work the versatile orientation distribution function given by Maekawa et al. [62] is used

$$g(\theta) = \frac{\sin(\theta)^{2P-1}\cos(\theta)^{2Q-1}}{\int_{\theta_a}^{\theta_b}\sin(\theta)^{2P-1}\cos(\theta)^{2Q-1}d\theta}$$
(6.34)

where  $\theta_a$  and  $\theta_b$  are the upper and lower limits of the angle  $\theta$  which are present in the distribution.  $0 < \theta_a, \theta_b < \pi$  and P > 1/2 and Q > 1/2.

The graph of the orientation distribution function is shown in figure (6.3), for P=Q.

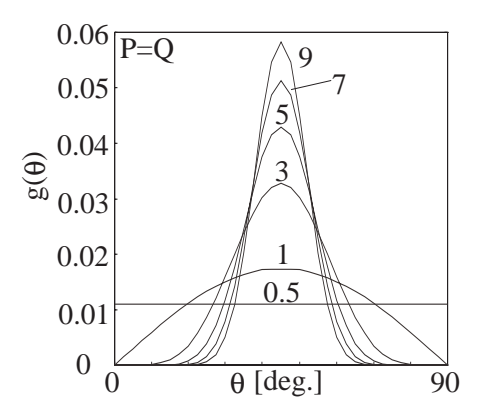


Figure 6.3: The orientation distribution function, for various values of P = Q.

Other distributions such as Gaussian or Weibull distributions are not suited for this type of investigation because these are symmetric and can not display a skew symmetric fibre distribution. The skew symmetric distributions are shown in figure (6.4).

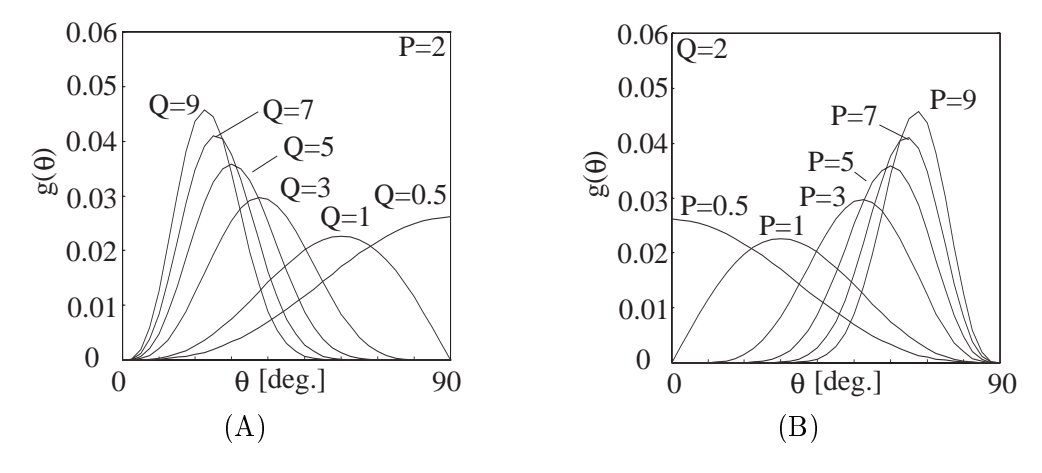


Figure 6.4: Skew symmetric orientation distribution function.

In order to take the fibre distribution into account in the creep modelling, the global boundary conditions are transformed into the local fibre coordinate system figure (6.2b), thereby becoming a function of  $\theta$ 

$$\sigma_{ij} = a_{iM} a_{jN} \sigma_{MN} \tag{6.35}$$

where capital indices denotes the global coordinate system and lower case indices denotes the local fibre coordinate system.  $a_{kL}$  are the direction cosines between the local coordinate axis and the global coordinate axis and are given as

110 6.5. Results

$$a_{kL} = \begin{pmatrix} \cos \theta & 0 & \sin \theta \\ 0 & 1 & 0 \\ -\sin \theta & 0 & \cos \theta \end{pmatrix}$$

$$(6.36)$$

Since each fibre is oriented differently the effect of orientation distribution is taken into account by averaging the eigenstrain over all directions present in the representative volume element as

$$\bar{\varepsilon}_{ij}^* = \frac{\int_0^\theta \int_0^{2\pi} \varepsilon_{ij}^*(\theta, \Phi) g(\theta, \Phi) dS}{\int_0^\theta \int_0^{2\pi} g(\theta, \Phi) dS}$$
(6.37)

where  $dS = \sin(\theta)d\theta d\Phi$ . The eigenstrain,  $\varepsilon_{ij}^*(\theta, \Phi)$ , is first calculated in the local fibre coordinate system following the Mori - Tanaka procedure described before and then transformed back into the global coordinate system and finally integrated as shown in equation (6.37).

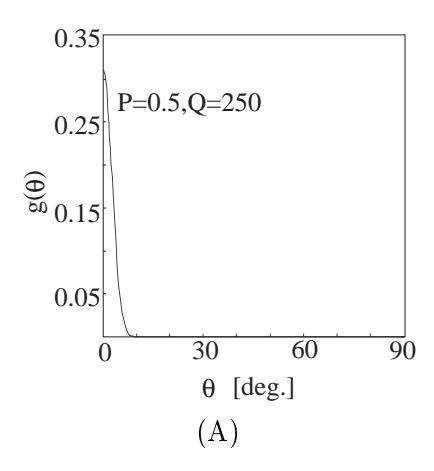
### 6.5 Results

In order to carry out calculations incorporating the effect of weakened interfaces, the interfacial parameter  $\alpha$  needs to be determined. In chapter 4 the interfacial shear strength of the two model systems has been found to be 2.1 MPa for the PP-U specimens and 11 MPa for the PP-MA specimens. This gives a shear strength ratio of  $\approx 0.193$ . To determine the interfacial parameter,  $\alpha$ , the composite - with a fibre distribution as shown in figure 6.5A - and perfect interfacial bonding is subjected to a shear stress  $\sigma_{13}$  and the interfacial shear stress,  $\sigma_{13}^{perf}$  is noted. By "trial and error" the interfacial parameter is now adjusted to a value that gives an interfacial shear stress,  $\sigma_{13}^{weak}$  which is equal to  $0.193 \cdot \sigma_{13}^{perf}$ . Following this procedure the interfacial parameter  $\alpha$  is found to be  $8\times10^{-6}$ , corresponding to an interfacial stiffness of 125 GPa or 83 times stiffer than the matrix. According to Qu [88] the condition for the interface to be slightly weakened is that the compliance of the spring layer is much smaller than that of the matrix or equivalently that the interfacial stiffness is much larger than that of the matrix which is the case in the present situation.

Calculation of the initial composite stiffnesses and composite creep strains with and without a weakened interface have been carried out for various fibre distributions and fibre volume fractions at a temperature corresponding to  $T = 23^{\circ}C$ .

In figure 6.5B the elastic stiffness normalised with respect to matrix modulus is shown for a composite with perfectly aligned fibres, (UD), and for a composite with fibre distribution as shown in figure 6.5A as a function of fibre volume fraction. The UD composite elastic stiffness does not change when  $\alpha \neq 0$ , which is due to the aspect ratio of the fibres. When the fibre aspect ratio is larger than  $\approx 25$  the general expressions for the Eshelby tensor approaches the expressions for an infinitely long fibre, and thus the stiffness will not be affected by weak interfaces. Considering the stiffness of a composite with distributed fibres according to figure 6.5A, the stiffness is only decreased by approximately 6 % compared to the UD composite. When the interface is weakened the stiffness decreases by 5 % compared to the perfect interface and by 11 % compared to the UD composite. Another important aspect to notice is that the stiffness of the UD composite varies linearly with respect to fibre volume fraction, whereas the stiffness for the composite with distributed fibres is slightly nonlinear with respect to fibre volume fraction and this nonlinearity increases when the interface is weakened.

In figure 6.6A the fibre distributions used for calculating the results in figure 6.6B are shown.



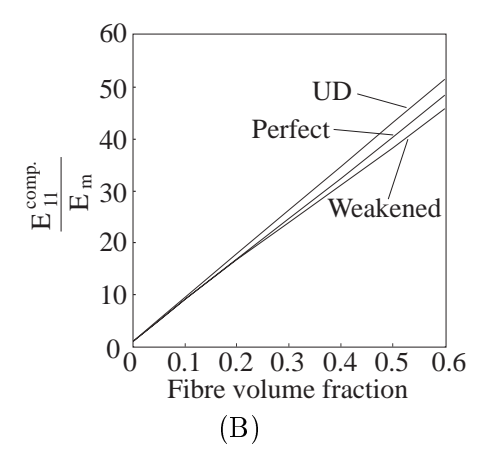
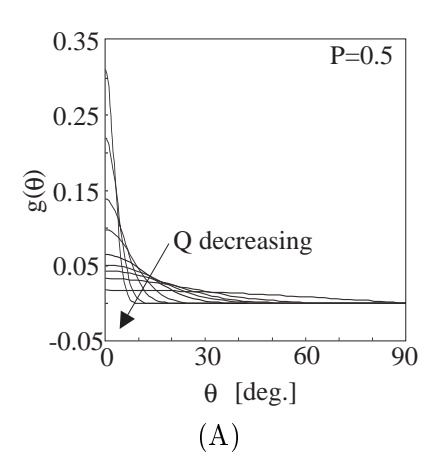


Figure 6.5: A) The distribution function for P = 0.5 and Q = 250, and B) the stiffness - normalised with respect to matrix modulus - in the loading direction.



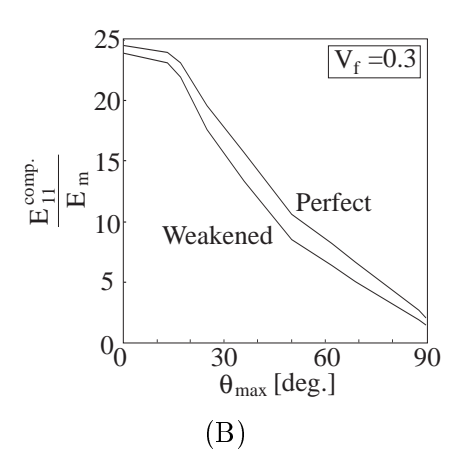


Figure 6.6: A) The distribution functions used in fig. 6.6B), and B) the stiffness normalised with respect to the matrix modulus as a function of  $\theta_{max}$ .

In all these distributions the fibres are distributed within the interval  $[0, \theta_{max}]$  where  $\theta_{max}$  takes on the values  $\theta_{max} = 10^{\circ}$ ,  $20^{\circ}$ ,...,  $90^{\circ}$  by adjusting Q and keeping P constant at P = 0.5. The stiffness normalised with respect to the matrix modulus of a composite with perfect and weakened interface with 30 % fibres is shown in the figure. Comparing the stiffnesses shown in the figure to the UD composite the stiffness is only affected by around 9 % by varying  $\theta_{max}$  from 0 to  $15^{\circ}$ . However, when  $\theta_{max}$  increases further the stiffness decreases drastically. Comparing the two situations shown in the figure it is seen that the largest difference occur for angles in the interval  $30^{\circ} < \theta_{max} < 60^{\circ}$ , which is obvious since the interface is weakened with respect to shear loading. The maximum shear stresses occur at  $45^{\circ}$  to the principal stresses which are in the 11 and the 33 direction, respectively. This means that when  $\theta_{max}$  is in the range  $30^{\circ} < \theta_{max} < 60^{\circ}$  the effect of the weakened interface will be largest.

In the following calculations the fibre distributions shown in figure 6.7 have been used. In figures 6.8, 6.9 and 6.10 the fibre distribution corresponding to P = 0.5 and Q = 11 have been used,

112 6.5. Results

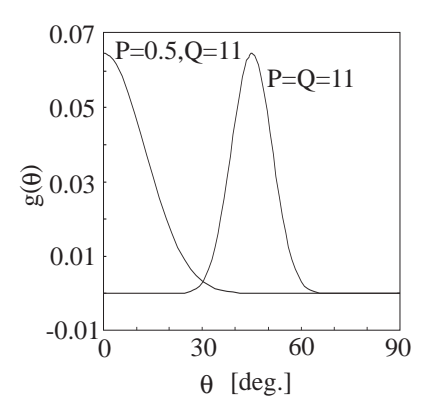
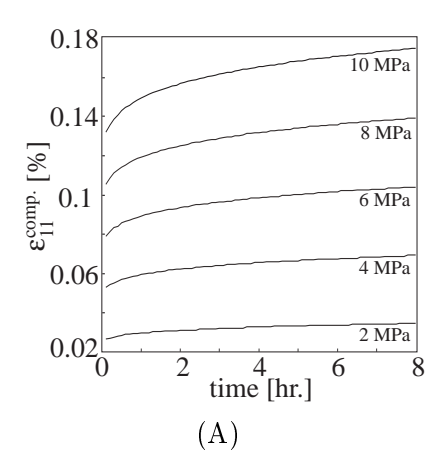


Figure 6.7: The fibre distribution functions for P=Q=11 and P=0.5, Q=11.

whereas both of the distributions shown have been used in the calculations of the results shown in figures 6.11, 6.12 and 6.13. All calculations are carried out for a composite with 30 % fibres and perfect/weakened interfaces.



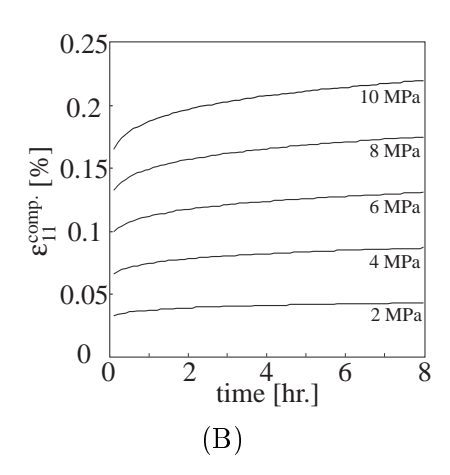
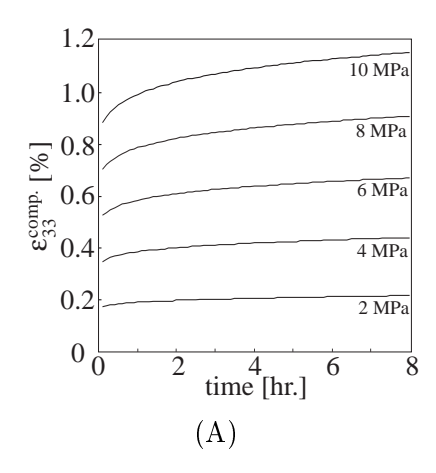


Figure 6.8: The composite creep strains for loads applied in the 11 direction in case of A) perfect interface and B) weakened interface.

In figure 6.8 the composite creep strains are shown for a composite loaded in the 11 direction. The creep strains have been calculated to investigate the effect of the fibres on the nonlinear creep behaviour. The creep strain after 8 hours of the pure matrix at the five load levels are: 0.33 %, 0.71 %, 1.14 %, 1.63 % and 2.2 %, respectively. From the figures it is seen that the fibres are restricting the 8 hour creep strain to less than 10 % of the pure matrix creep strain. Furthermore, it is seen that the composite response is dominated by the fibres since the nonlinear behaviour of the matrix is nearly absent, i.e. the nonlinearity is less than 3 % at  $\sigma = 10$  MPa. The same holds true for the composite creep with a weakened interface. However, the weakened interface causes the creep strains to increase by 25 % at each load level. The degree of nonlinearity is determined by calculating the ratio of creep strain to applied load and checking the deviation from linearity.

In figure 6.9 the composite creep strains are shown for a composite loaded in the 33 direction - transversely to the fibres preferred orientation. The figures show that when the composite - with



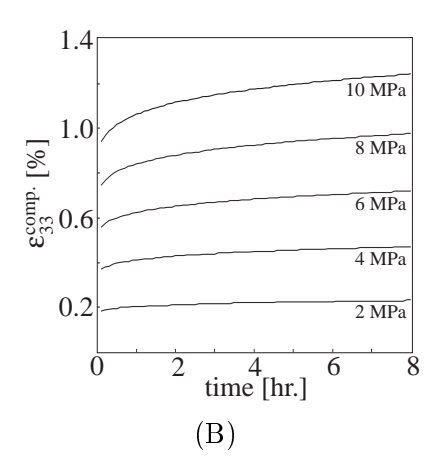
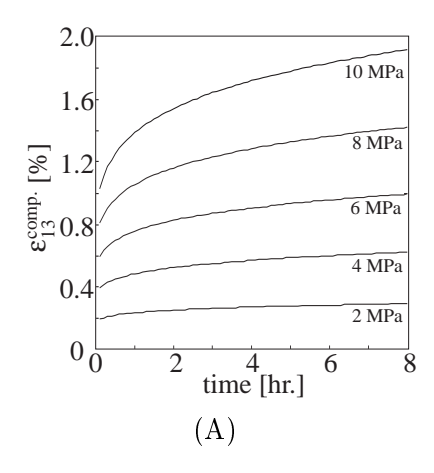


Figure 6.9: The composite creep strains for loads applied in the 33 direction in case of A) perfect interface and B) weakened interface.

this fibre distribution - is loaded transversely the creep strains after 8 hours are now between 50 % and 65 % of that of the pure matrix. The nonlinarity is also showing. At 10 MPa load the nonlinearity is approximately 5 % when the interface is perfect and 6 % when the interface is weakened, respectively. Finally, the creep strain is increased by approximately 7 % when the interface is weakened as compared to the perfect interface. This is quite obvious since there are only very few fibres in the loading direction and thus a weakened interface will have less influence as compared to the previous situation.



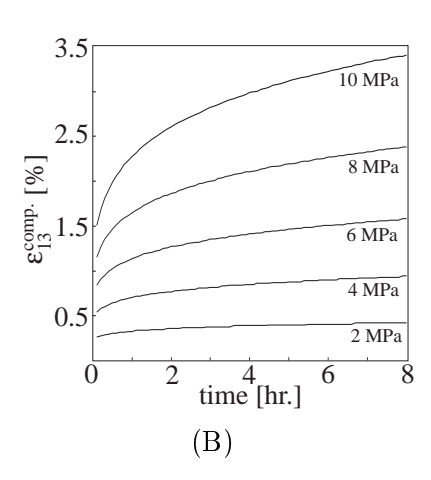


Figure 6.10: The composite creep strains for loads applied in the 13 direction in case of A) perfect interface and B) weakened interface.

In figure 6.10 the composite creep strains are shown for a composite subjected to a shear load,  $\sigma_{13}$ , in the transversely isotropic plane. Now it is clearly seen that the composite viscoelastic behaviour has become nonlinear. The nonlinearity is 27 % when the interface is perfect and 52 % when the interface is weakened. Furthermore, the creep strains are increased by 45 % at 2 MPa to 77 % at 10 MPa, as compared to the creep strain in the composite with perfect interfaces. This is mainly because of the weakened interface, however in the case of a perfect interface the

114 6.5. Results

creep strains are close to that of the pure matrix. This is due to the fibre distribution which is poor regarding shear loading.

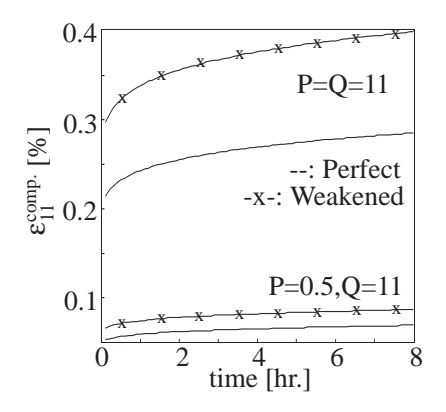


Figure 6.11: The creep strain  $\varepsilon_{11}^{comp}$  is shown for two different fibre distributions with perfect/weakened interfaces. The load is  $\sigma_{11} = 4$  MPa.

In figure 6.11 the composite creep strains are shown for a composite loaded in the 11 direction. Two fibre distributions have been used, corresponding to the two situations shown in figure 6.7. As expected the fibre distribution (P = 0.5, Q = 11) is superior to the other distribution (P = Q = 11). In fact the creep strains are increased by a factor of 4.1 when the interface is perfect and by a factor of 4.5 when the interface is weakened.

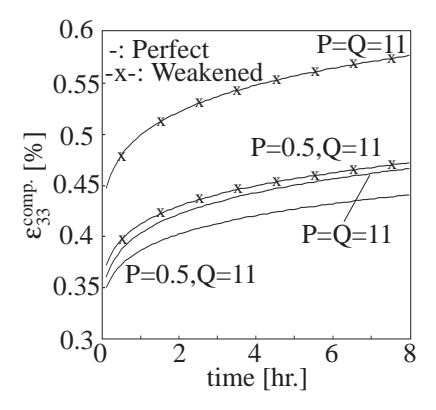


Figure 6.12: The creep strain  $\varepsilon_{33}^{comp}$  is shown for two different fibre distributions with perfect/weakened interfaces. The load is  $\sigma_{33} = 4$  MPa.

In figure 6.12 the composite creep strains are shown for a composite loaded in the 33 direction. The same two fibre distributions as in the previous situation have been used. The behaviour is now quite complicated. The creep strains in the two situations; when the interface is perfect and P = Q = 11 and when the interface is weakened and P = 0.5, Q = 11 are nearly identical. This is due to the fact that the distribution corresponding to P = Q = 11 is not an adequate distribution for load cases other than shear. Finally, as expected, the creep strains are largest

when the interface is weak and P = Q = 11.

In figure 6.13 the composite creep strains are shown for a composite loaded in the 13 direction,

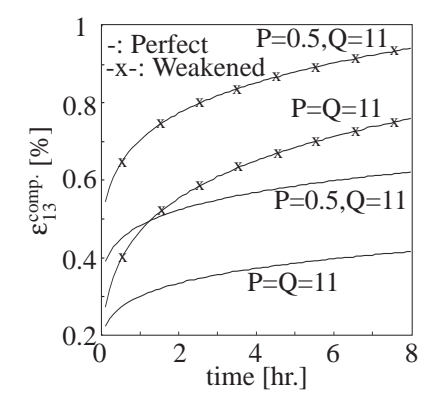


Figure 6.13: The creep strain  $\varepsilon_{13}^{comp}$  is shown for two different fibre distributions with perfect/weakened interfaces. The load is  $\sigma_{13} = 4$  MPa.

corresponding to the transversely isotropic plane and again the same fibre distributions as in the previous two situations have been used. For the perfect interface the distribution corresponding to P=Q=11 is shown to be superior, which is also to be expected considering the discussion in conjunction with figure 6.6. Considering loading times less than 1.3 hours the fibre distribution corresponding to P=Q=11 with a weakened interface shows better creep properties than the other distributions with perfect interfaces. Finally, the situation when the interface is weakened and the fibres are distributed according to P=0.5 and Q=11 shows poor creep properties.

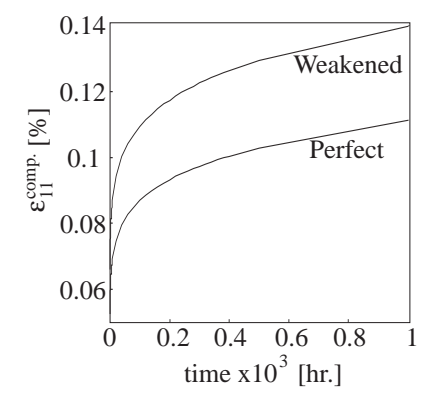


Figure 6.14: The creep strain  $\varepsilon_{11}^{comp.}$  is shown for a fibre distribution according to P=0.5 and Q=11 with perfect/weakened interfaces. The load is  $\sigma_{11}=4$  MPa.

The last figure, 6.14, shows the long term performance of a composite with 30 % fibres distributed according to P=0.5 and Q=11. It is seen that the composite with this fibre distribution displays quite good creep properties even when the interface is weakened the maximum strain after 1000 hours is only 0.14 %, and offers a creep resistance which is 9 times better than that of the pure matrix at 1000 hours. When the interface is perfect the composite is more than 11 times as resistant to creep than the pure matrix.

116 6.6. Summary

### 6.6 Summary

In this chapter the overall creep behaviour of short fibre reinforced composites has been considered. The overall creep modelling is based upon the Mori - Tanaka mean field approach which is extended to incorporate both the effects of weakened interfaces and complex fibre distributions. The weakened interfaces are modelled by introducing a spring layer of vanishing thickness at the interface between the fibre and the matrix. This makes the interfacial tractions continuous, whereas displacements may be dis-continuous, depending on the value of the spring layer compliance. In order not to violate the compatibility requirements the interface is only weakened with respect to shear, i.e. no overlapping of the fibre and matrix can occur, but relative sliding may occur. The interfacial parameter enters the governing equations and thus gives a modified Eshelby tensor for determining the eigenstrains.

The effect of various fibre distributions are taken into account by introducing a fibre distribution function. The eigenstrains are then calculated in the local fibre coordinate system, transformed back into the global coordinate system and averaged over all possible orientations.

The procedure described above enables the calculation of elastic stiffness, creep strain etc. for short fibre composites with and without perfect interfaces and for various fibre distributions.

Calculations have shown that for UD composites the interfacial parameter does not influence the elastic stiffness in the fibre direction. For various fibre distributions the interfacial parameter has a varying effect. The largest influence of weakened interfaces is seen when shear load,  $\sigma_{13}$ , is applied to a composite with a preferred fibre orientation corresponding to the 11 direction.

Results from the present model are presented by Schjødt-Thomsen and Pyrz in [107] since an implementation of a complex fibre orientation into the Mori - Tanaka model has not yet been accomplished.

### Chapter

7

# **Conclusions**

The purpose of the present work is to investigate the load transfer mechanisms between the fibre and matrix in and around a single fibre in short fibre reinforced viscoelastic composites. The basis of this work is experimental investigations using micro Raman spectroscopy. In this work two different model systems have been used. One model system - the PP-U composites - consist of plasma treated fibres embedded in a standard polypropylene matrix. The other model system - the PP-MA composites - are standard surface treated fibres embedded in a polypropylene matrix grafted with maleic-anhydride.

At the present time it is not possible to use MRS for strain measurements in a semi-crystalline polymer. Therefore, two different nonlinear stress/strain analysis methods have been proposed. Both of these are based upon the integration of point forces along the fibre boundary and are capable of taking thermal induced stress/strain into account. In these models the matrix constitutive behaviour is described using the Schapery model. One of these analysis methods uses experimental quantities as input parameters, whereas the other is purely theoretical. Additionally, nonlinear finite element models have been used as analysis tools along with two proposed methods.

Experimental results have been used to determine an interfacial parameter which has been incorporated into an extension of the Mori - Tanaka mean field theory in order to describe the overall creep behaviour of short fibre reinforced composites with weakened fibre/matrix interfaces. Furthermore, a statistical fibre orientation function is used in conjunction with the overall creep model.

In the following some of the most important conclusions of the present work is summarised.

### **Experimental Investigations**

Micro Raman spectroscopy has been used to measure the fibre strain in model composites with one or a few fibres embedded. The test specimens were subjected to different loading histories because the loading itself may affect the load transfer efficiency due to stress relaxation at fibre ends.

To conduct the fibre strain measurements the relation between applied strain and frequency shift was found to be  $-23 \text{ cm}^{-1}/\%$ , which is consistent with values reported in the litterature.

The measured fibre strain in the PP-U composites displayed a linear dependence of the longitudinal fibre coordinate. Furthermore, no significant differences between fibre strain magnitude was observed when subjecting these composites to different load levels. Subjecting the PP-U composites to mechanical conditioning and subsequent creep it was found that the load bearing capability of the fibres diminished. When subjecting these composites to creep and subsequent recovery the fibre recovery strains were drastically increased, compared to the initial residual strains, no matter what the load level. From these experimental results it is obvious that the fibre strains are nearly independent of applied load and it is therefore concluded that the load transfer is of a friction-like nature governed by the initial residual stress and the coefficient of friction between the fibre and matrix. Since the load transfer is of a purely mechanical nature it was expected that the fibre would carry a decreasing amount of load for increasing time, due to relaxation of the initial residual stresses and this was verified experimentally.

The other material combination, the PP-MA composites, displayed a much more efficient load transfer. In fact the initial residual fibre strain carried per millimeter fibre length is 3 times larger than in the PP-U composites. The maximum initial residual fibre strains have been found to be 0.39~% which is close to the compressive fibre fracture strain found by other researchers to be  $0.45~\% \pm 0.05~\%$  for HM PAN based carbon fibres (Courtaulds Grafil HM-standard, [64]). This indicated that the fibre matrix interface in the PP-MA composites is much stronger than the interface in the PP-U composites. The various measurements showed that the initial residual strain has a restricting effect on the fibre creep strain since the fibre creep strain is only just tensile at overall strains of 0.64~%. Even though the measured fibre strains are nonlinear with respect to the fibre longitudinal coordinate a portion of the fibre displayed a linearity in strain with respect to the longitudinal coordinate. This has been attributed to extensive yielding at the interface between the fibre and matrix and is also shown by a nonlinear viscoplastic finite element model. Yielding occurs along approximately half the fibre length and decreases the load transfer efficiency, resulting in the interesting fact that the fibre strain decreases with increasing time.

Model composites with misaligned fibres were subjected creep loading conditions and it was found that the fibre strain decreases with increasing misalignment angle. This is due to two mechanisms. As the misalignment angle increases the effect of the radial pressure on the fibre is reduced and thus decreases the load transferred to the fibre. Secondly, for increasing misalignment angles the Poisson effect of the matrix contributes more and more to the longitudinal fibre strain and when the fibre is orthogonal to the loading direction the fibre experiences compression only.

Preliminary investigations of fibre interaction have been undertaken and it was found that the interaction distance is much smaller than in the elastic case. Furthermore, viscoelastic interaction seems to be very dependent on fibre arrangement, suggesting that viscoelastic interaction is much more complicated than in the elastic case.

SEM micrographs of the two fibre types were recorded in order to see if there were any visual differences in fibre surface morphology which could explain the different load transfer mechanisms. It was found that the plasma treated fibres had a more smooth surface compared to the fibres with the standard surface treatment. This means that the possibility of interpenetration of the matrix into the fibre surface and the degree of mechanical interlocking is reduced when using the plasma treated fibres. This results in the frictional-like load transfer.

Finally, the MRS results were used to calculate the interfacial shear strength of the model composites. The PP-U composites were found to have an interfacial shear strength of 2.1 MPa, whereas the PP-MA composites have an interfacial shear strength of 11 MPa, governed by the shear yield strength of the matrix.

### Theoretical Modelling

Due to the different load transfer mechanisms, two slightly different analysis methods have been proposed. The first is used to model the frictional load transfer. It is used in conjunction with the experimentally measured initial residual fibre strains and a Lamé solution to give the coefficient of friction. The coefficient of friction have been found to be  $\mu_{fric.} = 0.21$ . Comparison between a nonlinear finite element model using a coefficient of friction of 0.2 showed very good agreement. The theoretical method is of a qualitative nature and predicts - in agreement with experiments - that the load transferred to the fibre decreases with increasing time/load due to stress relaxation.

The other stress/strain analysis method is used to model the behaviour of the PP-MA model composites. It is purely theoretical and is based upon Eshelby's thought experiment and an incremental stress/strain formulation. This approach captures the tendencies of the experiments and also predicts tension and compression along the fibre length - at the same time.

The major differences between the calculated results and experimental results are due to the constant interfacial tractions which govern the nature of the interfacial shear stress and thus governs the shape of the longitudinal fibre stress. The difference between the results from this approach and experimental results are also due to the fact that this theoretical method is viscoelastic and not viscoplastic. However, it is believed that the basis of this approach has potential for improvement with respect to taking viscoplasticity into account. This is mainly due to the fact that this approach is much less time consuming compared to the nonlinear FE models.

Results from this analysis method also predict that the initial residual stress may have a beneficial effect on the fibre strains, that is the initial residual stress may prohibit tensile fibre fractures.

The final modelling was concerned with the overall creep of short fibre reinforced composites. The creep of composites with weakened interfaces and "real" fibre orientations were considered. The weakened interfacial stiffness is found to be 83 times the stiffness of the matrix. Calculations for UD composites showed that the weakened interface does not influence the elastic stiffness in the fibre direction. For various fibre distributions the weakened interface has a varying influence, where the largest effect is seen when applying shear load,  $\sigma_{13}$ , to a composite with its preferred fibre orientation in the 11 direction. Generally, it is seen that alignment of the fibres parallel to the loading direction reduces the degree of nonlinearity, i.e. the composite behaves linearly viscoelastic even though the matrix is nonlinear viscoelastic.

#### General Remarks

The present work contributes to the knowledge and understanding of the load transfer mechanisms in short fibre reinforced viscoelastic composites. This work does not represent a complete and final description of the problem but provides information of the tendencies. A complete description also seems unattainable due to the difficulties of obtaining mechanical properties of the fibre/matrix interphase. Furthermore, the calculated results both from the FE models and the two proposed methods are not based upon an interphase being present between the fibre and matrix. However, that may be taken into account in the two models through an iterative interaction procedure.

### Future Work

Further extension of the work presented in this report is reasonable since almost all mechanical properties are dependent on the interphase/interface properties which affect the load transfer. As

a consequence the theoretical methods proposed here need to consider this aspect. Furthermore, the experimental programme must also be directed towards determining interfacial properties and this may not be restricted to only considering the fragmentation test since this test is not fully understood.

Another interesting technique which may be used to gain more quantitative knowledge of the fibre surface morphology is atomic force microscopy.

The overall creep behaviour was considered theoretically but the next step will obviously be to measure fibre strains in real composites in order to correlate experimental values with theoretical predictions. This is especially necessary because the poor load transfer in the PP-U composites may show it to be more efficient in a real composite due to the interaction between fibres and the very complicated stress field.

- [1] Aboudi, J., "Mechanics of composite materials: A unified micromechanical approach". Elsevier, Studies in applied mechanics, 1991.
- [2] Argon, A. S., "Stresses in and around slender elastic rods and platelets of different modulus in an infinite elastic medium under uniform strain at infinity". Fibre Sci. Tech., 1976, 9, pp. 265-275.
- [3] Baillie, C. A. & Bader, M. G., "Strength studies of single carbon fibres in model composite fragmentation tests". *Composites*, 1994, **25**, No. 6, pp. 401-406.
- [4] Batchelder, D. N. & Bloor, D., "Strain dependence of the vibrational modes of a diacetylene crystal". J. Polym. Sci., 1979, 17, pp. 569-581.
- [5] Benveniste, Y., "The effective mechanical behaviour of composite materials with imperfect contact between the constituents". *Mech. Mater.*, 1985, 4, pp. 197-208.
- [6] Benveniste, Y., Dvorak, G. J. & Chen, T., "Stress fields in composites with coated inclusions". Mech. Mater., 1989, 7, pp. 305-317.
- [7] Biot, M. A., "Theory of stress-strain relations in anisotropic viscoelasticity and relaxation phenomena". J. Appl. Phys., 1954, 25, No. 11, pp. 1385-1391.
- [8] Bogoeva Gaceva, G., Mäder, E., Haüssler, L., & Dekanski, A., "Characterization of the surface and interphase of plasma-treated HM carbon fibres". Composites Part A, 1997, 28 A, pp. 445-452.
- [9] Bower, D. I., Lewis, E. L. V. & Ward, I. M., "Relationships among stress-induced Raman shifts for isotropic and uniaxially oriented polymers". *Polymer*, 1995, 36, No. 18, pp. 3473-3477.
- [10] Bozarth, J. M., Gillespie, J. W. & McCullough, R. L., "Fiber orientation and its effect upon thermoelastic properties of short carbon fiber reinforced poly(etheretherketone) (PEEK)". Polym. Comp., 1987, 8, No. 2, pp. 74-81.
- [11] Brüeller, O. S., "On the non-linear characterization of the long term behavior of polymeric materials". *Polym. Engn. Sci.*, 1987, **27**, No. 2, pp. 144-148.
- [12] Chawla, K. K., "Composite Materials, Science and Engineering". Springer-Verlag, 1987.
- [13] Chen, T., Dvorak, G. J. & Benveniste Y., "Stress fields in composites reinforced by coated cylindrically orthotropic fibres". *Mech. Mater.*, 1990, **9**, pp. 17-32.
- [14] Chen, T., Dvorak, G. J. & Benveniste, Y., "Mori Tanaka estimates of the overall elastic moduli of certain composite materials". J. Appl. Mech., 1992, 59, pp. 539-546.

[15] Chohan, V. & Galiotis, C., "Interfacial measurements and fracture characteristics of 2D microcomposites using remote laser Raman microscopy". Composites Part A, 1996, 27A, pp. 881-888.

- [16] Chou, T. W., Nomura, S. & Taya, M., "A self consistent approach to the elastic stiffness of short-fiber composites". J. Comp. Mater., 1980, 14, pp. 178-188.
- [17] Christensen, R. M., "Theory of viscoelasticity. An introduction". 1971, Academic Press, New york.
- [18] Cox, H. L., "The elasticity and strength of papers and other fibrous materials". Brit. J. Appl. Phys., 1952, 3, No. 1, pp. 72-79.
- [19] Day, R. J. & Young, R. J., "Raman microscopy of fibres and composites". J. Microscopy, 1993, 169, pp.155-161.
- [20] Dollar, A. & Steif, P. S., "Load transfer in composites with Coulomb friction interface". Int. J. Solids Structures, 1988, 24, No. 8, pp. 789-803.
- [21] Drzal, L. T., Rich, M. J., & Lloyd, P. F., "Adhesion of graphite fibers to epoxy matrices: I. The role of fiber surface treatment", J. Adhesion, 1982, 16, pp. 1-30.
- [22] Dvorak, G. J. & Benveniste Y., "On the thermomechanics of composites with imperfectly bonded interfaces and damage". *Int. J. Solids Structures*, 1992, **29**, No. 23, pp. 2907-2919.
- [23] Engineered Materials Handbook. Vol. 1, "Composites", 1987, ASM International.
- [24] Eshelby, J. D., "The determination of the elastic field of an ellipsoidal inclusion, and related problems". *Proc. Roy. Soc.*, 1957, **A241**, pp. 376-396.
- [25] Fan, C. F. & Hsu, S. L., "A study of stress distribution in model composites by using finite-element analysis. I. End effects". J. Polym. Sci., Part B, Polym. Phys., 1992, 30, pp. 603-618.
- [26] Feillard, P., Desarmot, G. & Favre, J. P., "Theoretical aspects of the fragmentation test". Comp. Sci. Tech., 1994, **50**, pp. 265-279.
- [27] Folkes, M. J., "Interfacial crystallization of polypropylene composites". In "Polypropylene: Structure, blends and composites", Ed. J. Karger-Kocsis, 1995, Chapman & Hall.
- [28] Fukuda, H. & Kawata, K., "Stress and strain fields in short fibre-reinforced composites". Fibre Sci. Tech., 1974, 7, pp. 129-156.
- [29] Galiotis, C., "A study of mechanisms of stress transfer in continuous and discontinuous fibre model composites by laser Raman spectroscopy". Comp. Sci. Tech., 1993, 48, pp. 15-28.
- [30] Galiotis, C. & Batchelder, D. N., "Strain dependence of the first- and second-order Raman spectra of carbon fibres". J. Mat. Sci. Lett., 1988, 7, pp. 545-547.
- [31] Galiotis, C., Robinson, I. M., Young, R. J., Smith, B. J. E. & Batchelder, D. N., "Strain dependence of the Raman frequencies of a Kevlar 49 fibre". *Polym. Comm.*, 1985, **26**, No. 12, pp. 354-355.
- [32] Gamstedt, E. K., "Fatigue damage mechanisms in polymer matrix composites". Ph.D Thesis, Luleaa University of Technology, 1997. ISSN 1402-1544.
- [33] Goto, S. & McLean, M., "Role of interfaces in creep of fibre-reinforced metal-matrix composites II, Short fibres". *Acta Metall. Mater.*, 1991, **39**, No. 2, pp. 165-177.

- [34] Green, A. E. & Rivlin, R. S., "The mechanics of non-linear materials with memory". Arch. Rat. Mech. Anal., 1957/58, 1, pp. 1-21.
- [35] Grubb, D. T., Li, Z. F. & Phoenix, S. L., "Experimental studies of fiber interactions with multi-fiber model composites". *Proc. of The American Society for Composites*, 1994. pp. 592-601.
- [36] Grubb, D. T. & Li, Z. F., "Molecular stress distribution and creep of high-modulus polyethylene fibres". *Polymer*, 1992, **33**, No. 12, 2587-2597.
- [37] Guild, F. J., Vlattas, C. & Galiotis, C., "Modelling of stress transfer in fibre composites". Comp. Sci. Tech., 1994, 50, pp. 319-332.
- [38] Hashin, Z. & Shtrikman, S., "A variational approach to the theory of the elastic behaviour of multiphase materials". J. Mech. Phys. Solids, 1963, 11, pp. 127-140.
- [39] Hiel, C., "The nonlinear viscoelastic response of resin matrix composite laminates", Blacks-burg report, VPI-E-83-6, March 1983.
- [40] Hill, R., "Continuum micromechanics of elastoplastic polycrystals". J. Mech. Phys. Solids, 1965, 13, pp. 89-101.
- [41] Hollas, J. M., "Modern Spectroscopy". 3. Ed., John Wiley and Sons.
- [42] Huang, Y. & Young, R. J., "Analysis of the fragmentation test for carbon fibre/epoxy model composites by means of Raman spectroscopy". Comp. Sci. Tech., 1994, **52**, pp. 505-517.
- [43] Huang, Y. & Young, R. J., "Interfacial behaviour in high temperature cured carbon fibre/epoxy resin model composite". *Composites*, 1995, **26**, No. 8, pp. 541-550.
- [44] Huang, Y. & Young, R. J., "Effect of fibre microstructure upon the modulus of PAN- and PITCH-based carbon fibres". Carbon, 1995, 33, No. 2, pp. 97-107.
- [45] Hu, X., Stanford, J. L. & Young, R. J., "Strain measurement and deformation analysis in a diacetylene containing urethane copolymer using Raman spectroscopy". *Polymer*, 1994, **35**, No. 1, pp. 80-85.
- [46] Hui, C. Y., Phoenix, S. L., Ibnabdeljalil, M. & Smith, R. L., "An exact closed form solution for fragmentation of Weibull fibers in a single filament composite with applications to fiberreinforced ceramics". J. Mech. Phys. Solids, 1995, 43, No. 10, pp. 1551-1585.
- [47] Jang, B., Liu, C. W., Wang, C. Z. & Shih, W. K., "Mechanical properties and morphology of crystalline polymers and their continuous fiber composites". *J. Thermoplastic Comp. Mater.*, 1988, 1, pp. 242-276.
- [48] Jang, B. Z., In "Polypropylene: Structures, blends and composites". 1995, 3, Ed. J. Karger-Kocsis, pp. 330-339.
- [49] Kelly, A. & Tyson, W. R., "Tensile properties of fiber-reinforced metals: Copper/Tungsten and Copper/Molybdenum". J. Mech. Phys. Solids, 1965, 13, pp. 329-350.
- [50] Keresztury, G. & Földes, E., "On the Raman spectroscopic determination of phase distribution in polyethylene". *Polym. Testing*, 1990, **9**, pp. 329-339.
- [51] Lacroix, T., Tilmans, B., Keunings, R., Desaeger, M. & Verpoest, I., "Modelling of critical fibre length and interfacial debonding in the fragmentation testing of polymer composites". *Comp. Sci. Tech.*, 1992, 43, pp. 379-387.

[52] Lacroix, T., Keunings, R., Desaeger, M. & Verpoest, I., "A new data reduction scheme for the fragmentation testing of polymer composites". J. Mat. Sci., 1995, 30, pp. 683-692.

- [53] Di Landro, L. & Pegoraro, M., "Evaluation of residual stresses and adhesion in polymer composites". *Composites Part A*, 1996, **27 A**, pp. 847-853.
- [54] Lewis, E. L. V., Bower, D. I. & Ward, I. M., "Stress-induced shifts and intensity changes in the 1616 cm<sup>-1</sup> Raman line for isotropic and uniaxially oriented poly(ethyleneterephthalate)". *Polymer*, 1995, **36**, No. 25, pp. 4741-4752.
- [55] Lienkamp, M. & Schwartz, P., "A Monte Carlo simulation of the failure of a seven fiber microcomposite". *Comp. Sci. Tech.*, 1993, **46**, pp. 139-146.
- [56] Lin, C. W., "Modification of polypropylene by peroxide-catalysed grafting of maleic anhydride for adhesive bonding: surface and interface". J. Mat. Sci. Lett., 1993, 12, pp. 612-614.
- [57] Lin, T. H., Yu, C. L. & Weng, G. J., "Derivation of polycrystal creep properties from the creep data of single crystals". J. Appl. Mech., 1977, 44, pp. 73-78.
- [58] Lockett, F. J., "Nonlinear Viscoelastic Solids", Academic Press, 1972.
- [59] Long, D. A., "Raman Spectroscopy", McGraw-Hill International Book Company, 1977.
- [60] Lou, Y. C. & Schapery, R. A., "Viscoelastic characterization of a non-linear fiber-reinforced plastic". J. Comp. Mater., 1971, 5, pp. 208-234.
- [61] Mann, N. R., Schafer, R. E. & Singpurwalla, N. D., "Methods for statistical analysis of reliability and life data", John Wiley & Sons, 1974, Wiley Series in probability and mathematical statistics.
- [62] Maekawa, Z. I., Hamada, H. & Yokoyama A., "Lamination theory of composite material with complex fiber orientation distribution". *In Proc. of ICCS* 5, 1989, pp. 701-714.
- [63] McCartney, L. N., "New theoretical model of stress transfer between fibre and matrix in a uniaxially fibre-reinforced composite". *Proc. R. Soc. Lond.*, 1989, A425, pp. 215-244.
- [64] Melanitis, N. & Galiotis, C., "Compressional behaviour of carbon fibres, Part 1: A Raman spectroscopic study". J. Mater. Sci., 1990, 25, pp. 5081-5090.
- [65] Melanitis, N. & Galiotis, C., "Interfacial micromechanics in model composites using laser Raman spectroscopy". *Proc. R. Soc. Lond. A.*, 1993, **440**, pp. 379-398.
- [66] Melanitis, N., Galiotis, C., Tetlow, P. L. & Davies, C. K. L., "Monitoring the micromechanics of reinforcement in carbon/epoxy resin systems". J. Mat. Sci., 1993, 28, pp. 1648-1654.
- [67] Mermet, A., Duval, E., Etienne, S. & G'Sell, S., "Effect of plastic deformation on the nanostructure of polycarbonate: study by low-frequency Raman scattering". *Polymer*, 1996, **37**, No. 4, pp. 615-623.
- [68] Mori, T. & Tanaka, K., "Average stress in matrix and average elastic energy of materials with misfitting inclusions". Acta Metall., 1973, 21, pp. 571-574.
- [69] Mura, T., "Micromechanics of defects in solids", 2nd Ed., 1993, Kluwer Academic Publishers, Mechanics of elastic and inelastic solids.
- [70] Nairn, J. A., "A variational mechanics analysis of the stresses around fibre breaks in embedded fibres". *Mech. Mater.*, 1992, **13**, pp. 131-154.

- [71] Nairn, J. A. & Liu. Y. C., "Stress transfer into a fragmented anisotropic fiber through an imperfect interface". *Int. J. Solids Structures*, 1997, **34**, No. 10, pp. 1255-1281.
- [72] Nemat-Nasser, S. & Hori, M., "Micromechanics: Overall properties of heterogeneous materials", 1993, North-Holland, Applied mathematics and mechanics.
- [73] Nielsen, A. S., "Micromechanical modelling of thermal stresses in polymer matrix composites based on Raman microscopy"., Ph.D Thesis, Aalborg University, In prep.
- [74] Nielsen, A. S. & Pyrz, R., "The effect of cooling rate on thermal residual strains in carbon/polypropylene microcomposites". Sci. Engn. Comp. Mater., 1998, 7, Nos. 1-2, pp 1-22.
- [75] Nielsen, A. S., Schjødt-Thomsen, J. & Pyrz, R., "Matrix strain field mapping around embedded fibres using polarised Raman microscopy". In *Proc. 12th. Int. Conf. Composite Mater*, (ICCM-12), July 1999, Paris, France.
- [76] Pachalis, J. R. & Chou, T. W., "Modelling of creep of misaligned short-fiber reinforced ceramic composites". J. Appl. Mech., 1992, 59, pp. 27-32.
- [77] Pagano, N. J. & Tandon, G. P., "Thermo-elastic model for multidirectional coated fiber composites: traction formulation". *Comp. Sci. Tech.*, 1990, **38**, pp. 247-269.
- [78] Pagano, N. J. & Tandon, G. P., "Modelling of imperfect bonding in fiber reinforced brittle matrix composites". *Mech. Mater.*, 1990, **9**, pp. 49-64.
- [79] Paipetis, A. & Galiotis, C., "Effect of fibre sizing on the stress transfer efficiency in carbon/epoxy model composites". Composites Part A, 1996, 27 A, pp. 755-767.
- [80] Piggott, M. R., "A new model for interface failure in fibre reinforced polymers". Comp. Sci. Tech., 1995, 55, pp. 269-276.
- [81] Piggott, M. R., "Why the fibre/polymer interface can appear to be stronger than the polymer matrix". Comp. Sci. Tech., 1997, 57, pp. 853-857.
- [82] Piggott, M. R., "The effect of interface/interphase on fiber composite properties". *Polym. Comp.*, 1987, **8**, No. 5, pp. 291-297.
- [83] Piggott, M. R., "Expressions governing the stress-strain curves in short fibre reinforced polymers". J. Mater. Sci., 1978, 13, pp. 1709-1716.
- [84] Piggott, M. R., "Why interface testing by single-fibre methods can be misleading". Comp. Sci. Tech., 1997, 57, pp. 965-974.
- [85] Pipes, R. B., McCullough, R. L. & Taggart, D. G., "Behavior of discontinuous fiber composites: Fiber orientation". *Polym. Comp.*, 1982, **3**, No. 1, pp. 34-39.
- [86] Pipkin, A. C. & Rogers, T. G., "A non-linear integral representation for viscoelastic behaviour". J. Mech. Phys. Solids, 1968, 16, No. pp. 59-72.
- [87] Pyrz, R., "Inelastic constitutive modelling and microstructure characterization of composites with continuous fibres"., Doctor Technices thesis. February 1995, Institute of Mechanical Engineering, Aalborg University.
- [88] Qu, J., "Eshelby tensor for an elastic inclusion with slightly weakened interface". J. Appl. Mech., 1993, **60**, pp. 1048-1050.
- [89] Qu, J., "The effect of slightly weakened interfaces on the overall elastic properties of composite materials". *Mech. Mater.*, 1993, 14, pp. 269-281.

[90] Raman, C. V. & Krishnan, K. S., "A new type of secondary radiation". Nature, 1928, 121, No. 3048, pp. 501-502.

- [91] Raman, C. V. & Krishnan, K. S., "A change of wave-length in light scattering". *Nature*, 1928, **121**, No. 3051, pp. 619.
- [92] Robinson, I. M., Zakikhani, M., Day, R. J., Young, R. J. & Galiotis, C., "Strain dependence of the Raman frequencies for different types of carbon fibres". *J. Mater. Sci. Lett.*, 1987, No. 6, pp. 1212-1214.
- [93] Rodriguez-Cabello, J. C., Merino, J. C., Jawhari, T. & Pastor, J. M., "Rheo-optical Raman study of chain deformation in uniaxially stretched bulk polyethylene". *Polymer*, 1995, **36**, No. 22, pp. 4233-4238.
- [94] De Roover, B., Sclavons, M., Carlier, V., Devaux, J., Legras, R. & Momtaz, A., "Molecular characterization of maleic anhydride-functionalized polypropylene". *J. Polym. Sci.*, Part A, 1995, **33**, pp. 829-842.
- [95] Schadler, L. S., Amer, M. S. & Iskandarani, B., "Experimental measurement of fiber/fiber interaction using micro Raman spectroscopy". *Mech. Mater.*, 1996, **23**, pp. 205-216.
- [96] Schadler, L. S. & Galiotis, C., "Fundamentals and applications of micro Raman spectroscopy to strain measurements in fibre reinforced composites". *Int. Mat. Rev.*, 1995, **40**, No. 3, pp. 116-134.
- [97] Schadler, L. S., Laird, C., & Figueroa, J. C., "Interphase behaviour in graphite thermoplastic monofilament composites, Part I, Monotonic loading". *J. Mater. Sci.*, 1992, **27**, No. 15, pp. 4024-4034.
- [98] Schaffer, B. G. & Adams, D. F., "Nonlinear viscoelastic analysis of a unidirectional composite material". J. Appl. Mech., 1981, 48, pp. 859-865.
- [99] Schapery, R. A., "Application of thermodynamics to thermomechanical fracture and bire-fringent phenomena in viscoelastic media". J. Appl. Phys., 1964, 35, No. 5, pp. 1451-1465.
- [100] Schapery, R. A., "A theory of non-linear thermoviscoelasticity based on irreversible thermodynamics". Proc. 5th U. S. Nat. Cong. Appl. Mech., ASME, 1966, pp. 511-530.
- [101] Schapery, R. A., "On a thermodynamic constitutive theory and its application to various nonlinear materials.". *Proc. IUTAM Symp. on Thermoinelasticity*, 1968, Springer-Verlag, pp. 259-285.
- [102] Schapery, R. A., "On the characterization of nonlinear viscoelastic materials". *Polym. Engn. Sci.*, 1969, **9**, No. 4, pp. 295-310.
- [103] Schjødt-Thomsen, J. & Pyrz, R., "Influence of interphase and repeated loading on creep strains and recovery strains using micro Raman spectroscopy". To appear in the ICCI-VII issue of *Composite Interfaces*.
- [104] Schjødt-Thomsen, J. & Pyrz, R., "Creep of carbon/polypropylene model composites a Raman spectroscopic investigation". Comp. Sci. Tech., 1999, **59**, No. 9, pp. 1375-1385.
- [105] Schjødt-Thomsen, J. & Pyrz, R., "Influence of thermally induced strains on subsequent creep loading using micro Raman spectroscopy". In *Proc. 12th. Int. Conf. Comp. Mater.*, (ICCM-12), July 1999, Paris, France.

- [106] Schjødt-Thomsen, J. & Pyrz, R., "Non-linear creep modelling of short single fibre model composites", Submitted to *Comp. Sci. Tech.*
- [107] Schjødt-Thomsen, J. & Pyrz, R., "Overall creep modelling of short fibre reinforced composites with weakened interfaces and complex fibre orientation distributions", Submitted to *Mech. Mater.*
- [108] Sengonul, A. & Wilding, M. A., "Modelling of the time dependence in ultra-high-modulus polyethylene based on Raman microscopy". *Polymer*, 1995, **36**, No. 23, pp. 4379-4384.
- [109] Song, Y., Bao, G. & Hui, C. Y., "On creep of unidirectional fiber composites with fiber damage". Acta Metall. Mater., 1995, 43, No. 7, pp. 2615-2623.
- [110] Structural Research and Analysis Group, "COSMOS/M Finite Element Analysis System". Advanced modules manual. February 1996, Vol. 4, (NSTAR).
- [111] Sørensen, N. J., "Mikromekanisk modellering af krybning i metal-matrix kompositter". Ph.D Thesis (in Danish), DCAMM Report S62 January 1993.
- [112] Takao, Y., Chou, T. W. & Taya, M., "Effective longitudinal Young's modulus of misoriented short fiber composites". J. Appl. Mech., 1982, 49, pp. 536-540.
- [113] Timoshenko, S. P., "Theory of Elasticity", Third Edition, 1970, McGraw Hill International Editions.
- [114] Tripathi, D., Chen, F., & Jones, F. R., "The effect of matrix plasticity on the stress fields in a single filament composite and the value of interfacial shear strength obtained from the fragmentation test". *Proc. R. Soc. Lond. A*, 1996, **452**, pp. 621-653.
- [115] Varna, J., Joffe, R. & Berglund, L. A., "Interfacial toughness evaluation from the single-fiber fragmentation test". *Comp. Sci. Tech.*, 1996, **56**, pp. 1105-1109.
- [116] Walpole, L. J., "On the overall elastic moduli of composite materials". J. Mech. Phys. Solids, 1969, 17, pp. 235-251.
- [117] Wagner, H. D., Amer, M. S. & Schadler, L. S., "Fibre interactions in two-dimensional composites by micro-Raman spectroscopy". J. Mater. Sci., 1996, 31, pp. 1165-1173.
- [118] Wagner, H. D., Wood, J. R. & Marom, G., "Clarifying the application of Weibull statistics for determining the stress state of a fibre from fragmentation tests". *Adv. Comp. Lett.*, 1993, 2.
- [119] Wang, Y. M. & Weng, G. J., "Transient creep of a fiber reinforced metal matrix composite under transverse loading". J. Eng. Mater. Tech., 1992, 114, pp. 237-244.
- [120] Wang, Y. M. & Weng, G. J., "The influence of inclusion shape on the overall viscoelastic behavior of composites". J. Appl. Mech., 1992, 59, pp. 510-518.
- [121] Wang, Y. R. & Chou, T. W., "Analytical modelling of creep behavior of short fibre reinforced ceramic matrix composites". J. Comp. Mater., 1992, 26, No. 9, pp. 1269-1286.
- [122] Weibull, W., "A statistical distribution function of wide applicability". J. Appl. Mech., 1951, 18, pp. 293-297.
- [123] Weng, G. J., "A self consistent scheme for the relaxation of metals". J. Appl. Mech., 1981, 48, pp. 779-784.

[124] Weng, G. J., "A physically consistent method for the prediction of creep behaviour of metals". J. Appl. Mech., 1979, 46, pp. 800-804.

- [125] Whitney, J. M. & Drzal, L. T., "Axisymmetric stress distribution around an isolated fiber fragment". *Toughened Composites*, ASTM STP 937, 1987, Ed. N. J. Johnston, American Society for Testing and Materials, pp. 179-196.
- [126] Wood, J. R., Wagner, H. D. & Marom, G., "A model for compressive fragmentation". Adv. Comp. Lett., 1994, 3, No. 4, pp. 133-138.
- [127] Wood, J. R., Huang, Y., Young, R. J. & Marom, G., "Measurement of thermal strains during compressive fragmentation in single fibre composites by Raman spectroscopy". Comp. Sci. Tech., 1995, 55, pp. 223-229.
- [128] Wu, W., Desaeger, M., Verpoest, I & Varna, J., "An improved analysis of the stresses in a single fibre fragmentation test: I. Two-phase model". *Comp. Sci. Tech.*, 1997, **57**, pp. 809-819.
- [129] Wu, W., Verpoest, I. & Varna, J., "An improved analysis of the stresses in a single fibre fragmentation test: II. 3-phase model". *Comp. Sci. Tech.*, 1998, **58**, pp. 41-50.
- [130] Xanthos, M., "Interfacial agents for multiphase polymer systems: Recent advances". *Polym. Eng. Sci.*, November 1988, **28**, No. 21, pp. 1392-1400.
- [131] Xinran, X., "Viscoelastic characterization of thermoplastic matrix composites" Doctoral Thesis, Free University of Brussels, November 1987.
- [132] Young, R. J., Lu, D. & Day, R. J., "Raman spectroscopy of kevlar fibres during deformation caveat emptor". *Polym. Int.*, 1991, **24**, pp. 71-76.
- [133] Young, R. J. & Yeh, W. Y., "Chain stretching in a poly(ethyleneterephthalate) fibre". Polymer, 1994, 35, No. 18, pp. 3844-3847.
- [134] Young, R. J., "Monitoring deformation processes in high-performance fibres using Raman spectroscopy". J. Text. Inst., 1995, 85, No. 2, pp. 360-381.
- [135] Young, R. J., Personal communications with RJY during his visit to Aalborg University in February 1999.
- [136] Zhu, Z. G. & Weng, G. J., "Creep anisotropy of metal matrix composites containing dilute concentration of aligned spheroidal inclusions". *Mech. Mater.*, 1990, **9**, pp. 93-105.

# **APPENDICES**

### **Appendix**

# $\mathbf{A}$

### Stresses Due to a Point Force

The stresses due to a pointforce are obtained by the well known expressions given by Timoshenko [113], here rewritten for cartesian coordinates.

The stresses due to the interfacial shear stress are

$$\sigma_x^{(2)}(x,y) = \frac{1}{4\pi} \int_0^{l_f/2} \tau_i(\xi) \left[ \frac{(x-x_1)}{(x-x_1)^2 + (y-y_1)^2} \right] \times \left\{ -(3+\nu) + 2(1+\nu) \frac{(y-y_1)^2}{(x-x_1)^2 + (y-y_1)^2} \right\} + \frac{(x-x_1)}{(x-x_1)^2 + (y-y_2)^2} \times \left\{ -(3+\nu) + 2(1+\nu) \frac{(y-y_2)^2}{(x-x_1)^2 + (y-y_2)^2} \right\} - \frac{(x-x_2)}{(x-x_2)^2 + (y-y_1)^2} \times \left\{ -(3+\nu) + 2(1+\nu) \frac{(y-y_1)^2}{(x-x_2)^2 + (y-y_1)^2} \right\} - \frac{(x-x_2)}{(x-x_2)^2 + (y-y_2)^2} \times \left\{ -(3+\nu) + 2(1+\nu) \frac{(y-y_2)^2}{(x-x_2)^2 + (y-y_2)^2} \right\} \right] d\xi$$
(A.1)

$$\sigma_y^{(2)}(x,y) = \frac{1}{4\pi} \int_0^{l_f/2} \tau_i(\xi) \left[ \frac{(x-x_1)}{(x-x_1)^2 + (y-y_1)^2} \right] \times \left\{ (1-\nu) - 2(1+\nu) \frac{(y-y_1)^2}{(x-x_1)^2 + (y-y_1)^2} \right\} + \frac{(x-x_1)}{(x-x_1)^2 + (y-y_2)^2} \times \left\{ (1-\nu) - 2(1+\nu) \frac{(y-y_2)^2}{(x-x_1)^2 + (y-y_2)^2} \right\} - \frac{(x-x_2)}{(x-x_2)^2 + (y-y_1)^2} \times \left\{ (1-\nu) - 2(1+\nu) \frac{(y-y_1)^2}{(x-x_2)^2 + (y-y_1)^2} \right\} - \frac{(x-x_2)}{(x-x_2)^2 + (y-y_2)^2} \times \left\{ (1-\nu) - 2(1+\nu) \frac{(y-y_2)^2}{(x-x_2)^2 + (y-y_2)^2} \right\} d\xi$$
(A.2)

$$\tau_{xy}^{(2)}(x,y) = -\frac{1}{4\pi} \int_{0}^{l_f/2} \tau_i(\xi) \left[ \frac{(y-y_1)}{(x-x_1)^2 + (y-y_1)^2} \right] \times \left\{ (1-\nu) + 2(1+\nu) \frac{(x-x_1)^2}{(x-x_1)^2 + (y-y_1)^2} \right\} + \frac{(y-y_2)}{(x-x_1)^2 + (y-y_2)^2} \times \left\{ (1-\nu) + 2(1+\nu) \frac{(x-x_1)^2}{(x-x_1)^2 + (y-y_2)^2} \right\} - \frac{(y-y_1)}{(x-x_2)^2 + (y-y_1)^2} \times \left\{ (1-\nu) + 2(1+\nu) \frac{(x-x_2)^2}{(x-x_2)^2 + (y-y_1)^2} \right\} - \frac{(y-y_2)}{(x-x_2)^2 + (y-y_2)^2} \times \left\{ (1-\nu) + 2(1+\nu) \frac{(x-x_2)^2}{(x-x_2)^2 + (y-y_2)^2} \right\} d\xi$$
(A.3)

where  $x_1, x_2, y_1$  and  $y_2$  are given by

$$x_1 = x_0 + \xi$$

$$x_2 = x_0 - \xi$$

$$y_1 = y_0 + d_f/2$$

$$y_2 = y_0 - d_f/2$$

The stresses due to the transverse normal tractions are

$$\sigma_x^{(3)}(x,y) = \frac{1}{4\pi} \int_0^{l_f/2} \sigma^*(\eta) \left[ \frac{(y-y_3)}{(x-x_3)^2 + (y-y_3)^2} \right] \times \left\{ -(3+\nu) + 2(1+\nu) \frac{(x-x_3)^2}{(x-x_3)^2 + (y-y_3)^2} \right\} + \frac{(y-y_3)}{(x-x_3)^2 + (y-y_4)^2} \times \left\{ -(3+\nu) + 2(1+\nu) \frac{(x-x_4)^2}{(x-x_3)^2 + (y-y_4)^2} \right\} - \frac{(y-y_4)}{(x-x_4)^2 + (y-y_3)^2} \times \left\{ -(3+\nu) + 2(1+\nu) \frac{(x-x_3)^2}{(x-x_4)^2 + (y-y_3)^2} \right\} - \frac{(y-y_4)}{(x-x_4)^2 + (y-y_4)^2} \times \left\{ -(3+\nu) + 2(1+\nu) \frac{(x-x_4)^2}{(x-x_4)^2 + (y-y_4)^2} \right\} \right] d\eta$$
(A.4)

$$\sigma_y^{(3)}(x,y) = \frac{1}{4\pi} \int_0^{l_f/2} \sigma^*(\eta) \left[ \frac{(y-y_3)}{(x-x_3)^2 + (y-y_3)^2} \right] \times \left\{ (1-\nu) - 2(1+\nu) \frac{(x-x_3)^2}{(x-x_3)^2 + (y-y_3)^2} \right\} + \frac{(y-y_3)}{(x-x_3)^2 + (y-y_4)^2} \times \left\{ (1-\nu) - 2(1+\nu) \frac{(x-x_4)^2}{(x-x_3)^2 + (y-y_4)^2} \right\} - \frac{(y-y_4)}{(x-x_4)^2 + (y-y_3)^2} \times \left\{ (1-\nu) - 2(1+\nu) \frac{(x-x_3)^2}{(x-x_4)^2 + (y-y_3)^2} \right\} - \frac{(y-y_4)}{(x-x_4)^2 + (y-y_4)^2} \times \left\{ (1-\nu) - 2(1+\nu) \frac{(x-x_4)^2}{(x-x_4)^2 + (y-y_4)^2} \right\} \right] d\eta$$
(A.5)

$$\tau_{xy}^{(3)}(x,y) = \frac{1}{4\pi} \int_{0}^{l_f/2} \sigma^*(\eta) \left[ \frac{(x-x_3)}{(x-x_3)^2 + (y-y_3)^2} \right] \times \left\{ (1-\nu) + 2(1+\nu) \frac{(y-y_3)^2}{(x-x_3)^2 + (y-y_3)^2} \right\} + \frac{(x-x_4)}{(x-x_3)^2 + (y-y_4)^2} \times \left\{ (1-\nu) + 2(1+\nu) \frac{(y-y_3)^2}{(x-x_3)^2 + (y-y_4)^2} \right\} - \frac{(x-x_3)}{(x-x_4)^2 + (y-y_3)^2} \times \left\{ (1-\nu) + 2(1+\nu) \frac{(y-y_4)^2}{(x-x_4)^2 + (y-y_3)^2} \right\} - \frac{(x-x_4)}{(x-x_4)^2 + (y-y_4)^2} \times \left\{ (1-\nu) + 2(1+\nu) \frac{(y-y_4)^2}{(x-x_4)^2 + (y-y_4)^2} \right\} d\eta$$
(A.6)

where  $x_3$ ,  $y_3$  and  $y_4$  are given by

$$x_3 = x_0 + \eta$$
  
 $x_4 = x_0 - \eta$   
 $y_3 = y_0 + d_f/2$   
 $y_4 = y_0 - d_f/2$ 

### **Appendix**

 $\mathbf{B}$ 

# **Average Strain and Stress Theorems**

In this appendix the average stress and strain theorems are outlined since these are used in conjunction with the Mori - Tanaka creep modelling. These theorems can also be found in [1].

Under conditions of imposed macroscopically homogeneous stress or deformation fields on the considered representative volume element (RVE), the average stress and strain are defined as

$$\langle \sigma_{ij} \rangle = \frac{1}{V} \int_{V} \sigma_{ij} dV$$

$$\langle \varepsilon_{ij} \rangle = \frac{1}{V} \int_{V} \varepsilon_{ij} dV$$
(B.1)

where V is the volume of the RVE, and  $\langle \rangle$  denotes averaging.

Homogeneous boundary conditions applied on the surface of the homogeneous body result in a homogeneous field in the body. Such boundary conditions are obtained by applying displacements on the boundary S as

$$u_i(S) = \varepsilon_{ij}^0 x_j \tag{B.2}$$

where  $\varepsilon_{ij}^0$  are constant strains. Alternatively tractions can be applied on S such that

$$t_i = \sigma_{ij}^0 n_j \tag{B.3}$$

where  $\sigma_{ij}^0$  are constant stresses and  $n_j$  is the unit outward normal vector to S.

### B.1 Average strain theorem

The average strain theorem states that the averaged strain within the RVE is equal to the constant strain applied on the surface.

To calculate the average strain in a two - phase composite the strain displacement relations are used

$$\varepsilon_{ij} = \frac{1}{2} \left( u_{i,j} + u_{j,i} \right) \tag{B.4}$$

Inserting this into the last of equations (B.1) yields

$$2V\langle \varepsilon_{ij} \rangle = \int_{V_1} \left( u_{i,j}^{(1)} + u_{j,i}^{(1)} \right) dV_1 + \int_{V_2} \left( u_{i,j}^{(2)} + u_{j,i}^{(2)} \right) dV_2$$
 (B.5)

where superscripts  $^{(i)}$  denote phases i of the composite with  $V_i$  being the volume occupied by phase i. Using the Gauss theorem

$$\int_{V} u_{k,l} dV = \int_{S} u_{k} n_{l} dS \tag{B.6}$$

implies that

$$2V\langle \varepsilon_{ij} \rangle = \int_{S_1} \left( u_i^{(1)} n_j + u_j^{(1)} n_i \right) dS + \int_{S_2} \left( u_i^{(2)} n_j + u_j^{(2)} n_i \right) dS$$
 (B.7)

where  $S_i$  are the bounding surfaces of phase i. The surfaces  $S_1$  and  $S_2$  contain the interfaces  $S_{12}$  and the external surface S. Assuming perfect bonding between the phases, i.e.  $u_i^{(1)} = u_i^{(2)}$  at the interface it readily follows that the contributions from  $S_{12}$  cancel each other in the integrals of the equation above. This leads to

$$\langle \varepsilon_{ij} \rangle = \frac{1}{2V} \int_{S} (u_i n_j + u_j n_i) dS$$
 (B.8)

Substituting the boundary condition (B.2) into the equation above and using the Gauss theorem yields

$$\langle \varepsilon_{ij} \rangle = \frac{1}{2V} \int_{S} \left( \varepsilon_{ik}^{0} x_{k} n_{j} + \varepsilon_{jk}^{0} x_{k} n_{i} \right) dS$$

$$= \frac{1}{2V} \varepsilon_{pj}^{0} \int_{V} 2x_{p,i} dV$$
(B.9)

remembering that  $\delta_{ij} \equiv x_{i,j}$  yields the final result, namely that

$$\langle \varepsilon_{ij} \rangle = \varepsilon_{ij}^0$$
 (B.10)

### B.2 Average stress theorem

The average stress theorem states that the homogeneous boundary tractions applied on S produce a stress field within the RVE whose average,  $\langle \sigma_{ij} \rangle$ , is identical to the constant stress  $\sigma_{ij}^0$ . To prove that, the equilibrium equations in the absence of body forces are considered

$$\sigma_{ii,j} = 0 \tag{B.11}$$

which implies that

$$(\sigma_{ik}x_j)_{,k} = \sigma_{ik,k}x_j + \sigma_{ik}x_{j,k} = \sigma_{ik}\delta_{jk} = \sigma_{ij}$$
(B.12)

Substituting this relation into the first of equations (B.1) gives

$$V\langle \sigma_{ij}\rangle = \int_{V} (\sigma_{ik} x_j)_{,k} dV \tag{B.13}$$

and by Gauss' theorem

$$V\langle\sigma_{ij}\rangle = \int_{S_1} \sigma_{ik}^{(1)} x_j n_k^{(1)} dS + \int_{S_2} \sigma_{ik}^{(2)} x_j n_k^{(2)} dS$$
 (B.14)

Since tractions are continuous at the interfaces  $S_{12}$ , i.e.  $\sigma_{ij}^{(1)} n_j^{(1)} = \sigma_{ij}^{(2)} n_j^{(2)}$  the contributions from  $S_{12}$  in the two integrals cancel each other and the former equation reduces to

$$V\langle \sigma_{ij} \rangle = \int_{S} \sigma_{ik} x_{j} n_{k} dS = \sigma_{ik}^{(0)} \int_{S} x_{j} n_{k} dS$$
$$= \sigma_{ik}^{(0)} \int_{V} x_{j,k} dV = V \sigma_{ij}^{(0)}$$
(B.15)

and thus

$$\langle \sigma_{ij} \rangle = \sigma_{ij}^{(0)} \tag{B.16}$$

which is the desired relation.

# Copyright © 2000 Jan Schjødt-Thomsen Reproduction of material contained in this report is permitted provided that the source is given. Additional copies are available at the cost of printing and mailing from Line Nesgaard Jensen, Institute of Mechanical Engineering, Aalborg University, Pontoppidanstraede 101, DK-9220 Aalborg East, Denmark. Telephone: +45 96 35 93 00, Fax: +45 98 15 14 11. Questions and comments are most welcome and can be directed to the author at the same address or by electronic mail: jst@ime.auc.dk. Printed at Aalborg University, January 2000. ISSN 0905-2305